On the use of aerosol optical properties and satellite-retrieved trace gases in regional air quality modelling

EMMA ANDERSSON

Department of Earth and Space Sciences
CHALMERS UNIVERSITY OF TECHNOLOGY
Gothenburg, Sweden 2015

On the use of aerosol optical properties and satellite-retrieved trace gases in regional air quality modelling
EMMA ANDERSSON

Cover: Aerosol optical depth at 532 nm, simulated by MATCH using aerosol dynamics and a more realistic treatment of particle morphologies and mixing states compared to externally mixed homogeneous spheres. Hourly data from 2007-12-22 at 12:00 over the European domain.

On the use of aerosol optical properties and satellite-retrieved trace gases in regional air quality modelling

EMMA ANDERSSON
Department of Earth and Space Sciences
Chalmers University of Technology

Abstract

The effects of anthropogenic pollutants in the lower atmosphere (troposphere) have been shown, historically and scientifically, to have a deleterious effect on both plant and animal life. Pollutants such as near-surface ozone and soot (black carbon) are two notorious examples with clear anthropogenic sources. Consequently, laws controlling emissions and future projections of air quality, especially around large cities worldwide, are critical to the vibrancy and sustainability of life.

The main purpose of this thesis is to summarise two studies involving the regional chemical transport model MATCH and its simulations of carbon monoxide (CO), ozone (O_3) and aerosols. The core question addressed in the first study is how the long-range transport representation of carbon monoxide and ozone can be evaluated. Simulating the long-range transport in regional models is important to get a well represented vertical distribution of the long lived (relative to modelling time and domain) species, a category to which the aforementioned gases belong. A methodology for evaluating lateral boundary conditions (LBCs) is tested for LBCs derived from the global EMEP MSC-W model. First, the method directly evaluates the LBCs at the model boundaries with satellite retrievals from MOPITT (CO) and OMI (O_3). The second part of the method uses the new LBC to drive MATCH model. MATCH is compared to satellite-retrieved data from the AIRS sensor and ground based observations from the GAW-network. The method of evaluating LBCs highlights the need for better evaluation techniques, rather than only using a direct evaluation at the lateral boundaries. The use of combined ground-based and satellite measurements, especially close to the model boundaries, needs to be further exploited.

A similar study, where aerosols concentrations fields are confronted with satellite retrievals, instead of trace gases, cannot be made without the use of an aerosol optics model. An optics model simulates the corresponding radiometric properties as retrieved from satellite measurements. Therefore, the focus of the second study involves the simulation of aerosol optical properties using a new, stand-alone, aerosol optics model. Simulated aerosol fields are provided by using MATCH. The new optics model simulates radiometric properties from particles whose morphology is based on more realistic assumptions. Special consideration is given to fractal aggregates of externally mixed soot and inhomogeneous internally mixed soot. The latter part mixes solid soot with liquid hydrophilic substances, where parts of the soot particle are confined as a solid spherical core and parts of the soot is mixed into a liquid phase coating of for example sulphate or nitrate. The simulations of the new optics model resulted in large impacts on the radiometric properties, comparable to the effects of using aerosol dynamics. This is an important finding since most climate and remote sensing applications, today, use rather coarse and simple models to retrieve aerosol optical properties.

Keywords: Air Quality, Model, Satellite, Radiation, Climate

Appended Papers

The thesis is based on the following papers:

- E. Andersson, M. Kahnert, A. Devasthale: Evaluation of lateral boundary conditions in a regional chemical transport model, *Geosci. Model Dev. Discuss.*, 8, 5763-5808, doi:10.5194/gmdd-8-5763-2015, 2015

- E. Andersson and M. Kahnert: Coupling aerosol optics to a chemical transport and aerosol dynamics model, manuscript prepared for *Geosci. Model Dev.*, 2015.

Contents

Acknowledgements

I would like to express special thanks to my supervisor Michael Kahnert, who has given me support and encouragements throughout this first half of my doctoral study. Without you I do not think I would have come this far. Many thanks also to my co-supervisors, David Simpson at Chalmers and Abhay Devasthale at the Swedish Meteorological and Hydrological Institute (SMHI), for valuable discussions, feedback and support.

This work has been done in collaboration with SMHI and I would like to thank everyone from the Air quality research group for helping me understand the MATCH model and to use the systems on NCS. I also want to thank my colleagues at GEMM for help and support.

Last, but not least, I want to thank my family and beloved partner for being by my side supporting and helping me through both good and bad. Thank you Marston, for teaching me that writing is an art, it takes humility, patience and practice to master.

1

Introduction

Air quality, or air pollution, has been a concern for humankind for the longest of time. Records from ancient Rome describes how "the oppressive atmosphere" affects the physical conditions of the city inhabitants (Mosley 2014). This oppressive atmosphere was caused by emissions from potteries, homes, and workshops. Historically, air pollution has been seen as something mostly occurring the troposphere and affecting e.g., animal respiratory systems and destroying stomata in plants and disabling their ability to photosynthesise. While the aforementioned anthropogenic effects on air quality were isolated across the globe, during the last decades, it has become evident that air pollution is global problem and affects the radiative balance of the planet and thereby the climate.

Given the ongoing and historical evidence of anthropogenic induced climate change, it remains critical to monitor and model air quality, both regionally and globally. Today there are many different observation platforms and chemical transport models (CTM) in operation to provide scientists and decision makers with information about air quality. Observations and simulations of air quality further our scientific knowledge and provide a basis when creating laws and restrictions on, e.g., emissions and land use.

Space borne measurements of air quality, because for their good spatial coverage, are widely used, but they do not measure the concentration of atmospheric constituent directly. Instead they measure radiometric signals which must be converted to an atmospheric state via a process called *retrieval*. The retrieval process can result in large uncertainties, especially when retrieving information from the lower part of the atmosphere, the troposphere. Therefore ground-based measurements are widely employed since they generate less uncertainties and provide higher temporal resolution data at the cost of worse spatial coverage. An additional attribute is that there exist large networks of ground-based air quality observations sites all over the globe.

Simulating air quality summarise and expand the theoretical knowledge we have acquired so far. This includes the dynamical and chemical processes in the atmosphere. There are many different types of models, simulating local, regional or global scale processes. Some of these focus on dispersion, climate and/or radiative properties. By comparing model results with measurements we can confirm, or dismiss, the current knowledge we have about the atmospheric, radiative, and chemical processes.

This thesis focuses on a regional CTM simulation of the dispersion of chemicals in the troposphere. To put the work done in this thesis into perspective, a description of the troposphere and its important processes is given in chapter 2. The used regional CTM is also confronted with satellite retrieved and ground based measurements, therefore it is important to understand the underlying concepts of atmospheric radiative transfer and how observations of the atmosphere can be carried out. These topics are covered in Chapters 3 and 4. Chapter 5 describes a chemical transport model, and Chapter 6 summaries the papers this thesis is built upon together with an outlook of continued research.

2

The Troposphere

2.1 Structure of the Atmosphere

The atmosphere can be divided into different parts, depending on whether one basis this on the dynamics, photo-chemistry or thermodynamics, but the most common division is based on the vertical temperature profile, with its four inflection points as divisions. The first layer (from the ground) is called the troposphere. In this region the Earth is absorbing the incoming radiation from the sun and emits infrared radiation back up. This results in an almost linear decrease of the temperature, with a lapse rate of 5-7 K km^{-1} up to the tropopause, the first inflection point at around 10-16 km, depending on the latitude. After the tropopause, the stratosphere continues with an increase in temperature due to a layer with higher concentration of ozone. Here, the ozone absorbs large parts of the ultraviolet radiation, which is dangerous to almost all living things on Earth, and heats up its surrounding. The temperature increase stops at the stratopause, at around 50 km, where the heating from ozone diminishes and the mesosphere begins. In this region at high latitudes during summer, the famous Noctilucent clouds are found, night glowing clouds consisting of ice crystals in the higher part of the mesosphere. The last inflection point is called the mesopause, where the temperature rises once again into the thermosphere. This region of the atmosphere is very different from the previous parts, in that it is not electrically neutral, since the solar radiation ionises the molecules and creates a plasma of ions and free electrons, which can effect the dynamics.

This thesis focuses on the troposphere where approximately 75-80% of the mass of the atmosphere is situated, 99% of atmospheric water resides, and where there are high levels of aerosols and trace gases due to emissions from the Earth's surface. The name troposphere can be translated into "turning" or "changing" sphere, and comes from its characteristic strong convective processes creating clouds and precipitation and thereby different kinds of weather phenomena.

2.2 Tropospheric chemistry

Chemistry in the troposphere involves many complex interactions. This section will give a short overview of the constituents of the troposphere and what drives

chemistry in the troposphere. The chemistry is described in terms of the three different aggregations states, gas, liquid, and solid. Gas-phase chemistry deals with the reactions of all the trace and bulk gases, whereas the liquid and solid phase chemistry deals with all the particulate matter, or particles, in the atmosphere, such as sulphate aerosol and soot. This section is largely based upon Finlayson-Pitts and Pitts Jr. (2000) and Monks (2005).

The bulk composition of the atmosphere is 78% nitrogen (N_2), 21% oxygen (O_2), 1% argon (Ar) and about 0.039% carbon dioxide (CO_2). The rest of the composition consists of various trace gases which have much shorter life times, but interact and drive the whole system of complex chemical reactions. Most of these trace gases are emitted from the surface, undergo chemical and physical transformations, get transported and in the end deposited or transformed into chemical species. These four events are the core pillars of the tropospheric chemistry system and are illustrated in a simplified scheme in Fig. 2.1.
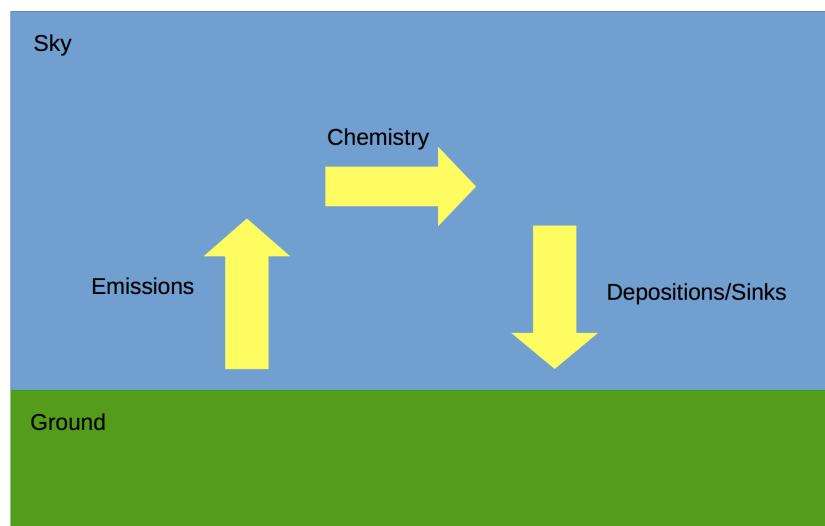

Figure 2.1: Simplified scheme of the tropospheric chemistry where the four elements of the tropospheric chemistry system emission, chemistry, deposition/sinks and transport (represented by the yellow arrows) are illustrated.

When studying the quality and impact of the air surrounding us, the emission, transport, chemistry and sinks need to be considered for gas- liquid- and solid phase constituents.

A large part of the chemistry in the atmosphere is taking place in the state of gases. The gas-phase chemistry of the troposphere can be described in analogy with a low temperature combustion engine where an overall reaction can be described as; emitted hydrocarbons (C_xH_y) being oxidised by O_2 creating CO_2 and hydrogen gas (H_2O) (Monks 2005). But unlike in a combustion engine, which is thermally initiated, the tropospheric chemistry is initiated and maintained through photochemistry. Photochemistry is the process by which some atmospheric species interact with radiation at certain energy levels, to change the molecules or atoms and create highly reactive species or radicals. These rad-

icals are the main drivers of the chemistry in the troposphere; and they serve as oxidisers of the lower part of the atmosphere. These oxidants have a low abundance in the atmosphere due to their fast reaction times and thereby short life-times. Their life spans range from seconds to weeks, but yet are responsible for chemically cleaning and stabilising large parts of the atmosphere. The most important oxidants in the atmosphere are the hydroxyl radical (OH), the nitrate radical (NO_3), and tropospheric O_3.

Particles consist of liquid and solid materials. They are not only affected by chemical transformations, but also aerosol dynamical processes, such as condensation, coagulation, and nucleation. Particles are larger than gas molecules, but most of them are still too small for the human eye to detect; and the size ranges from 0.001 to 100 μm. The smallest particles consist of nucleated droplets containing ammonium sulphate or organic substances, then ranging from fine dust and soot to the larger particles like pollen and coarse dust. The larger particles are usually detected close to the source from where they were emitted, and the smaller particles can be transported over much longer distances, depending on their composition and in what microphysical processes they are involved.

2.3 Dynamics in the troposphere

Air quality and climate are largely dependent upon the dynamics of the atmosphere. Air quality is dependent upon the vertical mixing of air and on long range transport of air pollutants. Whereas changes in the climate cause changes in the circulatory system with more frequent strong hurricanes and more powerful El Niño [1] events (Cai et al. 2014).

There are many physical processes such as thermodynamical, radiative and frictional processes that affect both the large and small scale motions of the atmosphere. Phenomena such as the general circulation, gravity waves and extratropical hurricanes are examples of large scale dynamical features, where the size of the patterns are on the order of 1000 km in horizontal length. Smaller scales features such as squall lines and deep convection belong to the class of mesoscale systems, which are on the order of around 5 km. The even smaller dynamical features, below 1 km in size, are called micro-scale features, where turbulence with individual eddies and thermals are described. In the lower part of the atmosphere, all scales of dynamics influence the transport and mixing of the air. From the bottom of the troposphere, where the air interacts with the surface of the Earth and creates mechanical turbulence and where warm parcels of air rises and create convection, to the free troposphere, where the air is more stratified and influenced by larger scale motions such as deep convection and the Coriolis force.

All dynamical features of the atmosphere can theoretically be described by a set of primitive equations, related to fluid motion, called the NavIer-Stokes equations. These equations describe the change of momentum, mass and energy within a predefined system (a fluid parcel), derived from Newton's second law of motion together with the conservation of momentum, mass and energy. When modelling the atmosphere and its transport and mixing and using the

---

[1]An El Niño event is characterised by warm sea surface temperatures in the eastern pacific ocean causing ocean and atmospheric circulatory patterns to change, affecting the weather systems all over the globe.
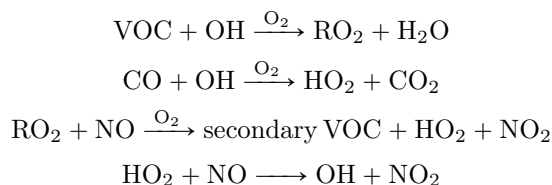
primitive equations, it is important to consider the resolution of the model. Depending on the size of the model grid box, different dynamical systems can be described theoretically. If the resolution is smaller than desired dynamical features, these features can be described with NavIer-Stokes equation. Otherwise, if the dynamical features are smaller than the grid box, the dynamics needs to be parameterised. This can contribute to uncertainties. A more developed discussion regarding the mathematical description of the atmospheric dynamics and how it is implemented in modelling the chemical transport, is discussed in section 5.1.2.
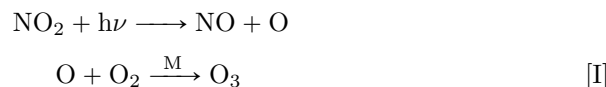
2.4   Air quality and Climate

Air quality and climate are tightly coupled together. In the latest IPCC report (Myhre et al. 2013), it was stated that improvements in air quality will *have* effects on the climate, through many important gaseous species and particles. However, the effects of the improvements depend on chemical and physical characteristics of the pollutants. CO_2 is the gas mostly associated with climate change, due to its interaction with long-wave radiation and its long life time in the atmosphere of about 100-1000 years. CO_2 is therefore a well mixed trace gas and can affect the radiative balance of the Earth on a time scale of decades. Other chemical species can have even stronger impacts when interacting with radiation, such as CH_4 and tropospheric ozone, but they do not have nearly as long life times as CO_2 (CH_4 has a lifetime of about 9.8 ± 1.6 years and tropospheric O_3 has a lifetime of about 22 days (Myhre et al. 2013)) and are therefore not as well mixed. These shorter lived species are often referred to as Short-Lived Climate Pollutants (SLCPs). Beside methane and ozone, hydrofluorocarbons (HFCs) and black carbon are some of the considered SLCPs which also are thought to harm public health, reduce food security, increase melting of ice and snow, and disrupt weather patterns. Efforts are made to reduce and mitigate these effect, for example in 2012, a coalition was created with the aim of reducing and mitigating the effects of these SLCPs, the Climate and Clean Air Coalition, in which several countries and organisations have signed up to take action (`http://www.ccacoalition.org`).

2.4.1   Tropospheric O_3

Most of the SLCPs, except tropospheric ozone, are dependent upon direct emission sources. Ozone is therefore considered a secondary air pollutant. The main sources of ozone in the troposphere are photochemical reactions and transport from the stratosphere, which holds 85-90% of the atmospheric ozone. The chemical reaction scheme in [I] shows the photochemical production of ozone in the troposphere, where R is short for many of the different organic compounds or hydrocarbons.

$$VOC + OH \xrightarrow{O_2} RO_2 + H_2O$$
$$CO + OH \xrightarrow{O_2} HO_2 + CO_2$$
$$RO_2 + NO \xrightarrow{O_2} secondary\ VOC + HO_2 + NO_2$$
$$HO_2 + NO \longrightarrow OH + NO_2$$

$$\text{NO}_2 + \text{h}\nu \longrightarrow \text{NO} + \text{O}$$

$$\text{O} + \text{O}_2 \xrightarrow{\text{M}} \text{O}_3 \qquad\qquad [\text{I}]$$

The photochemical production of O_3 is the largest source of tropospheric O_3 and is solely dependent upon precursor emissions of volatile organic compounds (including methane) VOCs, carbon monoxide CO, and nitrogen oxides NO_x, and the incoming solar radiation with wavelengths $\lambda < 420\,\text{nm}$. The sources of ozone are balanced with different sinks, where the largest sink of tropospheric ozone is the catalytic reaction cycle involving different radicals, such as OH, NO, chlorine Cl or Bromine Br, see reaction scheme [II],

$$\text{X} + \text{O}_3 \longrightarrow \text{XO} + \text{O}_2$$

$$\text{XO} + \text{O} \longrightarrow \text{X} + \text{O}_2 \qquad\qquad [\text{II}]$$
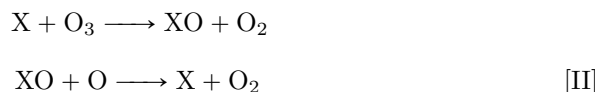
where X symbolises the radical catalyst. The most effective radical destructor of ozone is the OH radical.

When studying the trends and impacts of tropospheric ozone it is important to study its precursor concentrations and trends. Many of the ozone precursors are emitted from anthropogenic sources, such as fossil fuel and biomass burning. The trend of tropospheric ozone therefore varies regionally. For example, in Europe and North America there are declining trends, whereas in East Asia, ozone has increased (Granier et al. 2011).

2.4.2 Black carbon

Black carbon is a primary particle and emitted directly into the atmosphere. The largest emission sources of black carbon (BC), or soot, are forest fires and anthropogenic fossil fuel and biomass burning. Freshly emitted BC particles are classified as fine particles with a corresponding aerodynamic diameter[2] of $< 2.5\,\mu\text{m}$. As freshly emitted BC particles age, they undergo changes due to condensation, coagulation and photochemical reactions. This results in particle growth, changes in the particle morphology, mixing state and hygroscopicity. All these microphysical processes determine the health effects and radiative impact of BC particles. The typical lifetime of a BC particle in the atmosphere is around 1 day to 1 week (Myhre et al. 2013).

BC particles are harmful to public health since they contribute to respiratory and cardiovascular diseases, through inhalation. Black carbon also affects the climate, due to its ability to absorb radiation and decreases the surface albedo when deposited on snow covered surfaces.

---

[2]The aerodynamic diameter corresponds to the diameter of a spherical particle with the density of $1\,\text{g/cm}^3$ and the same settling velocity in air as the considered particle

3

Atmospheric Radiative Transfer

Radiation propagating through a medium will interact with it and be altered through different radiative processes, such as absorption, emission, single scattering and multiple scattering. In the atmosphere, the interaction between its gaseous constituents and particles with radiation is crucial for understanding the climate and remote sensing measurements. In climate modelling, the energy budget (change in incident solar and outgoing terrestrial radiation) drives the whole climate system. A change in the atmospheric composition will cause a change in the radiative properties of the atmosphere which alters the radiative balance and forces a change upon the climate system, a climate forcing. In remote sensing measurements of the atmosphere, radiation signatures are detected. To use this signature and learn about the composition of the atmosphere it is necessary to understand how the radiation has interacted with the atmospheric component.

Radiative transfer aims to describe the interaction between radiation and matter. Atmospheric radiative transfer modelling is used either in a direct manner, where the atmospheric composition is known and the radiometric observables are desired, or the opposite where the inverse of the direct model need to be used. To solve the direct problem one can couple a model predicting the concentrations of the atmospheric constituents, an optical model deriving the radiative properties and finally a radiative transfer model which derives for example the difference in the energy budget. To solve the inverse problem one usually needs not only a direct model, but also an a priori of the atmospheric state.

This chapter will give a short overview of the key concepts of radiative transfer, beginning with black-body radiation, and how this concept can be expanded to non black bodies, and continuing with the radiative transfer equation and concepts of radiative balance. The content of this chapter is largely based upon Wallace and Hobbs (2006) and Liou (2002).

3.1 General radiative concepts

Electromagnetic (EM) radiation consists of propagating oscillations of electric and magnetic fields, travelling at the speed of light (c= $2.998 \cdot 10^8$ m/s through vacuum). The EM radiation can be described in a classical way where it can be seen as an ensemble of oscillating waves characterised by having a certain wavelength λ [m] or frequency [1/s] $\nu = c/\lambda$. EM radiation with different wavelengths construct an electromagnetic spectrum. Figure 3.1 shows the electromagnetic spectrum. In contrast to the classical description of EM radiation, the quantum description says that EM radiation consists of elementary particles, photons, with discrete sets of energies. Each photon has an energy of $E = \frac{h \cdot c}{\lambda} = h \cdot \nu$., where $h = 6.626 \cdot 10^{-34}$ [J·s] and called the Plank's constant.

All bodies of matter emit radiation, with energies depending on the temperature of the body. If the body has a uniform temperature and composition as well as being in thermal equilibrium with its surrounding (i.e. it absorbs the same radiation as it emits), the body is defined as a black-body and absorb all incident wavelengths. The emission spectrum of a black-body is given by Plank's law,

$$B_\lambda(\lambda,T) = \frac{2hc^2}{\lambda^5} \frac{1}{e^{\frac{hc}{\lambda k_B T}} - 1} \tag{3.1}$$

where $B_\lambda(\lambda,T)$ is the spectral intensity (radiant energy per unit time and per solid angle, wavelength and area)[W/(sr· m^2· m)], T [K] is the temperature and $k_B = 1.38 \cdot 10^{-23}$ [J/K] is Boltzmann's constant. This black-body spectrum is an idealised case. Most bodies, such as a gaseous medium, can also reflect and transmit incoming radiation. However, the theory of black-body radiation can be extended and used for non-black bodies with a monochromatic emissivity, ϵ_λ, which is defined as the ratio of the radiation emitted by the body and the idealised radiation a black-body with the same temperature would emit. The non-black body spectrum follows as,

$$I_\lambda(\lambda,T) = \epsilon_\lambda \cdot B_\lambda(\lambda,T) \tag{3.2}$$

where $I_\lambda(\lambda,T)$ is the spectral intensity of the non-black body. As stated above, if a body or a medium is in thermal equilibrium with its surrounding, the emission ϵ_λ and absorption α_λ are equal; this is referred to as Kirchhoff's law. For the lower part of the atmosphere this law is applicable, since the frequency of molecular collisions is larger than the frequency of molecular absorption and emission of radiation near the wavelength of interest. This phenomena is called local thermal equilibrium (LTE).

In figure 3.2, the black-body spectra of the sun with an approximate black-body temperature of 6000 K and the Earth 255 K, respectively, are shown together with the absorption at the temperate troposphere and at ground level. The largest part of the solar spectrum is contained between the wavelengths 100 nm and $4\,\mu$m, where 90 % of the radiation comes from the visible ($0.4\,\mu$m -$0.75\,\mu$m) and the infrared ($0.75\,\mu$m-$5\,\mu$m). The terrestrial radiative spectrum is contained between the wavelengths $4\,\mu$m-$200\,\mu$m and is entirely thermal infrared. The absorption in figure 3.2 is shown together with the different gaseous species in the atmosphere affecting the radiation with absorption. More of the physics behind the absorption and scattering is described in section 3.2.
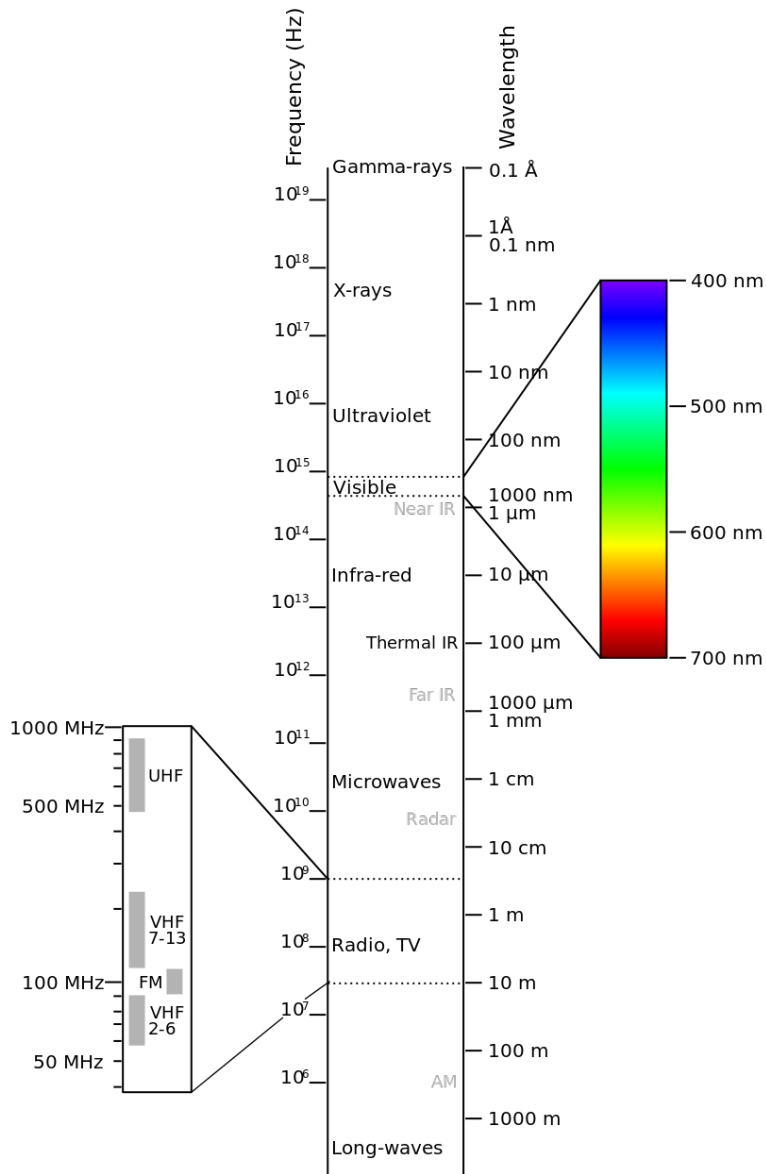
Figure 3.1: The electromagnetic spectrum, illustrating the different parts of the spectrum together with their wavelengths and frequencies (Blacus 2012).
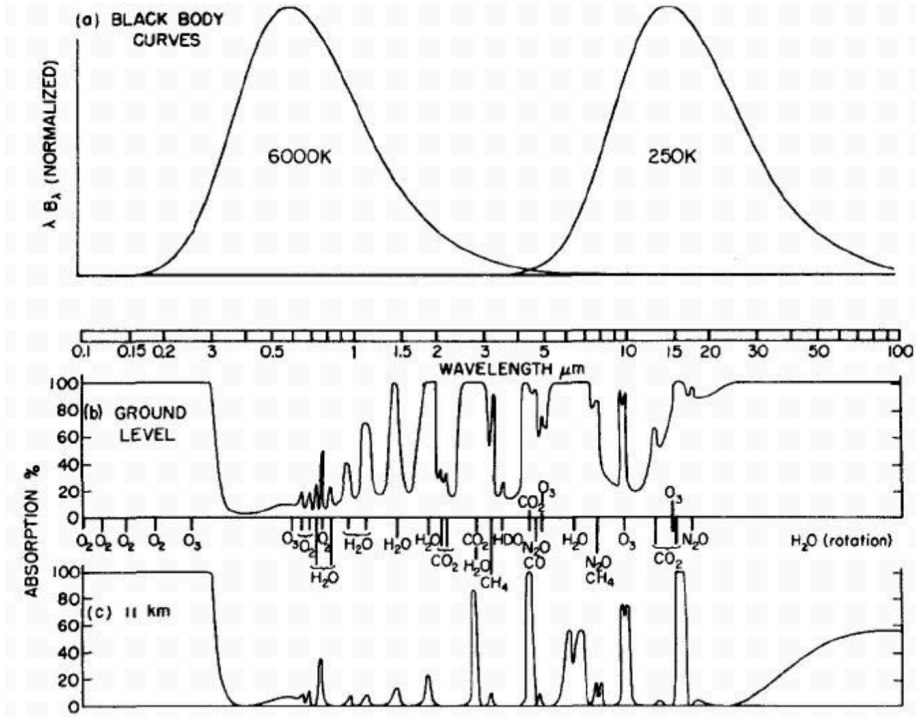
Figure 3.2: (a) Normalised black-body spectra from the sun (6000K) and the Earth (255K) as a function of wavelength. b) and c) show the monochromatic absorption at 11km and ground level, respectively (Gooby and Yung 2005). Permission to use given by the Oxford University Press Inc.

3.2 Scattering, Absorption and Emission

The aforementioned difference in average temperature on Earth due to the presence of the atmosphere is because of its different transmission properties of terrestrial and solar radiation. The atmosphere is fairly transparent to a larger part of the solar spectrum of radiation, whereas it is relatively opaque to the terrestrial thermal radiation. This effect is what is commonly referred to as the "Greenhouse effect". The transmission properties of the atmosphere depend upon the scattering and absorption of the different gases and particles suspended in the air. Scattering and absorption attenuates the radiation it interacts with. Looking at a single molecule/particle or a small volume containing an ensemble of particles, the associated rate of energy removal related to the incident energy flux, is defined as an extinction cross section σ_e [m^2]. The extinction cross section is a sum of scattering and absorption cross sections. The change in spectral intensity due to the interaction with matter, like the atmosphere, is linearly dependent upon the i) intensity of the incident radiation, ii) the local concentration of the gases or particles and iii) the extinction cross section, according to equation 3.3,

$$d\,\mathrm{I}_\lambda = -\,\mathrm{I}_\lambda\,\sigma_{e,\lambda} N dz \qquad (3.3)$$

14

where I_λ is the monochromatic spectral intensity [W/(sr$\cdot$ m$^2\cdot$ m)], N is the number density of the gas or particle considered, and dz is the differential path length through which the radiation has travelled. When dealing with attenuation of radiation in radiative transfer, it is convenient to introduce the concept of optical depth, τ,

$$\tau_\lambda = \int_{z_0}^{\infty} \sigma_{e,\lambda}(z) N dz \tag{3.4}$$

$$\implies \quad I_\lambda = I_{\lambda,0} \cdot e^{-\tau_\lambda} \tag{3.5}$$

The optical depth is a commonly used radiative parameter to describe the total attenuation of an electromagnetic wave travelling through a slant column of air. Solving equation 3.3 and using the concept of optical depth, results in 3.5. The continuing sections will separately describe monochromatic absorption and scattering for different relationships between the wavelengths and the size of the interacting atom/molecule or particle. After that, the section will continue with the mathematical formulation of the radiative transfer equation including all of the aforementioned radiative processes.

3.2.1 Absorption

The atmospheric absorption caused by molecules and particles depends upon their molecular structure. The energy that an atomic or molecular oscillator can absorb is discrete and and can be represented by transitions of electronic, rotation or vibration energy levels. Atoms can only change electronic levels (with their fine- and hyperfine structure) or photo-dissociate, whereas molecules have several rotational and vibrational energy levels. Depending on the structure of the molecule, it has more or less rotational and vibrational degrees of freedom. Diatomic molecules such as CO, have two degrees of rotational freedom and one vibrational mode, whereas a non-linear triatomic molecule such as O_3 as three rotational degrees of freedom and three vibrational modes, giving rise to the many potential energy levels into which the molecules can absorb radiation.

Particles differ from atoms and molecules, in that they are in a solid or liquid state. The constituting elements are seen as a lattice where the energy levels overlap each other and create a continuous energy band. The absorption can be treated with classical EM theory, Maxwell's theory, and bulk dielectric properties like the refractive index $m = m_r + im_i$, which describes the propagation of radiation through a medium. For a non-absorbing medium, the imaginary part of the refractive index $m_i = 0$. Section 3.2.2 discusses scattering by spherical particles and how Lorenz-Mie theory can be applied to describe both the scattering and absorption.

Due to the discrete nature of the energy absorbed and emitted by molecules and atoms, a spectra from such an emission, would create a line at a certain frequency. These absorption lines have a finite width due to i) pressure broadening, where collisions between the absorbing/emitting molecules induce transitions between energy levels, thus limiting the lifetime of excited states, ii) broadening due to the Doppler effect and iii) natural line broadening, caused by the finite life time of the excited states due to spontaneous emissions. The natural line broadening is comparatively very small and almost negligible, whereas the Doppler broadening is the dominant line broadening in the upper atmosphere,

and pressure broadening prevails in the lower part of the atmosphere. Figure 3.3 illustrates the relative broadening caused by Doppler and pressure broadening.
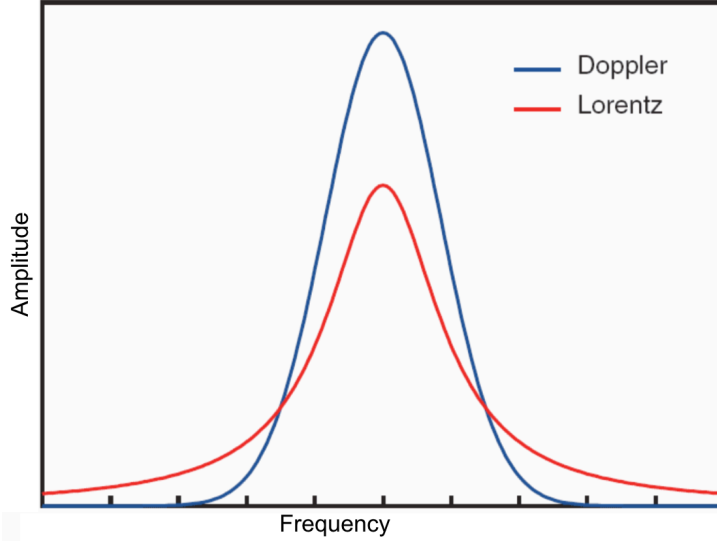

Figure 3.3: The line shape of the broadening from collisions which follows a Lorentzian distribution and from Doppler broadening with a Gaussian.

3.2.2 Scattering

Scattering is the physical process in which a electromagnetic wave interacts with a particle (in this case a molecule or an aerosol) and continuously removes energy from the incident wave and reradiates it out in all directions. The scattered intensity can be expressed according to equation 3.6,

$$I_{s,\lambda}(\Theta) = I_{\lambda,0} \frac{\sigma_{s,\lambda}}{r^2} \frac{P(\Theta)}{4\pi} \qquad (3.6)$$

where $\sigma_{s,\lambda}$ is the scattering cross section, r is the distance from the independent scatterer to the observation point, $P(\Theta)$ is the phase function, which describes the angular distribution of the scattered intensity and Θ is the angle between the incident and scattered wave.

Depending on the size of the particle, the scattering process differs. Introducing the size parameter $x = 2\pi r/\lambda$, a dimensionless parameter relating the size of the particle to the wavelength, where r is defined as a radius for a spherical particle. Even though most particles are not spheres, rather they come with a variety of shapes, it is a frequently used approximation for the development of different scattering theories. If the size parameter $x << 1$, i.e. the size of the particle is much smaller than the wavelength, Rayleigh scattering can be applied. This type of scattering has the greatest dependence on the wavelength where the scattering cross section $\sigma_{s,\lambda} \propto \lambda^{-4}$,

$$\sigma_{s,\lambda} = \frac{2\pi^5 \cdot r^6}{3\lambda^4} \left(\frac{m^2 - 1}{m^2 + 2} \right)^2 \qquad (3.7)$$

where $\sigma_{s,\lambda}$ is the scattering cross section that relates the scattered and incident spectral intensity. For the solar radiation, the imaginary parts of the refractive index for air molecules is so small, the absorption may be neglected. A good example of Rayleigh scattering is the blue sky caused by scattering of visible light by air molecules, where the scattered intensity of the incoming solar radiation $I_\lambda \propto \lambda^{-4}$. Since a large portion of the incoming solar radiation is visible light, the smaller blue wavelengths ($\lambda \approx 0.425\mu$m) scatters about 5.5 times more efficiently than red wavelengths ($\lambda \approx 0.650\mu$m).

For size parameters $x \approx 1$, scattering has to be derived with rigorous EM theory. Figure 3.4 illustrates the scattering distribution at $\lambda = 0.5$ μm, on spherical particles suspended in air with size $10^{-4}\mu$m,0.1μm and 1μm. The smaller particles scatter more evenly in the back- and forward direction, whereas the larger particles have a larger forward scattering with more complex patterns. The Lorenz-Mie scattering theory is developed for spherical particles from the
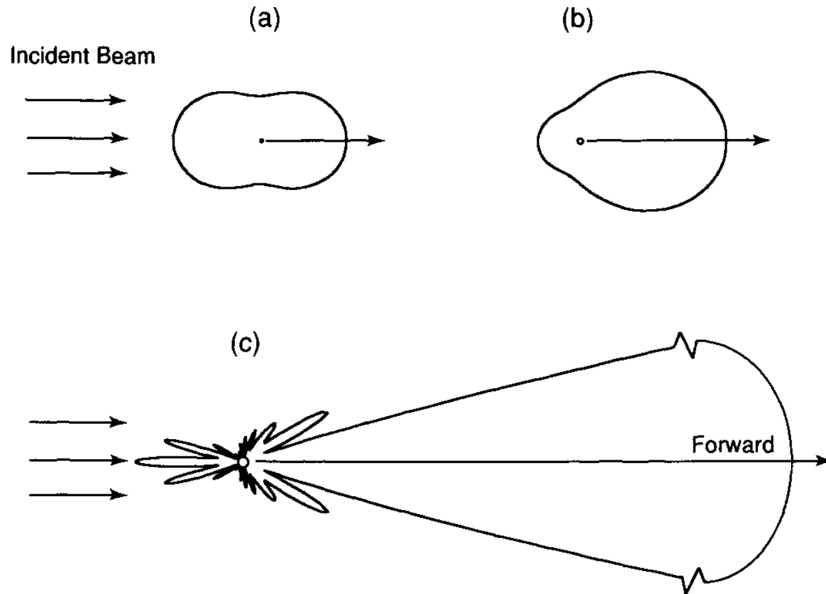

Figure 3.4: Scattering patterns from radiation of wavelength 0.5μm from three differently sized spherical particles, (a) $10^{-4}\mu$m, (b) 0.1μm and (c) 1μm where the forward scattering is scaled for presentation purposes. Reprinted from Liou (2002) with permission from Elsevier, Copyright (2002).

electromagnetic wave equations. The derivation of the scattering efficiency $Q_{s,\lambda}$, solved for a far-field approximation, is obtained as

$$Q_{s,\lambda} = \frac{\sigma_{s,\lambda}}{\pi r^2} = \frac{2}{x^2} \sum_{n=0}^{\infty} (2n+1)(\|a_n\|^2 + \|b_n\|^2), \qquad (3.8)$$

where the a_n and b_n coefficients are called the Mie-coefficients and depend on the Legendre polynomials as well as the particle size and the refractive index. The phase function for Lorenz-Mie scattering is also dependent upon the Legandre

polynomials and can be expressed in terms of the Mie-coefficients. In figure 3.5 the scattering efficiency $Q_{s,\lambda}$ is illustrated for different imaginary parts of the refractive index as a function of the particle size parameter. The size regime between $0.1 \leqslant x \leqslant 50$ is called the Mie regime where Lorenz-Mie scattering is applied. Larger size parameters $x > 50$, are treated with geometric optics.
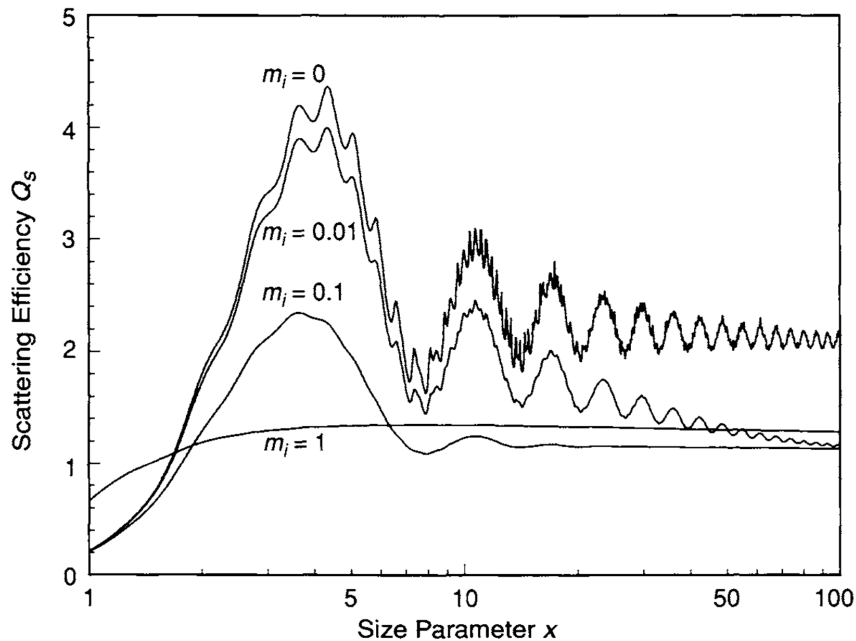

Figure 3.5: Lorenz-Mie scattering efficiency, $Q_s = \sigma_s/(\pi r)$ as a function of the size parameter x and different imaginary parts of the refractive index, m_i. Reprinted from Liou (2002) with permission from Elsevier, Copyright (2002).

When studying radiative transfer and scattering by molecules, aerosols and cloud droplets, the parameters that are used as input for radiative transfer modelling are the optical depth, the phase function and the single scattering albedo. As mention before, the phase function describes the angular distribution of the scattered intensity, and it is parameterised with the help of an asymmetry parameter g, which sometimes is used to represent the phase function. g relates the amount of forward and backward scattering and ranges from $-1 < g < 1$. For Rayleigh scattering, the scattering is isotropic and therefore $g = 0$. If $g > 0$, more forward scattering is present, whereas $g < 0$ indicates more backward scattering. The single scattering albedo, commonly denoted by ω, is defined as the ratio of the scattering and total extinction (scattering plus absorption) cross sections.

3.3 Radiative transfer equation

In the previous section, the change of spectral intensity, due to the attenuation from absorption and scattering, was introduced in equation 3.3. In this section, we generalise this expression by introducing a source term (note that

monochromatic intensities are still considered, but the wavelength index has been omitted),

$$\mu \frac{dI(\tau;\mu,\phi)}{d\tau} = \underbrace{-I(\tau;\mu,\phi)}_{\text{sink term}} + \underbrace{J(\tau;\mu,\phi)}_{\text{source term}} \quad (3.9)$$

where τ is the optical depth (from eq. 3.4), $\mu = \cos\theta$, θ is the zenith angle, and ϕ is the azimuthal angle. The sink term includes the attenuation due to absorption and scattering, whereas the source terms includes both emission, single and multiple scattering into the line of sight. When including multiple scattering, the incoming spectral intensity is traditionally divided into two components, a direct solar and diffuse component, $I = I_{\odot} + I_d$. Where the diffuse component comes from single and multiple scattering.The direct spectral intensity can only come into the observed line of sight through a single forward scattering event. The expression in 3.9 then becomes,

$$\mu \frac{dI_d(\tau;\mu,\phi)}{d\tau} = I_d(\tau;\mu,\phi) - \underbrace{\frac{\omega}{4\pi} \int_0^{2\pi} \int_{-1}^{1} I_d(\tau;\mu',\phi')P(\mu,\phi;\mu',\phi')d\mu'd\phi'}_{\text{multiple scattering}} \quad (3.10)$$

$$- \underbrace{\frac{\omega}{4\pi}F_{\odot}P(\mu,\phi;\mu_0,\phi_0)e^{-\tau/\mu_0}}_{\text{single scattering}} - \underbrace{(1-\omega)B[T(\tau)]}_{\text{emission}} \quad (3.11)$$

where $F_{\odot}$ is the solar flux density [W/m^2] and $(1-\omega)$ is the co-albedo representing the emissivity, since Kirchoffs's law is valid under LTE. As mentioned in the previous section, to solve the radiative transfer equation (RTE), the optical depth, phase function and the single scattering albedo are needed; they are usually retrieved from different data bases where they are calculated for different atmospheric species and wavelengths.

When solving the RTE for the troposphere, one need to include both scattering and absorption,account for LTE and consider a non-homogeneous medium. Solving the RTE for such a medium is computationally difficult, since there are few analytical solutions. Radiative transfer models are therefore developed for different applications like remote sensing or climate studies, using different approximations to numerically simplify the derivation of solutions.

3.4 The radiative energy budget

The radiative energy budget of the Earth refers to the energy balance at the top of the atmosphere, where the difference between the incoming radiation/energy, predominantly coming from the sun, and outgoing radiation/energy, mostly coming from the Earth system and partly reflected solar energy, are taken into account. Figure 3.6 illustrates the global annual mean energy balance on Earth and how the radiative energy is distributed within the Earth system.

If the energy budget is imbalanced, the temperature of the Earth will either experience an increase or a decrease, which undoubtedly affects the climate. A common metric used to quantify this imbalance is referred to as radiative forcing, RF. The radiative forcing is defined as the net change (down minus up)
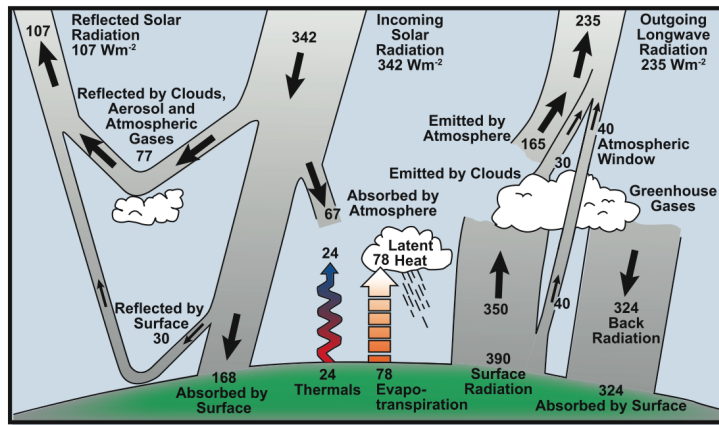
Figure 3.6: An estimate of Earth's global annual mean energy balance. Where the incoming solar radiation and out going long wave radiation interacts with different parts of the Earth system (Myhre et al. 2013).

in the radiative flux [w/m^2] due to some imposed perturbation (Myhre et al. 2013). There are different ways of deriving the radiative forcing. In the latest report from the Intergovernmental Program on Climate Change (IPCC) from 2013, Myhre et al. (2013), the radiative forcing was defined as the net change in irradiance at the tropopause after allowing the stratosphere to readjust to the radiative equilibrium holding tropospheric state parameters fixed at the unperturbed values.

4

Observing the Atmosphere

Humankind has always observed the atmosphere for its constantly changing conditions of temperature, pressure and chemical composition, in order to be able to adapt and live with it. There are two main ways of gathering information about the atmosphere; either by using remote sensing techniques, which acquire information about an object or phenomena at a distance without being in contact with it, or by using in-situ observations.

Remote sensing usually refers to the sensor technology used from the air, gathering information about an object through analysing the energy or radiation it sends out or interacts with. Unless the temperature of an object is absolute zero, 0K or $-273\,°C$, it always reflects, emits and absorbs energy in its own unique way. This energy can be sensed in a passive or active manner. Passive sensors only collect the energy emitted or reflected by the object itself or its surrounding whereas active sensors emit radiation to study the interaction between the emitted radiation and the object or its surrounding. The development of the technology of the remote sensing used today started in the 1820s with the invention of the camera and photographs. Since then aerial photography has been used to map the Earth and new remote sensing techniques have been developed using different wavelengths and platforms. In-situ observations are defined as observations being done at the location where the instrument is situated. This broad definition of observations contains a large variety of techniques, mostly coupled to what constituent of the atmosphere is being analysed.

This chapter first focuses on remote sensing from satellites, their retrievals and uncertainties, and describing the satellite sensors used in this thesis. As a last part ground based observations are briefly mentioned together with the ground based observations network used in this thesis.

4.1   Satellite Observations

Using satellites as a platform for remote sensing, first started some 60 years ago when the satellite Sputnik 1 was sent up by the Soviet Union to broadcast radio signals and could provide information about the density of the upper atmosphere through its orbit and information about the ionosphere through the propagation of radio signals. Since then a multitude of satellites have been sent out to

revolve around and observe the Earth. In the 1990s, some of the first satellites observing a multitude of trace gases were launched. MOPITT (Measurements Of Pollutions In The Troposphere), GOME (Global Ozone Monitoring Experiment) and IMG (Interferometric Monitor of Greenhouse gases) where three of the sensors that managed to probe the atmosphere to retrieve information of many important trace gases. Today, only MOPITT is operational and will be described later in this section.

When designing a satellite observing system there are many factors that need to be taken into consideration. What should it observe, atmospheric properties, land-masses? What spatial coverage should it have? What techniques are available and what orbit would be suitable? There are numerous weather and environmental monitoring satellites, most of them having a lower orbit between 600-800 km above ground, close to the poles in order to get global coverage. These sensors use different parts of the wavelength spectrum depending on the desired species of the atmosphere to observe. Three different satellite sensors have been used in this thesis and are described in 4.1.3.

As stated above, satellite sensors do not detect the atmospheric properties or land surface properties directly, the radiative properties are first observed then a radiative transfer model or forward model is needed to retrieve the wanted properties. The following section will give a short overview of how these retrievals are being derived.

4.1.1   Retrievals

To get a physical state from a remotely sensed measurement, an inversion of the radiometric signal needs to be done. The physical principles behind the inversion is basically what is illustrated in figure 4.1. Here the electromagnetic signal, S, is recorded, at a specific wavelength after it has interacted with gases, particles or the surface, then it is inverted through a function F. The function F deals with the theories of radiative transfer. The retrieved target largely depends upon the construction of F. Depending on the target, the function F can be linear, but usually this is not.

The common complex structure of F makes it so that a desired target or parameter sometimes has to be found by using a best fit to the measured signal. For example, if the target is a detailed vertical profile of some atmospheric variable from a satellite-signal, the solution becomes non-unique due to i) the received radiance is emitted from different layers of the atmosphere, ii) the received signal often time arises from deep layers within the atmosphere (since most of the atmospheric mass is residing in the lower part of the atmosphere) and iii) the measured signal always possesses errors. As a result there are several different ways of approaching retrievals of atmospheric constituents. A common way of dealing with the non-uniqueness of the retrieval solution, is to use constraints in terms of *a priori* information. This information is based on either measurements or modelling to give a "first guess" in the retrieval process. For example an a priori concentration profile can be given to a problem to constrain how much the values can vary and to "fill in" the retrievals where the observations are sensitive Deeter (2009, 2002). When using the retrievals it is therefore important to understand how much the relative effect the a priori has on the resulting retrieval. Equation4.1, describes how much of the a priori is weighted in the retrieval compared to the measured quantity,
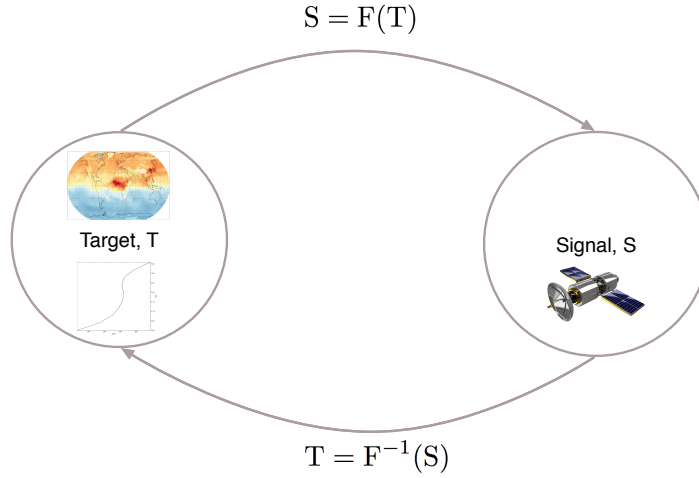
$$S = F(T)$$

$$T = F^{-1}(S)$$

Figure 4.1: Principle of retrieving a signal or a target for remote sensing. The target T represent an atmospheric state and the signal S represent a radiometric measurement.

$$x_{\mathrm{rtv}} = x_{\mathrm{a}} + A(x_{\mathrm{obs}} - x_{\mathrm{a}}) + \epsilon \qquad (4.1)$$

where x_{trv}, corresponds to the retrieved target, x_{obs} is the measured target,x_a is the a priori profile and A is an averaging kernel matrix. For an ideal retrieval the averaging kernel matrix tend towards an identity matrix. Each row of A describes the averaging kernel for each level, where each element corresponds to the relative weighting of the a priori and how the retrieved value depends on the measured value from all of the different levels. These rows are also referred to as weighting functions.

4.1.2 Satellite uncertainties

There are many uncertainties when it comes to employing satellite retrievals and for example use them to compare with model results. The first uncertainty is due to the above-mentioned a priori dependence. However, if comparing the satellite retrievals to a model data set, it is possible to add the same dependency of the a-priori to the model results by applying equation 4.1 to derive a "model-retrieval". Additional errors from the retrieval process and the measurement hardware are usually approximated within the retrievals process.

4.1.3 Satellites observing trace gases and aerosols

As mentioned before, there is a multitude of different satellites in orbit of Earth observing the atmosphere. The two largest organisations, responsible for many these satellites are the American space agency NASA (National Aeronautics and Space Administration) and the European Space Agency, ESA. Both agencies have several missions to observe the Earth. In table 4.1 some of these missions and their satellites are listed together with what they observe.

Table 4.1: List of operating satellites used to observe trace gases and aerosols through out the atmosphere, from both NASA and ESA.

Species	Sensor/Satellite (Agency)	Length of data record
CO	AIRS/Aqua (NASA)	2002–present
	IASI/MetOp (ESA)	2006–present
	MOPITT/Terra (NASA)	1999–present
O_3	AIRS/Aqua (NASA)	2002–present
	OMI/Aura (NASA)	2004–present
	GOME-2 (ESA)	2006–present
NO_2	OMI/Aura (NASA)	2004–present
	GOME-2 (ESA)	2006–present
CH_4	AIRS/Aqua (NASA)	2002–present
	IASI/MetOp (ESA)	2006–present
Aerosols	CALIOP/CALIPSO (NASA)	2006–present

In this thesis, only satellites from NASA have been used, therefore the rest of this section will be dedicated to describe NASA together with those satellites. NASA has a program called "The Earth Observation System" (EOS), which consist of a series of polar orbiting satellites aimed to monitor key components of the climate system and their interaction. In this thesis satellites with long periods of measurements are chosen. The satellites Aqua, Aura and Terra have flown in space for more than ten years and have accumulated large amounts of data with information about the atmosphere. The first two satellites are a part of the Afternoon train of satellites. This is a subset of satellites flying in a train formation with only about 20 minutes separation from the first to the last satellite. Figure 4.2 shows the A-train constellation, including Aqua and Aura. The A-train satellites all fly on an altitude of about 705 km above the Earth surface and move over the equator in the south-north direction (ascending node) between 13.30 and 13.45 local time. The Terra satellite is not a part of the A-train, it has a slightly different orbit. It flies slightly higher at 720 km and moves over the equator earlier than the A-train satellites at 10.40 in the ascending node. The following part of this section will briefly describe the sensors used from the above-mentioned satellites.

AIRS

The Atmospheric InfraRed Sounder (AIRS) is one of six instruments onboard the NASA satellite Aqua (Chahine et al. 2006). It is a hyper-spectral instrument that sounds the thermal part of the wavelengths spectrum. AIRS has several physical retrievals, among them temperature, water vapour, carbon monoxide and ozone. The goal of the AIRS mission is to support climate research and improve weather forecasting. AIRS was launched the 4 of May 2002 and has since then provided the scientific community with continuous observation through the atmospheric column. The retrieval process has developed significantly over the last decade and it is continuously being improved and evaluated.
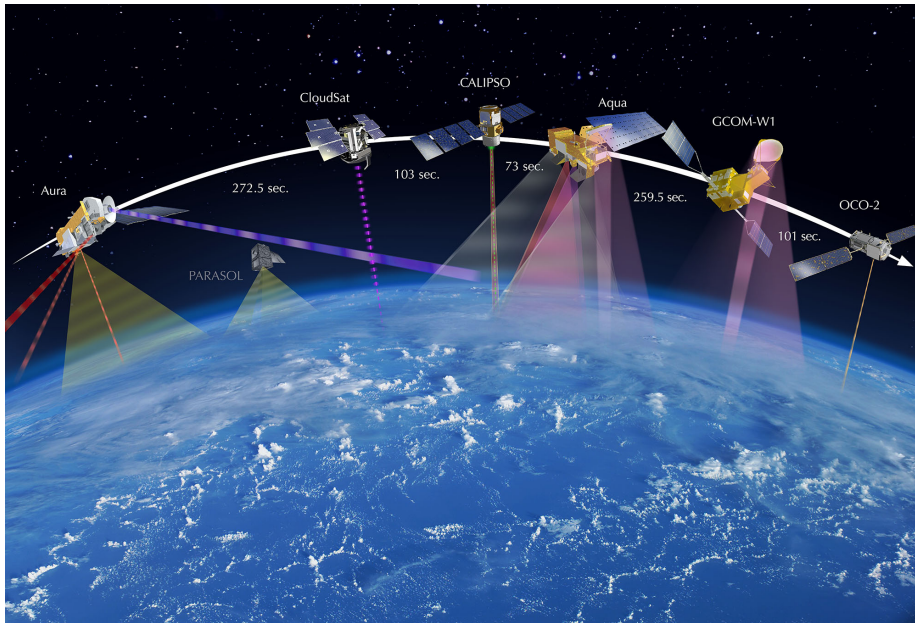
Figure 4.2: The A-train satellites used to observe the atmosphere and support the scientific community. Figure originally illustrated by NASA and *http://atrain.nasa.gov/images/A-Train_w-Time2013_Web.jpeg*

OMI

The Ozone Monitoring Instrument (OMI), is a sensor onboard the NASA satellite Aura and measures different aerosol types, cloud coverage and tropospheric ozone with a hyper-spectral imaging method, observing backscattered solar radiation form the ultraviolet and visible part of the spectrum. The OMI sensor was launched to space in 2004 and aims to observe both the "good" and the "bad" ozone, i.e. ozone form the troposphere and the stratosphere, respectively. The retrieval process is described in Kroon et al. (2011).

MOPITT

The Measurements Of Pollution In The Troposphere (MOPITT) is another instrument onboard the NASA satellite Terra and has been operational since March 2000. MOPITT is specifically designed to monitor CO in the lower part of the atmosphere. The sensor uses gas correlation spectroscopy and measures emitted and transmitted radiances in three different spectral bands. The retrieval algorithm is described by Deeter et al. (2012) and references therein.

4.2   Ground Based Observations

Observing the atmosphere from the surface of the Earth can be done in many different ways. As mentioned above, both in-situ and remote sensing methods can be used. Just as for satellites, the method depends on the type of atmospheric constituent being observed. LIDAR (LIght Detection And Ranging) is

one common remote sensing technique, where coherent radiation, usually in the ultraviolet, visible and infrared part of the solar spectrum, is used to determine atmospheric composition.

In-situ measurements are often accompanied by some type of spectroscopy, where a sample of air is collected and then studied with FTIR (Fourier Transformed InfraRed) spectroscopy, which uses infrared radiation to send through the sampled air and measure the attenuated signal.

4.2.1 Global Atmospheric Watch

The Global Atmospheric Watch (GAW) is a program developed by the World Meteorological Organisation (WMO) with the aim of providing scientific data and information about the chemical composition of the atmosphere by collecting and setting standards for scientific data from different networks and organisations. As of today, the GAW network coordinates data and activities for 30 global stations and over 400 regional stations.
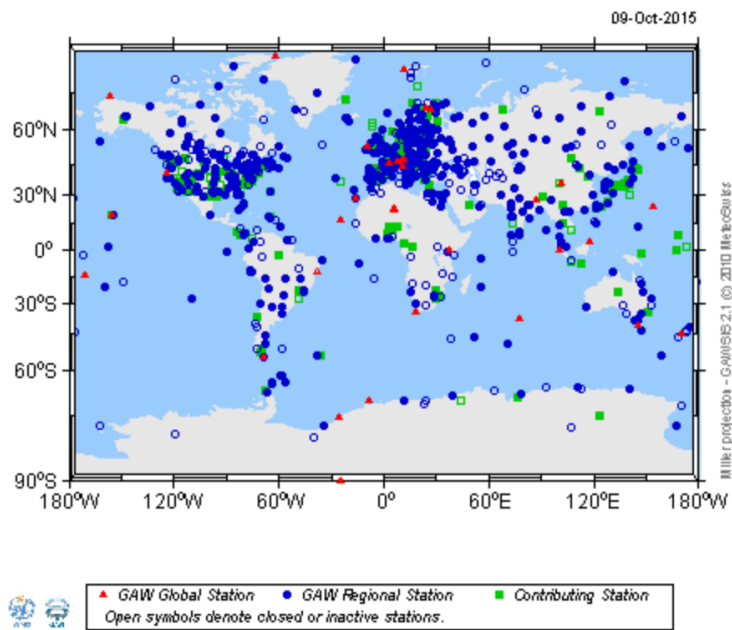

Figure 4.3: The GAW station network, including all global (red), regional (blue) and contributing (green) stations.

5

Chemical Transport
Modelling

There are different ways of modelling the atmosphere and its components. Chemical transport modelling focuses on modelling the emission, chemical transformation, transport and deposition of chemical constituents in the atmosphere. This chapter will give an overview what is considered in a chemical transport model (CTM) and give an example of how it can be used in conjunction with an aerosol optics model and in an Earth-system model.

5.1 Chemical Transport Models

5.1.1 Background

Air pollution has been a large problem since the Industrial revolution began in the 1800s, especially in urban areas where coal was widely used in factories. Different laws and regulations to control the air pollution existed during that time, but were usually too weak to make a difference. It was not until the 1950s where London experienced an episode of heavy pollution, that unarguably was damaging to human kind, that awoke awareness of the dangers of air pollution and that they needed to more strongly regulated (Mosley 2014). To understand how these regulations could be as effective as possible, one had to understand the dispersion of the pollutants and how they affect the surrounding areas. In the 1960s, dispersion models started to evolve and the first numerical model, developed to study air pollution, was called the Gaussian-Plume model and could simulate the dispersion of a point source plume. This type of model became widely used all over the world, especially for industrial pollution plumes. Later in the 1970s, it became more evident that the emitted plumes not only affected the local area, but it was transported and chemically altered during its lifetime in the atmosphere. Long-range transport models started to evolve, solving the continuity equation for mass. Solutions to the continuity equation are approached with two different frames of reference. In a Lagrangian framework an air parcel is followed and studied along a trajectory, whereas an Eulerian frame of reference looks at a specific location in the fluid and studies it in space and
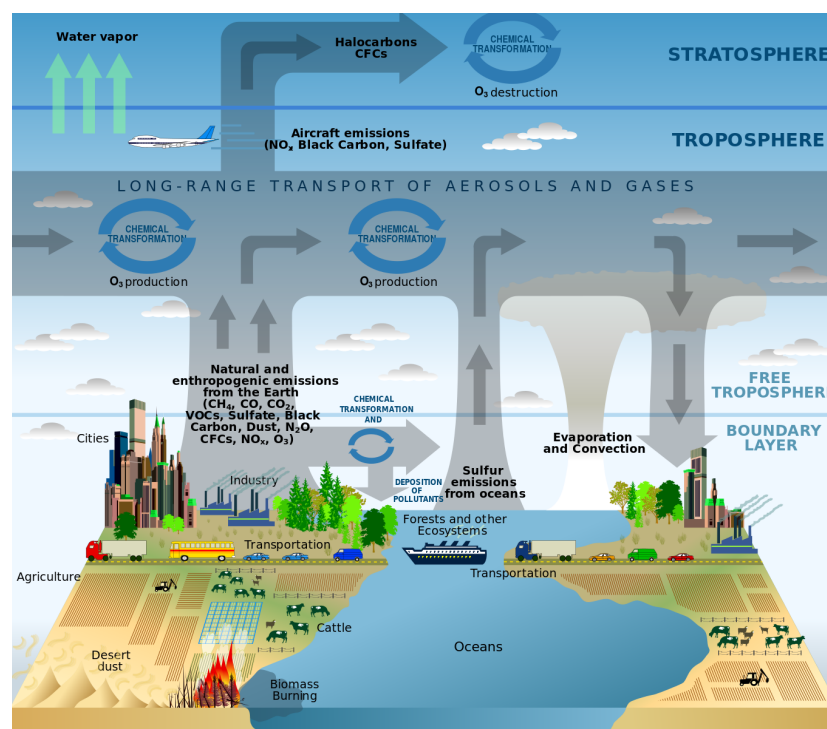
Figure 5.1: Schematic overview of the components in the Earth system that are included in an atmospheric model (Rekacewicz 2003).

time. From the beginning the Lagrangian models were used more for long-range transports over a longer period of time, whereas Eulerian models where used to study episodic events in local or urban areas (Zannetti P. and Al-Rashied 2007). Today both frameworks are widely used together with hybrid variations, like a Semi-Lagrangian model.

A 3-D model that describes the spatial and temporal variations of prescribed chemicals, using meteorological input and that solves the continuity equation, is called a chemical transport model. The aim of a CTM is to predict the concentration of atmospheric constituents by modelling the transport, chemistry, emission and deposition/sinks of the considered atmospheric constituents. Figure 5.1 shows a schematic overview of the different processes that are included in today's CTMs, and figure 5.2 shows a flow chart of how these processes are implemented and interacted within the CTM. Today, local, urban, regional and global CTMs are used to predict air quality, especially close to the surface, where the air pollution interacts with all living systems.

The following sections give a short overview of how the different atmospheric processes are accounted for in a CTM, and how CTMs can be used to study the effects of air pollution on the climate system. In the parts describing the atmospheric processes, special attention is paid to the boundary conditions in a regional CTM and how aerosol microphysics is modelled.
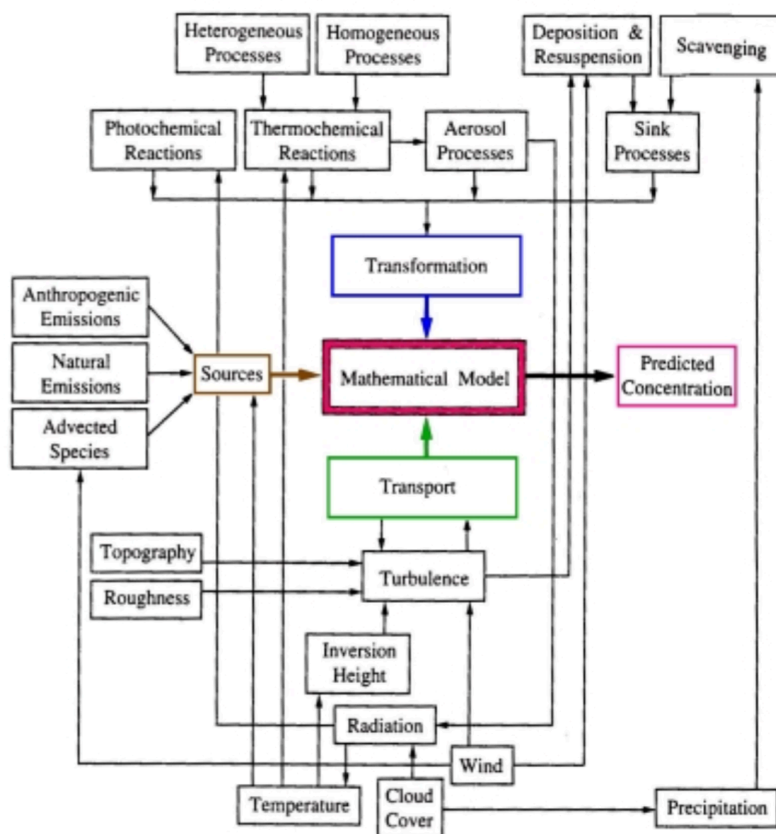
Figure 5.2: Schematic overview of the different processes involved in a mathematical chemical transport model. Originally illustrated by Seinfeld and Pandis (1998) and permission to use was given by John Wiley and Sons Ltd, Copyright(1998)

5.1.2 Atmospheric processes

All CTM models solve the equation for conservation of mass, the continuity equation to account for how the concentration fields of a chemical changes over time. All components mentioned earlier, transport, chemistry, emissions and depositions are accounted for in the following expression,

$$\frac{\partial c_i}{\partial t} + \underbrace{\nabla \cdot (\mathbf{u} c_i)}_{transport} = \underbrace{R_i(c_1, c_2, \ldots, c_n)}_{chemistry} + \underbrace{E_i}_{emission} - \underbrace{S_i}_{sinks} \tag{5.1}$$

where $c_i(\mathbf{x}, t)$ is the concentration of a chemical species varying in space and time, $\mathbf{u}(\mathbf{x}, \mathbf{t})$ is the velocity vector, R_i is the chemical generation term, $E_i(\mathbf{x}, t)$ correspond to emissions and $S_i(\mathbf{x}, t)$ the sinks in terms of deposition, (Seinfeld and Pandis 1998).

There are different ways of solving this equation, but one of the most common way is to separate each process and solve each as a separate differential equation for each time step. For example the gas-phase chemistry (including photochemistry), which is a set of n coupled ordinary differential equations, is separately solved from the transport, which deals with advection and diffusion as a mean advecting term and a turbulent diffusion term solved with a parameterisation scheme.

The coordinate system for a 3D CTM is usually a pressure based coordinate system, where the horizontal coordinates are Cartesian, but the vertical coordinate in the Cartesian system is replaced by a pressure based σ-coordinate,

$$\sigma = \frac{p - P_T}{P_S - P_T} \tag{5.2}$$

where p is the pressure at the level at which σ is defined, P_S and P_T correspond to the surface and top pressure of the model domain, respectively. This coordinate system is used instead of a complete Cartesian system, since otherwise the varying surface terrain could not be included in the model. Instead, the σ coordinate is dependent upon the surface pressure, which varies depending on the height above sea level, and a non-flat surface is taken into account in the modelling system. The coordinate system $\mathbf{x}$ will therefore consist of (x, y, σ).

Boundary conditions

To numerically solve the continuity equation in a CTM, boundary conditions are needed with the exception of using a global model domain. The non-global CTM need boundary conditions on each cardinal boundary as well as at the top and surface of the model domain. Boundary conditions heavily affect the resulting concentration fields of the model, especially if considering chemical species with a life time long enough for it to be transported across the model domain before they are updated. As cardinal and top boundaries, different models use different sets of boundary conditions. A common way of representing the inflow boundaries are through measurements, ground-based, satellite or aircraft, or from other larger scale models.

Aerosol microphysics

Chemical species that are simulated within a CTM can be in gas, liquid or solid phase. Simulating the chemical reactions in the gaseous phase is rather straight forward, since all reactions can be set up as a system of coupled ordinary differential equations. But for aerosols, there are many more physical and chemical processes involved since they are distributed with different sizes, undergo growth; through condensation and nucleation and they age; changing morphologies and hygroscopicity. Treating aerosols in a CTM model is always a compromise between how detailed the description of the aerosols should be and the computational efficiency.

A simple and commonly used way of including aerosols in a CTM is to use a mass-transport approach. In this approach, the aerosols are emitted, transported and deposited, no internal compositions or size distributions are changed. The major drawback of this approach is that no aerosol microphysics is included and therefore little can be said regarding the aerosol radiative effects, for example. This is an important consequence since one of the largest uncertainties, when it comes to understanding climate change, arises from the lack of understanding the effects aerosols have on the climate system (Myhre et al. 2013). Studies have shown that including aerosol microphysics has a large impact on the radiative properties of the aerosols such as the aerosol optical depth and the single scattering albedo (Kokkola et al. 2008, Kahnert et al. 2013). Size information is also essential for modelling the aerosols' ability to act as cloud condensations nuclei. More complex ways of simulating the aerosol microphysics in CTMs are not as common, as they are more computationally demanding, especially for operational models that are run on a regular basis for air quality forecasts and policy making. However, more aerosol dynamics modules are under development to include as many important microphysical processes as possible.

5.1.3 Model uncertainties

Simulated mass concentration fields from a CTM contain some degree of uncertainty. In general, uncertainties in CTMs comes from mainly three sources: i) physical parameterisations due to limited knowledge, or resolution, of processes such as dry deposition, biogenic emissions, and turbulent closure; ii) numerical approximations arising from grid size, time steps, or the amount of chemical species; and iii) input parameters such as meteorology, emission inventories, and land use. If defining an error as the discrepancy between model results and observations, then the errors are dependent upon the uncertainties within the model. However, since uncertainties are harder to quantify, the errors are adjusted for by tuning the model to fit the observations (Mallet and Sportisse 2006). The tuning might lead to less errors, but it does not provide any information about the uncertainties. A tuned model is therefore likely to differ substantially in its results if changing physical parameterisation, input data or numerical scheme. Quantifying the uncertainties, or the robustness, of a model can therefore be just as important as evaluating the model with observations.

5.2 Aerosol optics modelling

Modelling the optical properties of aerosols is of particular interest in climate simulation and remote sensing observations. Aerosol optics models are often used to produce data bases for different aerosol optical properties, by utilising the output aerosol concentration field from a large-scale CTM. In climate studies, the aerosol optical properties are of special interest to understand the direct radiative effect the aerosols have on the radiative balance of the Earth. In remote sensing applications, the aerosol optics model provides a conversion from the aerosol concentration field in a CTM to its optical properties, which are comparable to the radiometric output from remote sensing instruments.

Converting an aerosol concentration field to grid averaged optical properties is a complex task. Aerosols have different sizes, chemical compositions, complex morphologies and have different mixing states. Depending on the level of detailed description of the aerosol field from the CTM, the optics model needs to be adapted and make consistent use of the information at hand. The aerosol optical properties are affected by,

- the size distribution of the aerosols

- the refractive index of the aerosol, which depends on the chemicals it is composed of

- the shape or morphology.

The size distribution is given by a CTM (if it contains an aerosol dynamics module), whereas the refractive index and the morphology need to be taken care of by the optical model. The simplest and most commonly used methodology in optics model is to assume that all particles are homogeneous spheres that are externally mixed, i.e. one particle consists of only one substance. This method is widely used, not only for its simplicity and computational efficiency, but it is also of interest in data assimilation techniques, where the relationship between the mass mixing ratios and the optical properties becomes linear (Kahnert 2008). Other more complex approaches to model the particle's mixing states, chemical composition and morphologies are being used as well, but are often more computationally demanding and are in need of linearisation if used in data assimilation. The easier externally mixed methodology have, however, been shown to be a too coarse method of modelling the optical properties, and other methods are under development.

5.3 Earth-system modelling

Earth-system modelling utilises different types of models to get the best possible representations of the Earth-system as possible. The basis for an Earth-system model is a model solving all the primitive equations, i.e. all of the Navier-Stokes equations in order to simulate the atmospheric dynamics. These models are called general circulation or climate models and can be run on either global (GCM) or regional (RCM) scales. These climate models do, however, have rather coarse descriptions of many processes, such as the mass-transport. In an Earth-system model, a GCM/RCM is therefore coupled to other models such

as a CTM to get a better representation of the whole Earth-system. When coupling a CTM with a GCM/RCM, the CTM make use of the climate model simulated atmospheric dynamics as meteorological input, and the climate model employ the mass concentration fields to for example represent the aerosol-cloud processes in a better way.

6

Summary and Outlook

6.1 Summary of paper A

This study focuses on a method of evaluating lateral boundary conditions (LBCs) in regional chemical transport models. The methodology embraces two distinct parts. The first part is inspired by the work done by Henderson et al. (2014), in which LBCs are evaluated for a North American model domain by comparing global chemical transport model (CTM) data at the lateral boundaries with satellite retrievals from MOPITT and OMI for CO and ozone. We perform a similar evaluation, but over a European model domain. Here we use global CTM data from the global version of the EMEP MSC-W model. In the second part of the evaluation, we apply these LBCs to the regional CTM MATCH (Multiscale Atmospheric transport and CHemistry) model, developed by the Swedish Meteorological and Hydrological Institute (SMHI), and compare with independent data sets from the satellite sensor AIRS and ground based measurements from the GAW network. The regional model is also forced with dynamical and climatological boundary conditions derived from the global EMEP model. With this methodology we address questions that cannot be addressed fully by only evaluating the LBCs at the boundaries. More specifically, we want to address the following questions: i) Does the comparison between LBCs and satellite retrievals allow us to quantify the accuracy of the boundary values close to the surface?, ii) How much does the impact of the LBCs on in-domain concentrations differ between the surface and the free troposphere? and iii) Which improvements can one attain by using dynamic as opposed to climatological LBCs?

The results from this study gave a rather complex picture of how the LBCs affect a regional model and its in-domain concentration fields. However, the results show that the combined use of a direct (direct comparison with satellite retrievals) and indirect (driving a regional model with the evaluated LBCs and evaluate with independent in-domain observation) evaluation method provides a better analysis of the LBCs.

6.2 Summary of paper B

This paper describes the implementation of a new aerosol optics model in the large-scale CTM MATCH. The new optics model simulates more realistic particles where both external and internal mixtures are simulated. Special account is also taken to externally mixed black carbon (BC) where each BC particle is modelled as a fractal aggregate and inhomogeneous internal mixtures of BC. By inhomogeneous internal mixtures we are referring to solid BC being mixed with a liquid hydrophilic substance in a core-grey shell configuration. These two special BC treatments have shown to reproduce a more realistic amount of electromagnetic field interaction (Kahnert 2010, Kahnert et al. 2013).

We use three different ways of calculating aerosol optical properties: 1) using MATCH mass-transport model (i.e., with aerosol dynamics switched off) and a simple optics model with only externally mixed spheres; 2) using MATCH mass-transport model and the new optics model; and 3) using MATCH-Salsa (i.e., with aerosol dynamics switched on) and the new optics model. Comparing 1) and 2) we see the effects form using more realistic assumptions of particle morphologies and by comparing 2) and 3) we assess the impacts from using aerosol dynamics. The comparisons show that the effects from the new optics model are of similar magnitude as the known effects from using aerosol dynamics. This is important, since most climate and remote sensing applications today employ simplistic models to simulate aerosol optical properties.

6.3 Outlook

The goal of this thesis is to confront the MATCH model with satellite-retrieved data the results of which are presented in two studies. The first study uses satellite-retrieved data in a methodology for evaluating lateral boundary conditions (LBCs) for the relatively long-lived trace gases CO and O_3. The study showed that using this direct and indirect evaluation methodology of the LBCs with satellite retrievals, gives sufficiently robust results in the free troposphere, whereas closer to the surface inside the model domain, ground-based observations need to be employed. This study could be further expanded by investigating other trace gases, and also test if the method works well for short lived species such as NO_2.

The second study involves simulated aerosol concentration fields from MATCH. However, to this end, no satellite retrievals are used. This is because in order to compare MATCH modelled aerosol results, one needs to use an aerosol optics model to simulate radiometric properties of the aerosols, which correspond to the satellite-retrieved aerosol variables. Operational optics models today use rather coarse and simple descriptions of the particles' morphologies and compositions. This study therefore focuses on a newly developed aerosol optics model, which has the potential to produce more accurate radiometric properties of aerosols, since it uses more realistic assumptions of particle properties. These new assumptions of particle properties are, in this study, shown to impact the aerosol optical properties to the same degree as aerosol microphysics. However, since we only compare to other model simulations; in addition one should make comparisons to laboratory measurements or satellite retrievals.

As a continuation of this thesis, a combination of the two previous studies

could be done. The aim would be to evaluate boundary conditions of aerosols with satellite-retrieved information. To this end one would inversely model satellite observations to retrieve boundary fields. There are, however, challenges arising from such an approach, where the biggest one lies in the fact that the new optics model needs to be linearised.

Bibliography

Victor Blacus. `https://commons.wikimedia.org/wiki/File:` `Electromagnetic-Spectrum.svg`, 2012. Accessed 2015-10-14.

W. Cai, S. Borlace, M. Lengaigne, P. van Rensch, M. Collins, G. Vecchi, A. Timmermann, A. Santoso, M.J. McPhaden, L. Wu, M.H. England, G. Wang, E. Guilyardi, and F.F. Jin. Increasing frequency of extreme el niño events due to greenhouse warming. *Nature Climate Change*, 4:111–116, 2014. doi: 10.1038/nclimate2100.

M. T. Chahine, T. S. Pagano, H. H. Aumann, R. Atlas, C. Barnet, J. Blaisdell, L. Chen, M. Divakarla, E. J. Fetzer, M. Goldberg, C. Gautier, S. Granger, S. Hannon, F. W. Irion, R. Kakar, E. Kalnay, B. H. Lambrigtsen, S.Y. Lee, J. Le Marshall, McMillan W. W., L. McMillin, E. T. Olsen, H. Revercomb, P. Rosenkranz, W. L. Smith, D. Staelin, L. L. Strow, J. Susskind, D. Tobin, W. Wolf, and L. Zhou. Airs: Improving weather forecasting and providing new data on greenhouse gases. *B. Am. Meteorol. Soc.*, 87:911–926, 2006.

M. N. Deeter, H. M. Worden, D. P. Edwards, J. C. Gille, and A. E. Andrews. Evaluation of MOPITT retrievals of lower-tropospheric carbon monoxide over the united states. *J. Geophys. Res.*, 117:D13306, 2012.

Meeritt Deeter. *MOPITT (Measurement of Pollution in the Troposphere) Validated Version 4 Product User's Guide.* National Centre for Atmospheric Research, Boulder, CO 80307, 2009.

Merritt N. Deeter. *Calculation and Application of MOPITT Averaging Kernels*, 2002.

B.J. Finlayson-Pitts and J.N. Pitts Jr. *Chemistry of the Upper and Lower Atmosphere.* Acamdemic Press, 2000.

R.T. Gooby and Y. L. Yung. *Introduction*, chapter 1, page 4. Oxford University Press Inc., 2005.

Claire Granier, Bertrand Bessagnet, Tami Bond, Ariela D'Angiola, Hugo Denier van der Gon, GregoryJ. Frost, Angelika Heil, JohannesW. Kaiser, Stefan Kinne, Zbigniew Klimont, Silvia Kloster, Jean-Francois Lamarque, Catherine Liousse, Toshihiko Masui, Frederik Meleux, Aude Mieville, Toshimasa Ohara, Jean-Christophe Raut, Keywan Riahi, MartinG. Schultz, StevenJ. Smith, Allison Thompson, John van Aardenne, GuidoR. van der Werf,

and DetlefP. van Vuuren. Evolution of anthropogenic and biomass burning emissions of air pollutants at global and regional scales during the 1980–2010 period. *Climatic Change*, 109(1-2):163–190, 2011. ISSN 0165-0009. doi: 10.1007/s10584-011-0154-1. URL http://dx.doi.org/10.1007/s10584-011-0154-1.

B. H. Henderson, F. Akhtar, H. O. T. Pye, S. L. Napelenok, and W. T. Hutzell. A database and tool for boundary conditions for regional air quality modeling: description and evaluation. *Geosci. Model Dev.*, 7:339–360, 2014.

M. Kahnert. Variational data analysis of aerosol species in a regional CTM: background error covariance constraint and aerosol optical observation operators. *Tellus Ser. B*, 60B:753–770, 2008.

M. Kahnert. Modelling the optical and radiative properties of freshly emitted light absorbing carbon within an atmospheric chemical transport model. *Atmos. Chem. Phys.*, 10:1403–1416, 2010.

M Kahnert, T. Nousainen, and H. Lindqvist. Models for integrated and differential scattering optical properties of encapsulated light absorbing carbon aggregates. *Optics Express*, 21:7974–7993, 2013.

H. Kokkola, H. Korhonen, K. E. J. Lehtinen, R. Makkonen, A. Asmi, S. Järvenoja, T. Anttila, A.-I. Partanen, M. Kulmala, H. Järvinen, A. Laaksonen, and V.-M. Kerminen. SALSA — a sectional aerosol module for large scale applications. *Atmos. Chem. Phys.*, 8:2469–2483, 2008.

M. Kroon, J. F. de Haan, J. P. Veefkind, L. Froidevaux, R. Wang, R. Kivi, and J. J. Hakkarainen. Validation of operational ozone profiles from the ozone monitoring instrument. *J. Geophys. Res.*, 116:D18305, 2011.

K.N. Liou. *1 - Fundamentals of radiation for atmospheric applications, 3- Absorption and Scattering of solar radiation in the atmosphere*, chapter 1,3, pages 1–36,65–115. Academic Press, 2002.

Vivien Mallet and Bruno Sportisse. Uncertainty in a chemistry-transport model due to physical parameterizations and numerical approximations: An ensemble approach applied to ozone modeling. *J. Geophys. Res.*, 111:D01302, 2006. doi: doi:10.1029/2005JD006149.

P. S. Monks. Gas-phase radical chemistry in the troposphere. *Chem. Soc. Rev.*, 34:376–395, 2005.

S. Mosley. *Environmental History of Air Pollution*, chapter 5, pages 143–169. Springer International Publishing Switzerland, 2014.

G. Myhre, D. Shindell, F.-M. Breon, W. Collins, J. Fuglestvedt, J. Huang, D. Koch, J.-F. Lamarque, D. Lee, B. Mendoza, T. Nakajima, A. Robock, G. Stephens, T. Takemura, and H. Zhang. *Anthropogenic and Natural Radiative Forcing*, chapter 8, pages 659–740. Cambridge University Press, Cambridge, United Kingdom and New York, NY, USA, 2013.

Phillipe Rekacewicz. https://commons.wikimedia.org/wiki/File:Atmosphere_composition_diagram-en.svg, 2003. Accessed: 2015-10-13.

J.H. Seinfeld and S.N. Pandis. *Atmospheric Chemistry and Physics: From Air Pollution to Climate Change.* Wiley-Interscience, John Wiley and Sons, Inc., 1998.

J. M. Wallace and P. V. Hobbs. *Radiative Transfer*, chapter 4, pages 113–144. Academic Press, Elsevier - International Geophysics Series, 2006.

D. Al-Ajmi Zannetti P. and S. Al-Rashied. *2 - Air Pollution Modelling*, chapter 2, pages 15–28. The Arab School for Science and Technology (ASST) and The EnviroComp Institute, 2007.

Paper A

Evaluation of lateral boundary conditions in a
regional chemical transport model

Authors:
E. Andersson, M. Kahnert, A. Devasthale

©

Evaluation of lateral boundary conditions in a regional chemical transport model

E. Andersson[1], M. Kahnert[1,2], and A. Devasthale[2]

[1]Department of Earth and Space Sciences, Chalmers University of Technology,
41296 Gothenburg, Sweden
[2]Swedish Meteorological and Hydrological Institute, 60176 Norrköping, Sweden

Correspondence to: E. Andersson (emma.andersson@chalmers.se)

Abstract. Hemispheric transport of air pollutants can have a significant impact on regional air quality, as well as on the effect of air pollutants on regional climate. An accurate representation of hemispheric transport in regional chemical transport models (CTMs) depends on the specification of the lateral boundary conditions (LBCs). This study focuses on the methodology for evaluating LBCs
5   of two moderately long-lived trace gases, CO and O_3, for the European model domain and over a seven year period, 2006-2012. The method is based on combining the use of satellite observations at the lateral boundary with the use of both satellite and in situ ground observations within the model domain. The LBCs are generated by the global EMEP MSC-W model; they are evaluated at the lateral boundaries by comparison with satellite observations of the Terra/MOPITT sensor (CO) and the
10 Aura/OMI sensor (O_3). The LBCs from the global model lie well within the satellite uncertainties for both CO and O_3. The biases increase below $700\,\mathrm{hPa}$ for both species. However, the satellite retrievals below this height are strongly influenced by the a priori data; hence they are less reliable than at, e.g, 500 hPa. CO is, on average, underestimated by the global model, while O_3 tends to be overestimated during winter, and underestimated during summer. A regional CTM is run with (a) the
15 validated monthly climatological LBCs from the global model; (b) dynamical LBCs from the global model; and (c) constant LBCs based on in situ ground observations near the domain boundary. The results are validated against independent satellite retrievals from the Aqua/AIRS sensor at $500\,\mathrm{hPa}$, and against in situ ground observations from the Global Atmospheric Watch (GAW) network. It is found that (i) the use of LBCs from the global model gives reliable in-domain results for O_3 and
20 CO at $500\,\mathrm{hPa}$. Taking AIRS retrievals as a reference, the use of these LBCs substantially improves spatial pattern correlations in the free troposphere as compared to results obtained with fixed LBCs based on ground observations. Also, the magnitude of the bias is reduced by the new LBCs for both trace gases. This demonstrates that the validation methodology based on using satellite observations

at the domain boundary is sufficiently robust in the free troposphere. (ii) The impact of the LBCs on ground concentrations is significant only at locations in close proximity to the domain boundary. As the satellite data near the ground mainly reflect the a priori estimate used in the retrieval procedure, they are of little use for evaluating the effect of LBCs on ground concentrations. Rather, the evaluation of ground-level concentrations needs to rely on in situ ground observations. (iii) The improvements of dynamic over climatological LBCs become most apparent when using AOT40 as a metric. Also, when focusing on ground observations taken near the inflow boundary of the model domain, one finds that the use of dynamical LBCs yields a more accurate representation of the seasonal variation, as well as of the variability of the trace gas concentrations on shorter time scales.

1 Introduction

Hemispheric transport of aerosols and trace gases receives increasing attention owing to its impact on air quality, climate and visibility. Several recent studies have focused on hemispheric transport and, related to that, the significance of lateral boundary conditions (LBCs) in regional chemical transport modelling. The growing interest in hemispheric transport has partly been prompted by an increase in the average amount of pollution that is transported over hemispheric scales (e.g. Fiore et al., 2009). Hemispheric transport can also have a strong episodic impact on regional air quality (Fiore et al., 2002; Oltmans et al., 2006). Observational data from satellites of various tracers, such as carbon monoxide (CO) (Heald et al., 2003) and ozone (O_3) (Zhang et al., 2008), corroborate that hemispheric transport of air pollutants can be important for regional and local air quality. Further, while air quality studies traditionally have a strong focus on near-surface concentration fields, climate effects of air pollution involve aerosols and radiatively active trace gases throughout the atmospheric column. Concentration fields aloft are typically even more strongly influenced by long-range transport than near-surface concentrations. Thus, in modelling systems that couple regional climate and regional air quality models (e.g. Thomas et al., 2015) hemispheric transport of pollutants is likely to play an important role.

In regional models, the impact of hemispheric transport is described by LBCs in the inflow region. The significance of LBCs for regional air quality modelling has been analysed by several investigators (e.g. Mathur, 2008; Rudich et al., 2008; Song et al., 2008). In general, the impact of LBCs on in-domain concentration fields can be quite significant; it increases with species lifetime and decreases with the transport time from the domain boundary. For instance, Barna and Knipping (2006) studied sulphate concentrations in a regional model covering the USA and Mexico; it was found that, depending on meteorological conditions and on the choice of boundary conditions, between 4–25 % of the sulphate concentration at the surface and at a location far away from the boundaries can be attributed to particulate sulphate or sulphur dioxide precursors entering the model domain at the boundaries. Jiménez et al. (2007) found that ground-level ozone concentrations on the Iberian

2

peninsula are strongly influenced by the boundary conditions of both ozone and ozone precursors. It has also been pointed out that ecologically sensitive regions can be particularly susceptible to negative impacts of air pollution (e.g. Pour-Biazar et al., 2010); in such cases the role of hemispheric air pollution transport can be even more significant.

Traditionally, regional models have often relied on prescribed boundary conditions that do not adequately capture temporal and spatial variations. This approach can be particularly problematic during episodes of elevated emissions outside the model domain, such as dust-storm episodes, volcanic eruptions, or forest fires, that are transported across the domain boundary. While global models do not face challenges related to lateral boundary conditions, they are often too coarse for investigating, e.g., regional air quality standard attainment. However, they can be used to provide boundary conditions for regional air quality models that can introduce improvements over fixed boundary conditions. For example, Tang et al. (2007) compared temporally and spatially varying boundary conditions to either time-averaged or time- and horizontally averaged boundary conditions; the regional model was run over the continental USA as well as over a smaller sub-domain with a finer resolution. The dynamic boundary conditions yielded the best correlation with aircraft observations of O_3 and CO concentrations, especially in the high-resolution model.

A direct evaluation of the boundary conditions is often complicated by the sparsity of observational data. For this reason, one often performs an indirect evaluation by comparing model results within the computational domain with observations. Tang et al. (2009) investigated the benefit of using dynamic boundary conditions derived from either ozone sonde observations or from global models to forecasting ozone concentrations in continental USA. The results confirmed that the boundary conditions can have a strong impact on simulated ozone concentrations near the surface and aloft, especially near the inflow boundary. Further, while the use of dynamic boundary conditions from global models can improve correlations between predicted and measured surface ozone, this approach can also contribute to an increased model bias.

A common problem in the evaluation of boundary conditions by comparing model results to in-domain observations is to disentangle the impact of boundary conditions from all other parameters and processes that influence the model results. Satellite observations offer a good spatio-temporal coverage, thus allowing to evaluate boundary conditions directly at the boundary. This approach has been chosen by, e.g., Henderson et al. (2014), who investigated lateral boundary conditions of ozone and carbon monoxide in a regional air quality model for the continental USA. Pfister et al. (2011) made combined use of measurements from aircraft, ozone sondes, and observations of CO and O_3 from the TES instrument onboard NASA's Aura satellite, as well as modelling results from the global model MOZART-4. The study focused on the inflow of air pollution into California during the summer months. The authors found that the global model was able to reproduce about half of the free tropospheric variability when confronted with observational data. When used as LBCs in a regional model, the variability in the pollution inflow strongly impacted the surface concentrations

3

of CO and O_3 over California. In their conclusions the authors identify the evaluation of LBCs in regional models as one of the essential elements in regional model validation studies. They found it essential to evaluate both the spatio-temporally averaged background fields and the spatial and temporal variation of the LBC. However, they also concluded that, owing to high computational demands, nesting of global/hemispheric models with regional models may not always be practicable in all types of applications.

An alternative to the use of global models is to derive LBCs from satellite observations. For instance, Pour-Biazar et al. (2011) employed ozone observations from the OMI instrument onboard NASA's Aura satellite as well as aerosol optical depth obtained from MODIS onboard NASA's Terra and Aqua satellites to produce LBCs for the regional air quality model CMAQ, which was run for the continental USA. The analysis showed significant improvements for O_3 concentrations in the free troposphere and for $PM_{2.5}$ in the boundary layer.

This study aims to evaluate LBCs from a global CTM, the EMEP MSC-W model by comparing them with satellite retrievals and by investigating the impact of the LBCs by implementing them into a regional CTM, the MATCH (Multi-scale Atmospheric Transport and CHemistry) model developed by the Swedish Meteorological and Hydrological Institute. There are a large number of regional models being used in Europe, so a robust methodology for evaluation of lateral boundary fields for the European model domain has a potentially large user community. A similar direct evaluation, on domain boundaries, was conducted by Henderson et al. (2014) over the North American domain, but no similar studies has, to our knowledge, been done over the European domain.

The evaluation methodology is divided into two major parts. First, the LBCs from the global EMEP model are directly compared at the lateral boundaries of the European model domain, with satellite retrievals from the Terra/MOPITT (Measurements Of Pollution In The Troposphere) and Aura/OMI (Ozone Monitoring Instrument) instruments. Secondly, the study investigates the impact of LBCs on regional concentration fields by applying the LBCs from the global CTM, to the regional CTM, MATCH. The MATCH model results are compared to satellite retrievals from the Aqua/AIRS (Atmospheric InfraRed Sounder) instrument as well as to ground based measurements. Using the global CTM as LBCs gives the benefits of studying the impacts of using dynamical or climatological LBCs, which would not be possible if using satellite retrievals, due to the time resolution. The latter part of the evaluation is done by addressing the following questions: (i) How strongly are concentrations near the surface influenced by the LBCs? (ii) How are the concentrations influenced aloft in the troposphere at 500 hPa? (iii) What are the benefits of using dynamic vs climatological LBCs?

The outline of this paper is as follows. Sect. 2 presents the models and the observations together with a more detailed description of the methodology of this evaluation, which is the main focus of this paper. Section 3 shows the results from the evaluation processes, and concluding remarks are given in Sect. 4.

4

2 Models, measurements and methods

2.1 The EMEP model

135 The EMEP MSC-W chemical transport model has been developed for the European Monitoring and Evaluation Programme (EMEP) at the Meteorological Synthesizing Centre West (MSC-W, see www.emep.int). The EMEP model has been specifically developed to support policy work of the Convention on Long-range Transboundary Air Pollution (CLRTAP, http://www.unece.org/env/lrtap/lrtap_h1.html). EMEP model results have played an important part in the development of emis-
140 sion reduction scenarios, for both the Convention (now comprising 51 Parties, including USA and Canada) and increasingly for the European Commission (Amann et al., 2011; Simpson, 2013).

The EMEP MSC-W model (rv4.5(svn 2868)) has been described in detail by Simpson et al. (2012) (with updates in Simpson et al., 2013; Tsyro et al., 2014). Although traditionally run on the European scale with grid-sizes of around 30–50 km (Jonson et al., 2006; Simpson et al., 2006b; Fagerli
145 and Aas, 2008; Bergström et al., 2012), the model is increasingly being used for smaller scale applications, e.g. 2–5 km grids over the UK and Norway (Vieno et al., 2010; Karl et al., 2014), or globally (Sanderson et al., 2008; Jonson et al., 2010). In standard usage, the EMEP model has 20 vertical layers extending from the ground to 100 hPa (about 16 km), using terrain-following coordinates. The lowest layer has a depth of about 90 m. Meteorological data are taken from the European
150 Centre for Medium Range Weather Forecasting Integrated Forecasts System (ECMWF-IFS) model (http://www.ecmwf.int/en/research/modelling-and-prediction).

EMEP model results for O_3 from the global model version were compared with ozone-sonde data by Jonson et al. (2010) and found to reproduce observed values. Model results for CO, generated from both the European and global scale runs, have been compared with column data from FTIR
155 measurements at six sites (Angelbratt et al., 2011). Comparisons were complicated by the 100 hPa limit of the EMEP model and the fact that some of the stations were high altitude sites (hence above the planetary boundary layer sometimes), but mean CO concentrations were captured within 10–22 % by the European-scale model, and within 1–9 % by the global model. Further description and model runs of the global EMEP model can be found in the EMEP Status Report, Fagerli et al. (2014).
160 For the present study, the EMEP model has been run on a global scale, with horizontal resolution of $1° \times 1°$ latitude/longitude. Concentrations of CO, O_3 and other components have been exported every 3 h for use as LBC's to MATCH.

2.2 The MATCH model

MATCH is a three dimensional, Eulerian offline model that has been developed at the Swedish
165 Meteorological and Hydrological Institute (SMHI). It is highly flexible and can be used for different scenarios, regions and scales. The modelling system includes a three-dimensional variational data assimilation module (Kahnert, 2008, 2009) and an aerosol dynamics model (Kokkola et al., 2008;

5

Andersson et al., 2015). Studies have been performed at both urban scales (Gidhagen et al., 2012) and regional scales (Andersson et al., 2006). As with the EMEP model, It is also part of the core services in the European air quality ensemble forecasting system that has been developed in the EU FP7-project *Monitoring Atmospheric Composition and Climate* (MACC) (http://www.gmes-atmosphere.eu/about/project_structure/regional/r_ens/). For full descriptions of the model, see Robertson et al. (1999) and Andersson et al. (2015).

In this study, the model is set up over Europe, covering a range of $35°$ of longitude and $43°$ of latitude in a rotated lat-lon grid, with the horizontal resolution of $1° \times 1°$. The model has 40 vertical hybrid η layers ranging from the surface up to about $13 \, \text{hPa}$. These η levels are varying at each gridpoint to better follow the topography. The meteorological input data are read every three hours, and interpolated to hourly fields. Here, analysed data from the numerical weather prediction model HIRLAM (HIigh-Resolution Limited-Area Model) (Undén et al., 2002) are used, where analysed data are available every six hours, and forecast data are available every three hours.

Boundary conditions can be specified in MATCH in three different ways. The simplest option is to specify fixed lateral values at the western, eastern, northern, southern, and top boundaries, respectively. The second option is to specify vertical boundary profiles at discrete latitudes where the intermediate latitudes are derived by linear interpolation. The third option is to read in gridded boundary fields; one can either use dynamic boundary conditions from a large-scale model, or some climatology based on time-averaged model results or on satellite retrievals. Previously, the first two options have predominantly been used, but in this study the constant lateral boundaries for CO and O_3 are replaced by and compared to dynamic and climatological lateral boundary fields from the global EMEP model. The climatological LBCs, which are used in Sect. 3.1, consist of a monthly climatology based on data from 2006–2012, whereas the dynamic LBCs corresponds to $3 \, \text{hourly}$ data for the same period. These two different runs will henceforth be referred to as ELBCc and EL-BCd, respectively. The original LBCs (henceforth referred to as ORIG) are monthly and seasonally varying boundary conditions which partially are based on large-scale model runs reported in Näs et al. (2003) and back-trajectory analysed measurements from 1999 and EMEP stations close to the model-domain boundaries (Solberg et al., 2005). All ORIG LBCs are described and tabulated in Andersson et al. (2006).

2.3 Satellite retrievals

Following the work by Henderson et al. (2014) for the North American region where the global CTM GEOS-Chem was used to generate boundary conditions, we evaluate LBCs for the European model domain by comparison with satellite retrievals. The evaluation is done by collocating and extracting grid cells corresponding to the regional boundaries surrounding Europe, see Fig. 1; time averages are created for the period 2006–2012.
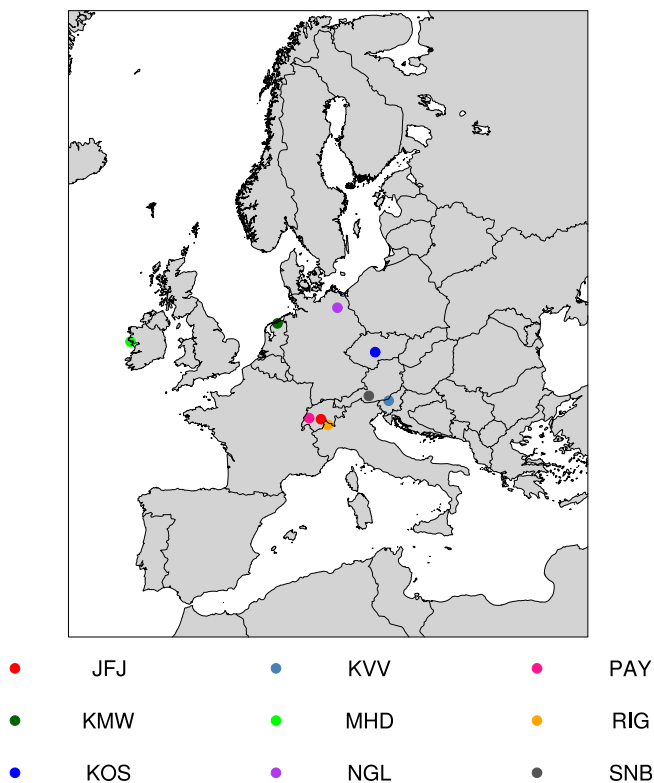
Figure 1. Map of the European model domain of the regional model, also showing the ground based measurement stations, summarised in Table 1.

The O_3 model data are compared with satellite retrievals from the OMI sensor onboard the Aura satellite. The OMI sensor uses two wavelength channels to retrieve a ozone partial column profile, OMI UV1 (270.0–308.5 nm) and the first part of OMI UV2 (311.5–330.0 nm), where the longer wavelengths at 330 nm are more affected by the changes of ozone in the troposphere (Kroon et al., 2011). The retrieval algorithm is based on the optimal estimation method (Rodgers, 2000); for full description of the retrievals see Bhartia (2002). The OMI data used in this evaluation correspond to Level 2 data, version 3 (OMO3PR), for the whole period of 2006–2012. Filtering of the data is done according to setting all the processing quality flags to zero, see the User Guide for ozone products http://disc.sci.gsfc.nasa.gov/Aura/additional/documentation/README.OMI_DUG.pdf. During the evaluation period, the OMI instrument has suffered from three different "row anomalies", the first one starting on 25 June 2007, the second one starting 11 May 2008 and the third one starting on 24 January 2009. These anomalies affect all wavelengths at certain viewing angles of OMI, but are filtered out, using the variable ReflectanceCostFunction, less than 30 (Kroon et al., 2011, J. F. de Haan, personal communication at Koninklijk Nederlands Meteorologisch Instituut, KNMI, 2015). The data was downloaded from the on-line archive (ftp://aurapar2u.ecs.nasa.gov).

7

The CO model data are evaluated against satellite retrievals from the MOPITT instrument on-board the Terra satellite. MOPITT detects CO by gas correlation radiometry and retrieves the data by a differential absorption method in two infrared spectral bands. The full description of the retrieval algorithm is found in Deeter et al. (2003). The retrieved MOPITT data used in this study correspond to Level 3 version 6, using both the thermal and near infrared spectral bands, MOP03JM with no additional filtering. MOPITT data for August and September of 2009 were not available and therefore not evaluated.

When comparing the vertical distribution of model data with satellite retrievals it is important to let the model data undergo the same degree of smoothing and get the same a priori and averaging kernel dependence as the satellite retrievals. This is done by applying Eq. (1) which is taken from the MOPITT Product User's Guide (Deeter, 2009, 2013).

$$\hat{y}_{\mathrm{rtv}} = y_{\mathrm{a}} + A(y_{\mathrm{m}} - y_{\mathrm{a}}), \tag{1}$$

where $\hat{y}_{\mathrm{rtv}}$ corresponds to retrieved or smoothed data, y_{a} is the a priori profile which is used to constrain the retrievals to fall within physically realistic solutions, A is the averaging kernel and y_{m} is the original prediction, in this case the EMEP model data. It is important to note that the averaging kernel in MOPITT is used for logarithmic concentrations fields, i.e. $\log_{10}(\mathrm{VMR})$ (Volume Mixing Ratio). This expression can also be used for the OMI data, but with the difference of using the natural logarithm (Kroon et al., 2011). This smoothing error, which is added to the model data through Eq. (1), is associated with the shape and magnitude of the measurement weighting functions and gets diminished when, either, the averaging kernels goes towards delta functions, or when the difference between y_{a} and y_{m} gets smaller (Deeter et al., 2012).

In the analysis, two months are chosen, January and August, to represent the winter and summer season and the low and high level periods of ozone. The statistical metrics used, throughout this study, are the bias and correlation, according to Eqs. (2) and (3).

$$\mathrm{bias} = \frac{1}{N} \sum_{i=1}^{N} \frac{x_{\mathrm{m},i} - x_{o,i}}{x_{o,i}} \cdot 100\,\% \tag{2}$$

$$\mathrm{correlation} = \sum_{i=1}^{N} \frac{(x_{\mathrm{m},i} - x_{\mathrm{m,avg}}) \cdot (x_{o,i} - x_{o,\mathrm{avg}})}{\sigma_{\mathrm{m}} \cdot \sigma_o} \tag{3}$$

where N is the number of data points, x_{m} corresponds to the model data, x_o to the measurement data, x_{avg} and σ are the arrhythmic mean and standard deviation of each data set, respectively.

Retrievals from the Atmospheric InfraRed Sounder (AIRS) onboard of the Aqua satellite are employed for validating MATCH results for O_3 and CO computed with different sets of LBCs. The AIRS sensor has several physical retrievals, among them the trace gases used in this study, CO and O_3. AIRS is a hyperspectral instrument that is sounding in the thermal spectrum and provides the longest record (since 2002) of the profiles of these gases retrieved simultaneously from the same sensor, Chahine et al. (2006). Over the last decade retrieval algorithms have been continuously im-

proved and validated. The uncertainties and sensitivities are also better understood and documented (Divakarla, 2008; Fetzer, 2006; Xiong et al., 2008; McMillan et al., 2011; Warner et al., 2013). We used the monthly Level 3 data ($1° \times 1°$ resolution), which suits best to our purpose of evaluation (i.e. investigating the large scale statistics), from the most recent Version 6 release of the products (Texeira, 2013; Tian, 2013). Thomas and Devasthale (2014); Devasthale and Thomas (2012) have previously demonstrated the usefulness of AIRS Level 3 data in investigating the large-scale variability of CO over the northernmost part of the study area. All satellite retrievals from OMI, MOPITT and AIRS were downloaded from NASA's REVERB website (http://reverb.echo.nasa.gov/reverb).

2.4 In situ ground observations

The ground stations used in this study are summarised in Table 1 and Fig. 1. All the stations, except one, have hourly data for at least six out of the seven years 2006–2012, for both CO and O_3. The station that does not have hourly data is the Irish station Mace Head, that has continuous event data for CO between 2006–2012. All measurement data were downloaded from the GAW-WDCGG website (http://ds.data.jma.go.jp/gmd/wdcgg/wdcgg.html).

Table 1. The names and abbreviation ground measurement stations used in the evaluation of O_3 and CO in MATCH.

Name	Country	Altitude (m a.s.)	Latitude (° N)	Longitude (° E)
Jungfraujoch (JFJ)	Switzerland	3580	46.55	7.99
Kollumerwaard (KMW)	the Netherlands	0	53.33	6.28
Kosetice (KOS)	Czech Republic	534	49.58	15.08
Krvavec (KVV)	Slovenia	1720	46.30	14.53
Mace Head (MHD)	Ireland	8	53.33	−9.9
Neuglobsow (NGL)	Germany	65	53.17	13.03
Payerne (PAY)	Switzerland	490	46.82	6.95
Rigi (RIG)	Switzerland	1031	46.07	8.45
Sonnblick (SNB)	Austria	3106	47.05	12.95

3 Results

3.1 Evaluation of lateral boundary conditions

Figure 2 presents the comparison of CO at the lateral boundaries. The four columns show results for the Southern, Northern, Eastern, and Western boundaries, while the top and bottom rows show results for January and August, respectively. The original EMEP model results are represented by grey dots, the smoothed EMEP results are shown as black solid lines, and the MOPITT retrievals and the a priori estimate are depicted as solid red and dashed blue lines, respectively. The maximum
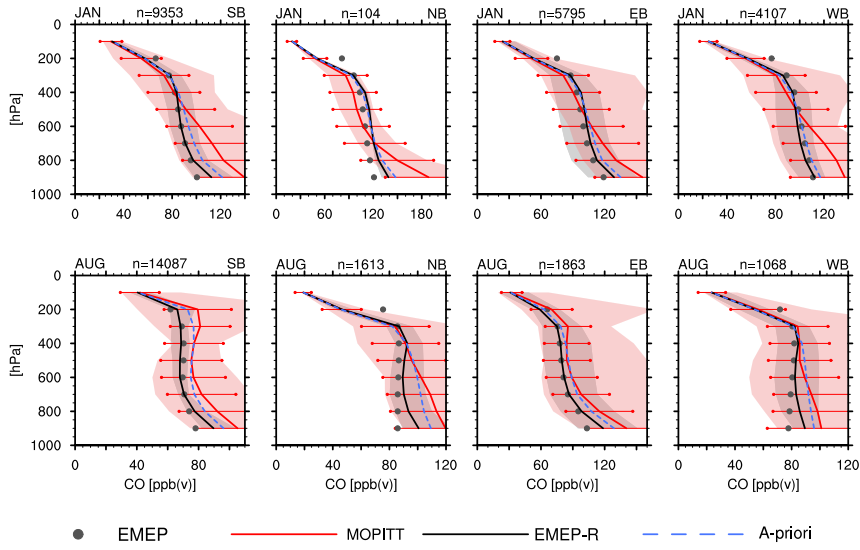
9

Figure 2. Carbon monoxide mixing ratios for January (first row) and August (second row) at the four cardinal boundaries (denoted SB, NB, EB and WB), observed by MOPITT (red solid line) and simulated retrievals from EMEP (black solid line). The retrievals (EMEP-R) are calculated by using Eq. (1) with EMEP model data (grey dots) and applying MOPITT's averaging kernel and adding the a-priori profile (blue dashed line). The red and grey shaded area correspond to the range of values in which the satellite and retrieval values vary at each level. The satellite uncertainties are represented by the red horizontal lines.

range within which the satellite retrievals and the smoothed model results vary are shown as red and grey shaded areas, respectively. The red horizontal lines represent the uncertainties of the satellite observations. As expected, the smoothed model results always lie between the original model results and the a priori estimate. Around $500\,\mathrm{hPa}$, the smoothing procedure produces results that are least influenced by the a priori; above that altitude and, even more so, near the surface, the smoothed model results are more closely following the a priori. This reflects the fact that the averaging kernel peaks in the mid-troposphere, where the satellite observations are most sensitive (Deeter et al., 2007).

The comparison of smoothed model results in Fig. 2 is complemented by Fig. 3, which illustrates the bias ranges at each altitude bin. The rows and columns are as in Fig. 2. The blue boxes represent the interquartile range, the black dotted lines show the range of bias at each altitude, and the blue line inside each box represents the median. The vertical lines represent the ± 10 and $\pm 30\,\%$ bias ranges. The most important fact we learn from Figs. 2 and 3 is that the simulated CO lies well within the uncertainties of the satellite retrievals at all four boundaries and months. Figure 3 confirms the relatively small difference between the EMEP model and the MOPITT data. The largest differences appear between EMEP and MOPITT below $700\,\mathrm{hPa}$, with an average bias of $-17\,\%$. At altitudes in the range of $700\text{–}400\,\mathrm{hPa}$, the agreement between the smoothed model results and the MOPITT retrievals tends to be least biased. As pointed out earlier, this is also the range where the instrument
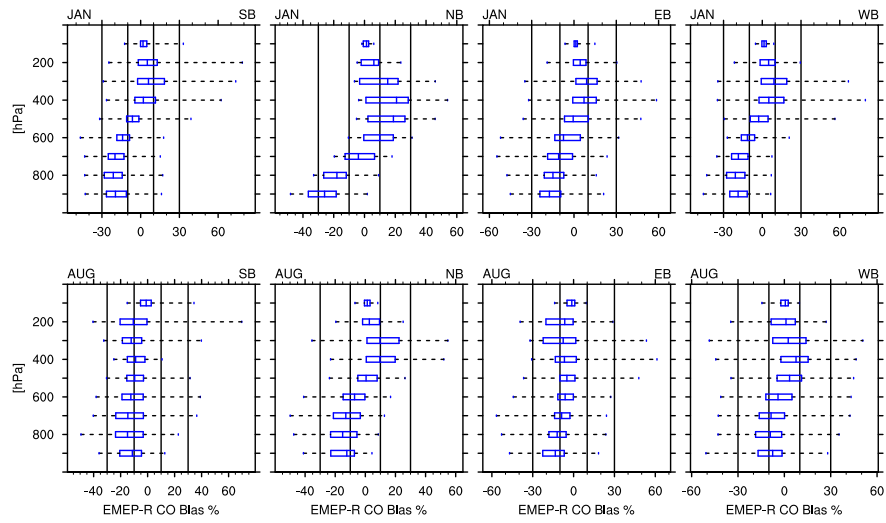
10

Figure 3. Retrieved bias for each altitude, shown as box-plots, between EMEP and MOPITT for CO and the same months and cardinal boundaries as Fig. 2. The blue boxes corresponds to the interquartile range, the black dotted lines show the range of bias at each altitude, the blue line within each box represents the median. The four black vertical lines show the ± 10 and $\pm 30\%$ bias range.
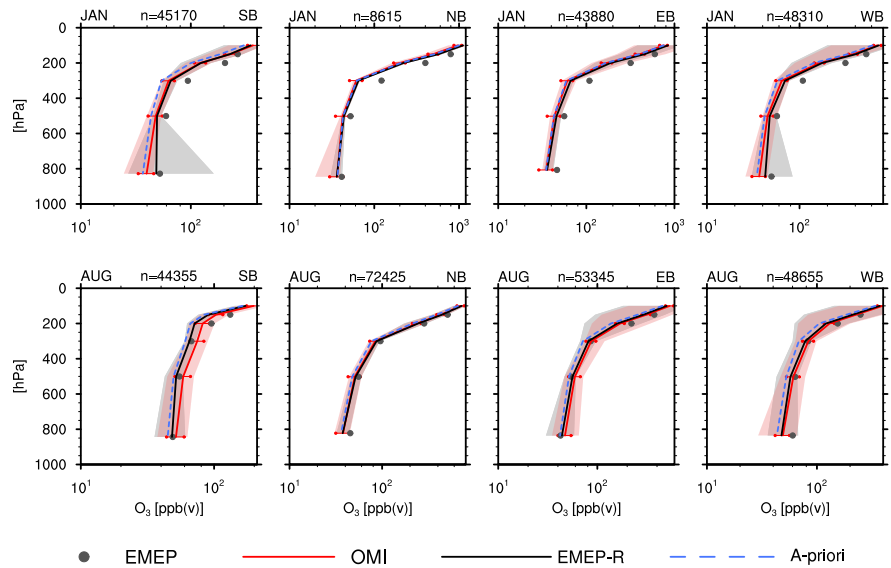

Figure 4. Same as Fig. 2 but for ozone and the satellite retrievals from OMI.
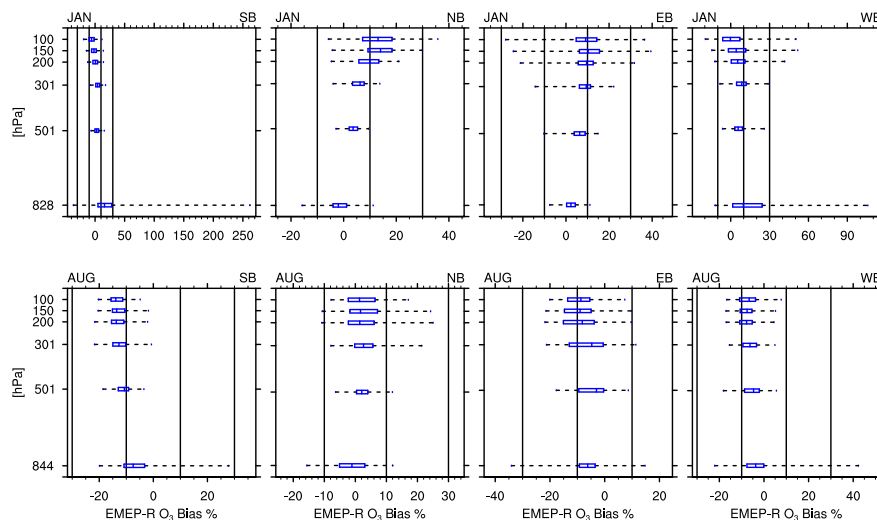
Figure 5. Same as Fig. 3, but for OMI and O_3.

is most sensitive. Hence the smoothing procedure produces results in this altitude range that rely least on the a priori estimate.

Ozone concentrations retrieved from the OMI instrument and computed by the EMEP model are found in Fig. 4, and Fig. 5 presents the corresponding bias ranges. The smoothed EMEP results for ozone lie well within the uncertainties of the satellite retrievals, except at around $800\,\mathrm{hPa}$ at the southern boundary in January. Here, Fig. 5 shows a correspondingly large bias. In January there is a general overestimation of O_3 by EMEP with an average bias of $7\,\%$, whereas the August months show an average underestimation of about $5\,\%$.

In this comparison, it is important to keep in mind the effect of the smoothing procedure. As pointed out earlier, this approach ensures that the comparison of model results and satellite retrievals is self-consistent. This is particularly important at those altitudes at which the instrument is least sensitive, which usually includes the altitude range near the surface. However, self-consistency alone does not guarantee the reliability of the validation. In the mid-troposphere, where the instruments tend to be most sensitive, the smoothing procedure alters the model results only little, and the satellite retrievals are mostly influenced by the measured signal rather than by the a priori estimate. Thus the comparison can be expected to provide us with a reliable model validation procedure at these altitudes. By contrast, near the surface both the satellite retrievals and the smoothed model results are strongly influence by the a priori estimate. It is, therefore, by no means obvious that the model validations presented in Figs. 2–5 allow us to conclude much about the reliability of the EMEP LBCs near the surface. To learn more about the effect of boundary fields on in-domain concentrations, we continue the investigation with an indirect validation of the model-derived LBCs. To this end, we force the regional MATCH model with the EMEP LBCs and compare the results to independent

12

satellite retrievals from the Aqua/AIRS instrument in the free troposphere, and to in-domain ground

315 concentrations from the GAW network. One important question in this comparison is to what extent the validation procedure we performed for the EMEP LBCs can be relied upon in the free troposphere and near the surface, respectively. We also force the MATCH model with its originally used boundary conditions (ORIG), which are based on combined use of a global model climatology and on ground observations near the lateral boundaries. We compare the independent observations to

320 MATCH results obtained with ORIG as well as with dynamic (ELBCd) and climatological (ELBCc) LBCs from the global EMEP model to assess possible improvements achieved with the validated EMEP boundary conditions, and to assess the possible benefits of using dynamic rather than climatological LBCs.

3.2 Evaluation of MATCH results near the surface

325 To better understand the impact of the new LBC at the surface, and to find out what possible benefits there might be in using dynamical vs climatological LBCs, the MATCH model runs are compared at the lowest model layer with each other and to the ground observations, in Table 1 at the surface. The model data are collocated with the measurement data by extracting the grid cell lying closest to the measurement station in latitude, longitude, and local time. For the surface comparison we

330 use a relative altitude method to extract the best corresponding model layer. This latter method is based upon the work done by Loibl et al. (1994), where the relative altitude between the stations altitude above sea level and the minimun altitude within a certain search radius, typically around 5 km, is used to find the corresponding model level. In this study the search radius is about 5 km, where the reference topography has a resolution of 1 arc-min (1.8 km) and can be found at https:

335 //www.ngdc.noaa.gov/mgg/global/global.html.

Figures 6 and 7 show the CO and O_3 results of the different MATCH model runs at the lowest model layer, averaged over the period 2006–2012. The new ELBC runs clearly show a reduction of the CO mixing ratios throughout the model domain, on average by 15 %. On the other hand O_3 increases all over the model domain, on average by 21 %.

340 To obtain information about the general behaviour of the ELBC and ORIG runs of MATCH, a comprehensive statistical analysis was done, investigating different time periods and statistical metrics for all stations. As a summary of the findings, Taylor diagrams (Taylor, 2001) were constructed, with statistics from the period 2006–2012. Figures 8 and 9 show the Taylor diagram with bias indicators, for CO and O_3. Essentially these diagrams summarise four statistical parameters,

345 the root mean square error, the correlation, the ratio between the variances (model/measurements) and the bias. The correlation is given as the cosine angle and can be read on the perimeter and have lines indicating different correlations. The root mean square corresponds to the distance from the "REF" indicator on the x axis and have dotted semicircles around this point to indicate the distance. The normalised variance, or standard deviation, is given as the radii from the origo point and are
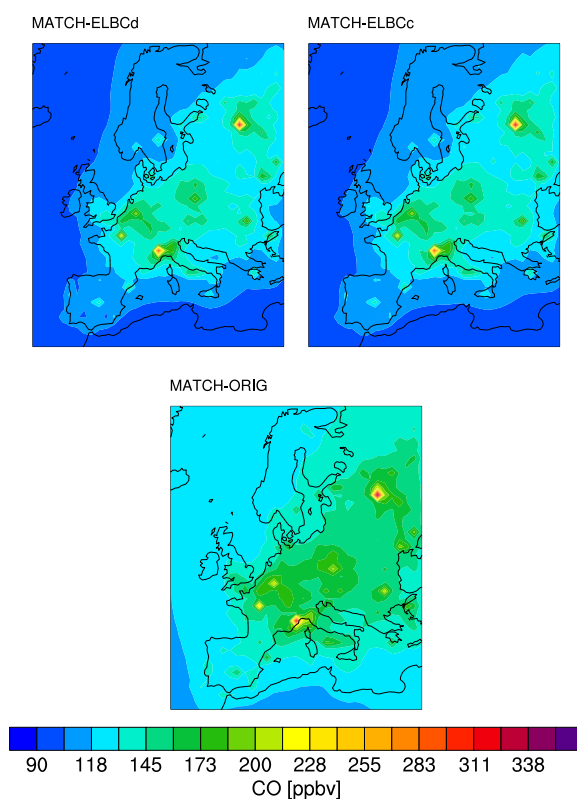
13

Figure 6. CO volume mixing ratios at the lowest model layer for the ELBCd (top left subplot), ELBCc (top right subplot) and ORIG (bottom subplot) runs of the MATCH model. The results are averaged over the entire period 2006–2012.

indicated with dashed quarter circles. The bias is indicated with markers, listed with triangles and circles in the diagram.

When changing from ORIG to ELBC, the CO results in Fig. 8 show very little change in the statistical parameters, except for the bias. The correlation gets slightly improved for three of the stations, KMW, KVV and MHD, whereas it otherwise does not change or it correlates a little bit worse. The normalised variance is low, below one, for all MATCH runs, and do not differ much between the runs. The root mean square does not change significantly either. The largest change is seen in the bias, where the new ELBC runs both underestimate the amount of CO more than the ORIG run, at all stations. These results are in line with earlier findings from Monks et al. (2015) and Stein et al. (2014). Monks did a comprehensive study, where eleven models, where inter-compared with CO, O_3 and OH, concluded a general underestimation of CO by all the models in the Arctic and the Northern Hemisphere. Stein investigated the underestimation of CO in wintertime and in the Northern Hemisphere and concluded that it partially comes from an underestimation of wintertime
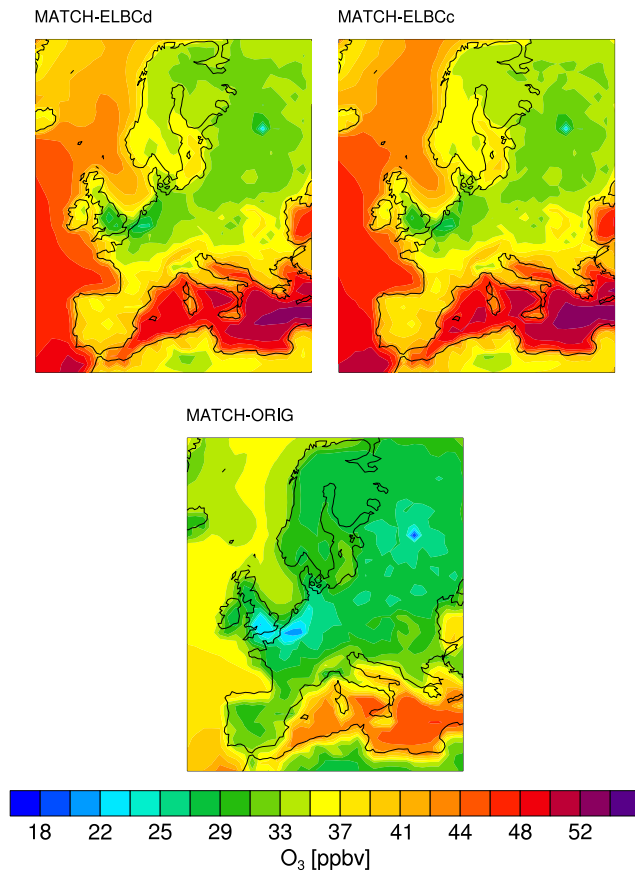
14

Figure 7. Same as Fig. 6, but for O_3.

road traffic emissions, too high dry deposition rates in boreal forests, and possibly from errors of the geographical and seasonal distribution of OH concentrations.

365   Figure 9 illustrates the summary of the O_3 statistics for the nine ground observation sites. The new ELBC MATCH model runs increase the amount of O_3 and clearly improve the variance, where the normalised standard deviation gets closer to one, "REF". The bias varies among the stations, but gets over all improved. Nevertheless, the correlation gets slightly worse for all stations except MHD, where it remains unchanged.

370   Time series of CO and O_3 corresponding to the year 2011 for all three model runs at the Mace Head station are investigated and shown in Figs. 10 and 11, respectively. These figures show the daily maximum of ozone and the CO mixing ratios at the same time of the day at which O_3 mixing ratios peak, which usually occurs in the afternoon. We chose the time of the O_3 maxima to avoid problems with nocturnal shallow boundary layers. It is evident that there are bias problems for both ELBC runs

375   and both trace gases. CO is underestimated more strongly with the new ELBC runs than the ORIG run, and O_3 is slightly more overestimated compared to the ORIG run. Examining the correlation,
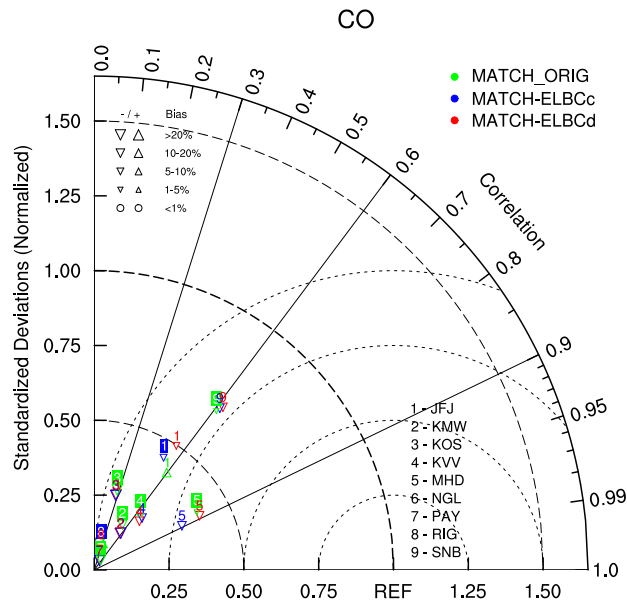
15

Figure 8. Taylor diagram showing CO statistics for all the chosen GAW stations, for the three MATCH model runs, ELBCd as red, ELBCc as blue and ORIG as green, with statistics from 2006–2012. The correlation is given by the cosine angle from the horizontal axis, the root mean square error corresponds to the distance from the "REF" indicator on the x axis, the ratio between the variances of the model and the measurements, here referred to as the normalised standard deviation and are represented by the radius or distance from the origo and the bias is symbolised next to each marker. Standard deviations larger than 1.75 are represented with their standard deviation/correlation as numbers underneath the diagram. The bias symbols are indicated in the list to the top left.

the ELBCd run captures more of the variability, especially on shorter time scales. Looking only at the summer season of 2011 the correlation is higher, 0.77 compared to 0.56 (ELBCc) and 0.59 (ORIG) for CO, and 0.72 compared to 0.64 (ELBCc) and 0.66 (ORIG) for O_3. For the year of 2011, the larger scale (seasonal) variation dominates, and the correlation is unchanged for CO and improved for O_3, 0.77 (ELBCd), 0.78 (ELBCc) and 0.66 (ORIG). The winter time O_3 is also much improved with the new ELBCs.

We have also investigated changes in a rather sensitive metric, the Accumulated Ozone over Threshold 40 ppb, AOT40 (Fuhrer et al., 1997). AOT40 is an important metric when studying ozone impact on vegetation (Fuhrer et al., 1997), it is also very sensitive to small variations in O_3 (Simpson et al., 2006a), and can thus highlight the differences among the different model runs. The AOT40 is derived for the months April to September of 2011 and at 07:00–19:00 UTC. Figure 12 shows the AOT40 for all the considered measurement stations in the model domain. Clearly the use of ELBC runs cause significant changes in the AOT40. In most cases this gives a better comparison with measurements, although it should be noted that this alone is not proof of better BCs: many
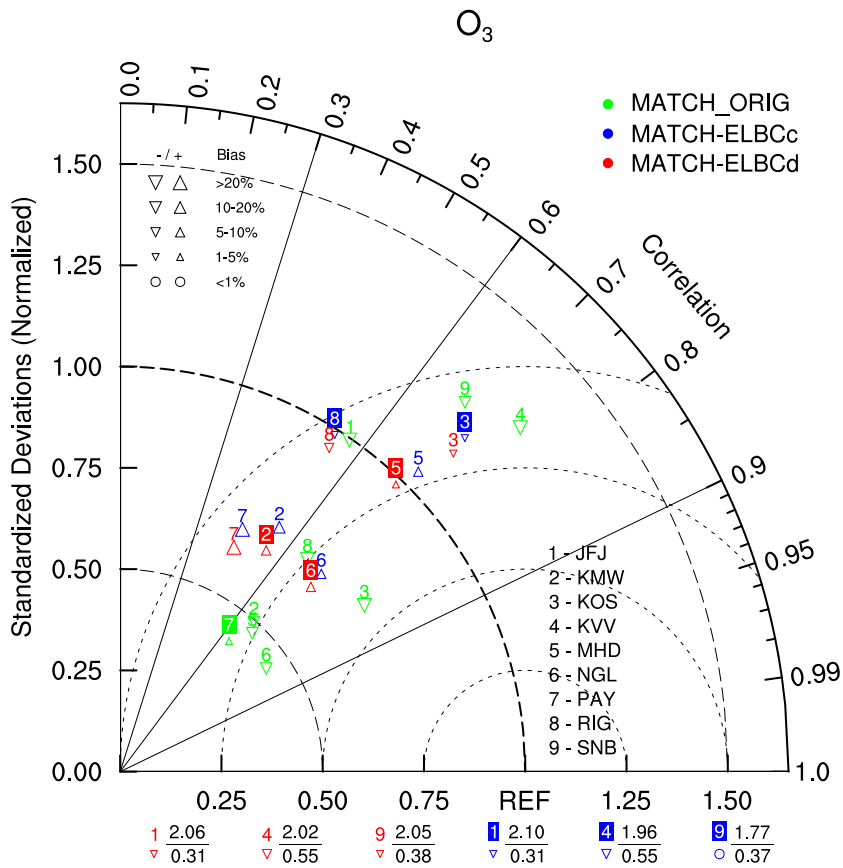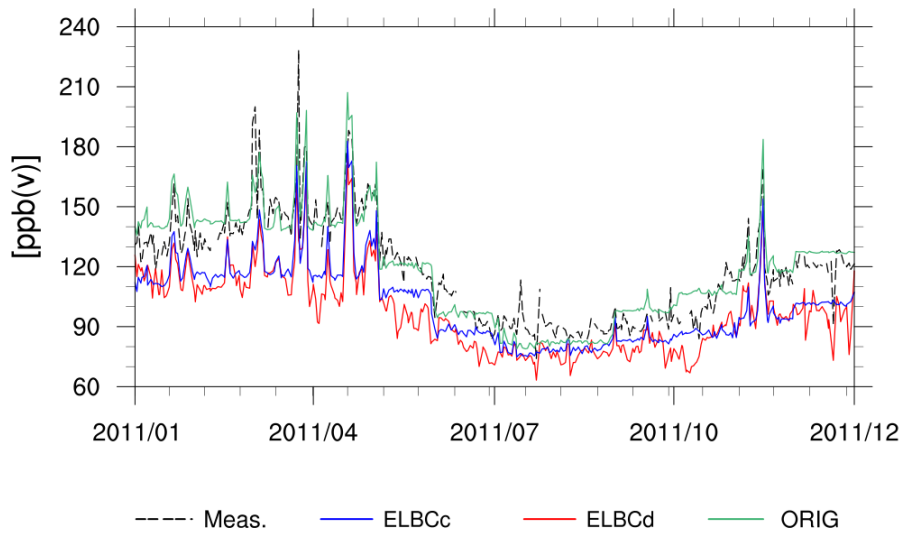
16

Figure 9. Same as Fig. 8, but for O_3.

Figure 10. Timeseries showing the summer season of 2011 for CO, at the Mace Head station.
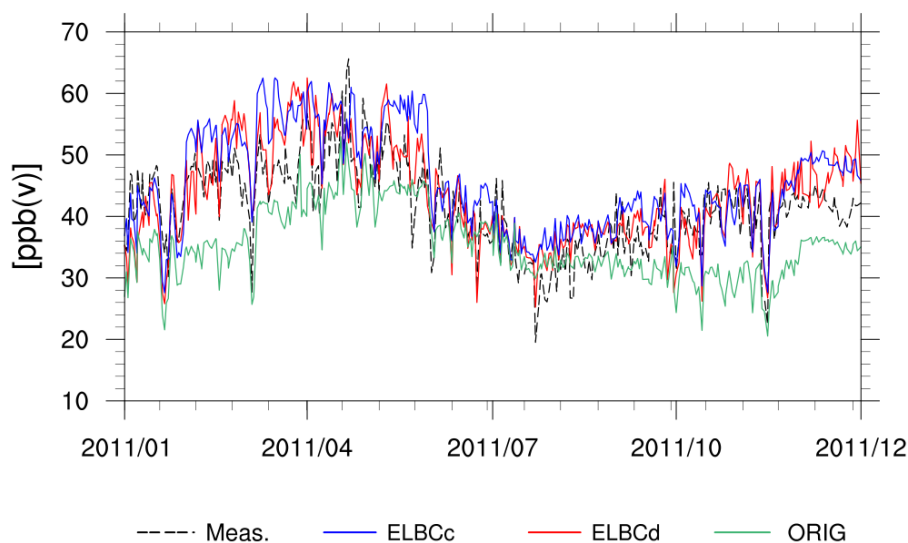
Figure 11. Same as Fig. 10, but for O_3.

other processes also affect the bias with respect to AOT40, such as dry deposition rates or chemical production rates (Tuovinen et al., 2007). The one station that deviates more from this improvement, is Mace Head, where the ORIG BCs give best results. The reason for this is most likely the use of Mace Head data in setting the values used in the ORIG BCs. The dynamic boundary conditions, ELBCd, also yield a better agreement with the observations than the climatological boundary conditions, ELBCc, at six of the nine stations. However, the ELBCc and ELBCd give rather similar AOT40 levels, suggesting that climatological ELBCs can be good enough even for this rather sensitive ozone metric. On average, the ORIG results underestimate the AOT40 by 41 % and new ELBC runs overestimates by 10 and 29 % respectively. Sensitivity tests show that (as expected) AOT40 is most sensitive to the O_3 BCs, and this is also consistent with the findings in Schulz et al. (2014), who compared the global EMEP model to the regional EMEP MSC-W model and ground based observations, and where the global EMEP model overestimates the amount of O_3 at the surface.

3.3 Evaluation of MATCH results at 500 hPa

The question we address here is how the LBCs influence the in-domain concentrations aloft in the troposphere at 500 hPa. To get a general view of how MATCH performs in the free troposphere, the mean vertical profiles for CO and O_3 are inspected. Figure 13 shows mean vertical profiles for CO and O_3 and the three MATCH runs together with the EMEP model at MATCH η levels (surface to about 13 hPa). The profiles are averaged over 2006–2012, at the Mace Head station, which again is used since it is located close to the Western boundary. The two ELBC runs and the EMEP results have similar vertical profiles, while the MATCH results obtained with the original prescribed boundary
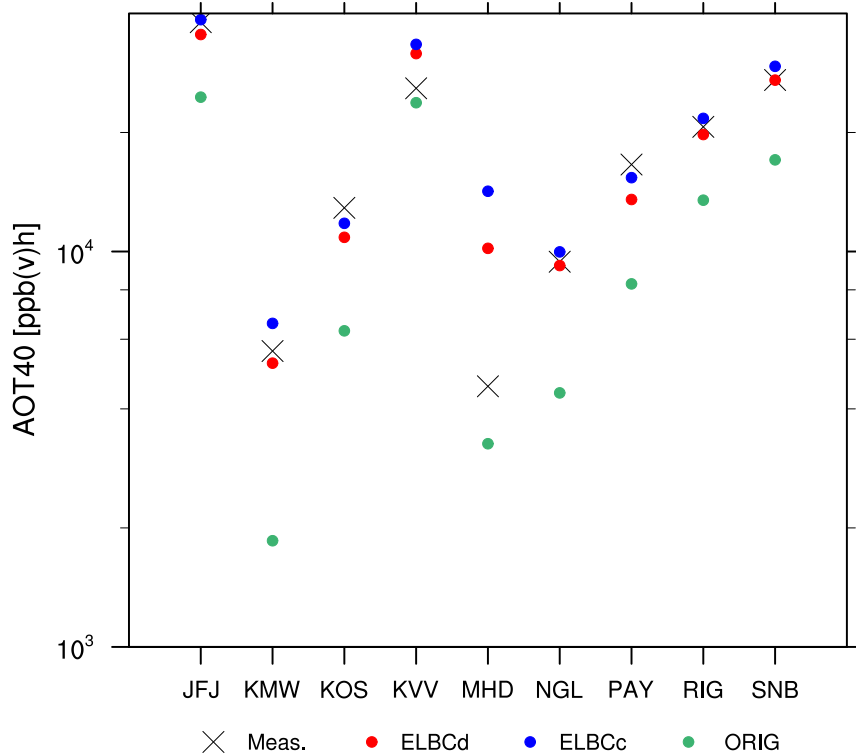
18

Figure 12. The AOT40 in ppb(v) h for the different in-domain ground based measurements stations and the different LBC setups. The AOT40 is derived for a corresponding growing season in 2011, representing the months of April to September and at 07:00–19:00 UTC.

values display a much weaker vertical variation. Judging by the satellite retrievals in Figs. 2 and 4, the vertical variation obtained with the EMEP model and with MATCH using the new boundary conditions are qualitatively more realistic than the corresponding results computed with the original boundary values, especially higher up in the free troposphere, where the difference between EMEP

415 and the satellite retrievals are smaller. Compared with the long term average of measurements (2006-2012) at the Mace Head station (represented by the black triangle), there seems to be a rather large bias for CO close to the surface, with an underestimation of about 20 % for the ELBC runs, and about 4 % for the ORIG run. As stated earlier in the comparison near the surface, many models have problems with underestimating the amounts of CO.

420 As for O_3, the new ELBC runs seem to produce too much near-surface ozone compared to the ground observations, while the ORIG run produces too little, as stated in the previous section. For this long-term mean, the ELBC runs have a positive bias of about 15 % and the ORIG a negative bias of about −9 %.
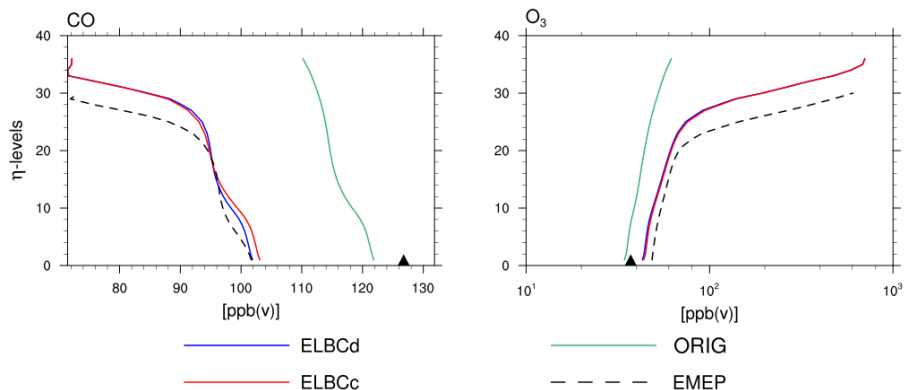
19

Figure 13. The seven year average vertical profiles at the Mace Head station location for CO (to the left) and O_3 (to the right), for the MATCH results and EMEP. The average ground based measurements at the Mace Head station is also shown as a black triangle. The levels correspond to η levels which varies with surface and model top pressure at each grid point and the pressure level 500 hPa approximately corresponds η level no. 18.

In order to gauge the significance of the differences in ozone concentrations aloft obtained with
425   the different LBCs, we take a look at how these ozone profiles translate into radiative forcing rates. To this end, we run a 1-dimensional radiative transfer model. We use a standard US atmosphere (Anderson et al., 1986), in which we replace the tropospheric ozone concentrations up to an altitude of 100 hPa by the Mace Head profiles shown in Fig. 13. We consider a dark ocean surface with a spectrally constant albedo of 7 %, and we perform the computations for a solar zenith angle of $50°$ (which
430   is typical for Mace Head around noon at equinox). We use the radiative transfer tool uvspec (Kylling et al., 1998), which is included in libRadtran, where we use DISORT (Stamnes et al., 1988) with six streams as a radiative transfer solver in conjunction with Kato's correlated k band model (Kato et al., 1999). The radiative fluxes are computed over the spectral range from 250 nm–4.5 μm. Not surprisingly, the "ELBCd" and "ELBCc" cases yield forcing rates that agree to within 99 % through-
435   out the atmospheric column. The ELBC ozone profiles yield a radiative forcing rate of $-1.8\,\mathrm{W\,m^{-2}}$ at the surface, and $+0.7\,\mathrm{W\,m^{-2}}$ well above the troposphere at 18 km altitude. By contrast the ozone profile obtained with the MATCH run based on the original LBCs yields a radiative forcing of only $-1.1\,\mathrm{W\,m^{-2}}$ at the surface, and $+0.4\,\mathrm{W\,m^{-2}}$ at 18 km. Thus the magnitude of the radiative forcing of tropospheric ozone computed with the original LBCs is considerably lower than that computed
440   with the EMEP-based LBCs.

This example clearly illustrates the impact of LBCs and concentration fields aloft on the climate forcing effect of tropospheric ozone. Thus we take a closer look at the MATCH results at 500 hPa obtained with different LBCs, and compare the simulations to independent satellite observations from AIRS. In this comparison we do not smooth the data, according to Eq. (1) as in Sect. 3.1.
445   There are primarily two reasons as to why we did not smooth the model data. First, smoothing a data
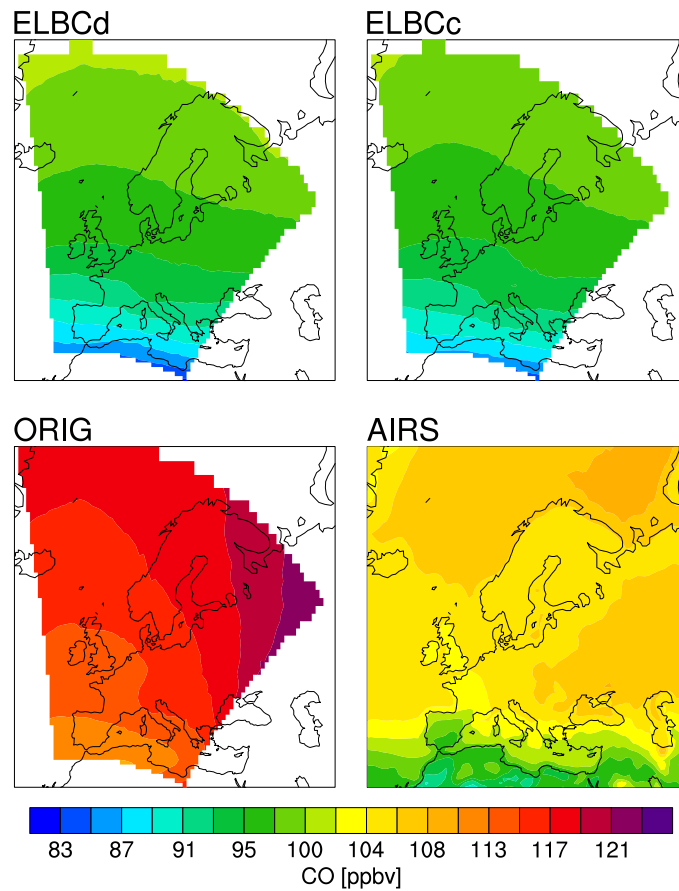
20

Figure 14. CO volume mixing ratios at $500\,\mathrm{hPa}$ for the ELBCd (top left), ELBCc (top right), ORIG (lower left) and the AIRS (lower right).

set increases the reliability of the vertical distribution, but we are only interested in one particular pressure level. Second, the chosen 500 hPa level is the level at which the satellite retrievals are least dependent upon the a-priori. Thus the a priori has very little impact on the retrieval result at that level. In addition, we are more interested in investigating the pattern correlations than the bias (which is more affected by the smoothing error). Also, it is noted that AIRS, in general, has a high sensitivity in the mid-troposphere at around $500\,\mathrm{hPa}$ (Warner et al., 2010). During the winter half year, when the surface temperatures are very cold over the study area and the lower troposphere is likely to be stratified due to inversions, the thermal contrast between the surface and successive layers in the troposphere is weakest (especially under the presence of near isothermal vertical structure). In such case, the maximum information content and averaging kernels peak around $500\,\mathrm{hPa}$ (Warner et al., 2010). This means that even in winter AIRS is most sensitive in the mid-troposphere.

Figures 14 and 15 show the three MATCH runs (ELBCd, ELBCc and ORIG) together with AIRS data at $500\,\mathrm{hPa}$, for CO and O_3 respectively, averaged over 2006–2012. The new ELBC runs clearly

21
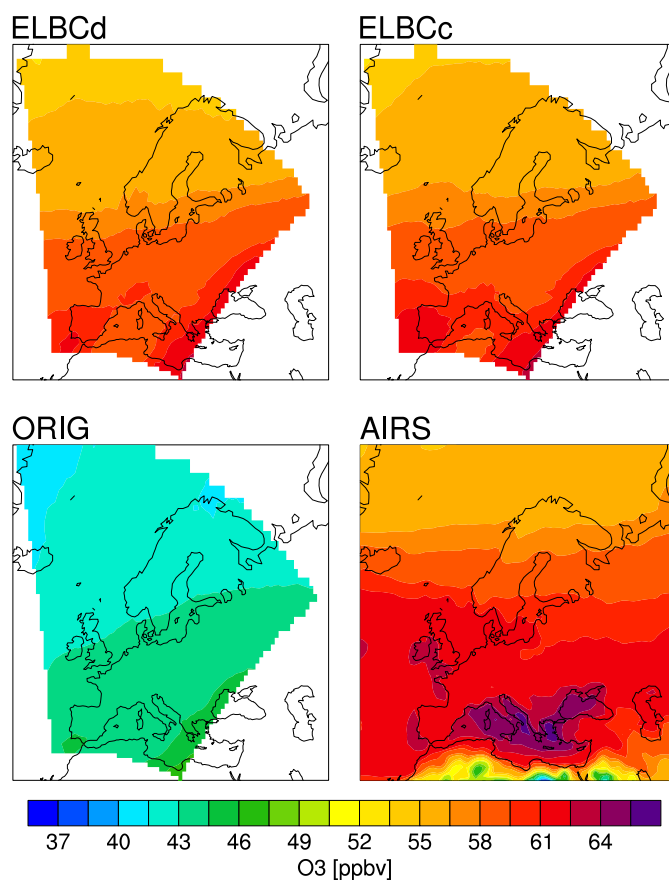
Figure 15. Same as Fig. 14, but for O_3.

impact the MATCH results. In comparison to AIRS, the CO results shows a clear improvement in

460   the pattern correlation, from 0.71 (ORIG) to 0.85 (ELBC runs); also, the north-south gradient in the

ELBC results are stronger than in the ORIG results, and compares better to the north–south gradient

in the AIRS retrievals. The ELBC runs do not deviate much from each other, much due to the long

averaging period. Looking at the time averaged variance over the model domain, the ORIG run has

three times larger variance than AIRS, whereas the ELBCs has about the same.

465   The O_3 results, in Fig. 15, also show an improvement in the north-south gradient and the pattern

correlation, 0.70 (ORIG) to 0.78 (ELBC runs). Looking at the time correlation averaged over the

2-D-domain, the best correlation is found with a lag of one to three months, meaning the ORIG run

lags about a month and the ELBCs lags three months behind the AIRS data. This is an important

observation, highlighting the need for further investigations of how the MATCH model and other

470   models are performing in the free troposphere in order to be able to couple chemical transport models

with climate models.

22

4 Conclusions

The main goal of this study was to test a methodology for evaluating lateral boundary conditions (LBCs) for the two long-lived atmospheric species CO and O_3. The methodology is based on a combined approach of performing (i) a direct comparison of LBCs derived from a global model with satellite observations at the domain boundaries, (ii) an in-domain comparison of a regional model run with satellite retrievals aloft, and (iii) and in-domain comparison of regional model runs with in situ observations at the ground. Thus our methodology combines the direct evaluation approach discussed in Henderson et al. (2014) with indirect testing methods used in various studies (e.g. Tang et al. (2007)). Boundary fields generated from the global EMEP model have, to our knowledge, not been validated previously by use of satellite data.

The direct evaluation with the global EMEP model shows good agreement, well within the uncertainties of the satellite retrievals. However, it is important to stress that the satellite data sets are retrieved with several assumptions, and they each have specific limitations, MOPITT has a lower sensitivity in the lower troposphere due to lower thermal contrasts between the surface-skin temperature and the surface-level air temperature, which leads to higher sensitivity on land, in daytime and at midlatitudes (Deeter et al., 2007). OMI has known biases, especially in the troposphere, where there are uncertainties, not only in distinguishing the tropospheric column from the stratospheric, but also how ozone is distributed in the troposphere, Kroon et al. (2011).

To illustrate the impact of the lateral boundary fields, we forced the MATCH regional CTM, set up over the European domain, with boundary fields obtained from the global EMEP model. This was done by using (a) dynamic boundary fields, and (b) "climatological" boundary fields obtained by averaging, for each month, EMEP results from a seven-year model run. The performance of the MATCH model aloft at $500\,\mathrm{hPa}$ is substantially improved with the use of the new ELBCs, where the pattern correlations increases from 0.68 (ORIG) to 0.83 (ELBC runs) for CO, and from 0.73 (ORIG) to 0.81 (ELBC runs), for O_3. Using AIRS as a reference, the model goes from a 12 % overestimation to a 9 % underestimation for CO and an underestimation of 28 % to a small overestimation of 3 % for O_3. Note, however that the bias is not considered a strong metric in this comparison at $500\,\mathrm{hPa}$, since we have not smoothed the model data.

At the surface, it was less straight forward to draw general conclusions from the direct comparison with the ground based measurements. The most significant improvements in temporal correlations are observed at Mace Head, for the ELBCd run. This station lies closest to the Western boundary; therefore it is more strongly influenced by the LBCs and less strongly by in-domain local sources. The improvements in temporal correlation are more pronounced when focusing on shorter time periods (e.g. summer season). This is consistent with Tang et al. (2007). Comparing the AOT40 results between the ELBC runs, the dynamical ELBCd setup of the LBCs produces, in general, amounts of O_3 closer to the measurements. This difference in performance between the ELBC runs can become important when studying air quality and health impacts on shorter time scales, but if

23

investigating the climate and its changes, a climatology can well represent the average amount of
510   long lived trace gases. In general the new ELBCs caused significant changes to the AOT40, where
the new ELBCs gives results closer to the measurements.

The use of a global CTM as LBCs in regional modelling certainly impacts the longer lived trace
gases both at the surface and aloft, in the free troposphere. It confirms that LBCs evaluated by satel-
lite observations at the boundary can be expected to provide accurate results in the free troposphere;
515   however, they also reveal the limitations of the methodology for ensuring the accuracy of boundary-
layer concentrations. This indicates that the significance of LBCs on ground concentration may have
been overestimated in previous studies. Even though we consider long-lived species, we find that
the LBCs influence ground concentrations only at locations in close proximity to the inflow do-
main. This makes it clear that it is not sufficient to limit the evaluation to using satellite data, and it
520   underlines the critical importance of monitoring ground concentrations near the inflow boundary.

All the datasets used in this evaluation of the LBCs, the EMEP, MOPITT and OMI data are
available upon request contacting the second author.

References

Amann, M., Bertok, I., Borken-Kleefeld, J., Cofala, J., Heyes, C., Hoeglund-Isaksson, L., Klimont, Z., Nguyen, B., Posch, M., Rafaj, P., Sandler, R., Schoepp, W., Wagner, F., and Winiwarter, W.: Cost-effective control of air quality and greenhouse gases in Europe: modeling and policy applications, Environ. Modell. Softw., 26, 1489–1501, doi:10.1016/j.envsoft.2011.07.012, 2011.

Anderson, G. P., Clough, S. A., Kneizys, F. X., Chetwynd, J. H., and Shettle, E. P.: AFGL Atmospheric Constituent Profiles (0–120 km), Tech. Rep. AFGL-TR-86-0110, AFGL (OPI), Hanscom AFB, Massachusetts 01736, 1986.

Andersson, C., Langner, J., and Bergström, R.: Interannual variation and trends in air pollution over Europe due to climate variability during 1958–2001 simulated with a regional CTM coupled to the ERA40 reanalysis, Tellus B, 59, 77–98, 2006.

Andersson, C., Bergström, R., Bennet, C., Robertson, L., Thomas, M., Korhonen, H., Lehtinen, K. E. J., and Kokkola, H.: MATCH-SALSA – Multi-scale Atmospheric Transport and CHemistry model coupled to the SALSA aerosol microphysics model – Part 1: Model description and evaluation, Geosci. Model Dev., 8, 171–189, doi:10.5194/gmd-8-171-2015, 2015.

Angelbratt, J., Mellqvist, J., Simpson, D., Jonson, J. E., Blumenstock, T., Borsdorff, T., Duchatelet, P., Forster, F., Hase, F., Mahieu, E., De Mazière, M., Notholt, J., Petersen, A. K., Raffalski, U., Servais, C., Sussmann, R., Warneke, T., and Vigouroux, C.: Carbon monoxide (CO) and ethane (C_2H_6) trends from ground-based solar FTIR measurements at six European stations, comparison and sensitivity analysis with the EMEP model, Atmos. Chem. Phys., 11, 9253–9269, doi:10.5194/acp-11-9253-2011, 2011.

Barna, M. G. and Knipping, E. M.: Insights from the BRAVO study on nesting global models to specify boundary conditions in regional air quality modeling simulations, Atmos. Environ., 40, S574–S583, 2006.

Bergström, R., Denier van der Gon, H. A. C., Prévôt, A. S. H., Yttri, K. E., and Simpson, D.: Modelling of organic aerosols over Europe (2002–2007) using a volatility basis set (VBS) framework: application of different assumptions regarding the formation of secondary organic aerosol, Atmos. Chem. Phys., 12, 8499–8527, doi:10.5194/acp-12-8499-2012, 2012.

Bhartia, P. K.: OMI Algorithm Theoretical Basis Document, Volume II, Ozone Products, NASA Goddard Space Center Greenbelt, Maryland, USA, 2002.

Chahine, M. T., Pagano, T. S., Aumann, H. H., Atlas, R., Barnet, C., Blaisdell, J., Chen, L., Divakarla, M., Fetzer, E. J., Goldberg, M., Gautier, C., Granger, S., Hannon, S., Irion, F. W., Kakar, R., Kalnay, E., Lambrigtsen, B. H., Lee, S., Le Marshall, J., W., M. W., McMillin, L., Olsen, E. T., Revercomb, H., Rosenkranz, P., Smith, W. L., Staelin, D., Strow, L. L., Susskind, J., Tobin, D., Wolf, W., and Zhou, L.: AIRS: improving weather forecasting and providing new data on greenhouse gases, B. Am. Meteorol. Soc., 87, 911–926, 2006.

Deeter, M.: MOPITT (Measurement of Pollution in the Troposphere) Validated Version 4 Product User's Guide, National Centre for Atmospheric Research, Boulder, CO 80307, 2009.

Deeter, M.: MOPITT (Measurement of Pollution in the Troposphere) Version 6 Product User's Guide, National Centre for Atmosperic Research, Boulder, CO 80307, 2013.

Deeter, M., Emmons, L., Francis, G., Edwards, D., Gille, J., Warner, J., Khattatov, B., Ziskin, D., Lamarque, J.-F., Ho, S.-P., Yudin, V., Attie, J.-L., Packman, D., Chen, J., Mao, D., and Drummond, J. R.: Operational

carbon monoxide retrieval algorithm and selected results for the MOPITT instrument, J. Geophys. Res., 108,
570   ACH1.1–ACH1.11, 2003.

Deeter, M. N., Edwards, D. P., Gille, J. C., and Drummond, J. R.: Sensitivity of MOPITT observations to carbon
monoxide in the lower troposphere, J. Geophys. Res., 112, D24, doi:10.1029/2007JD008929, 2007.

Deeter, M. N., Worden, H. M., Edwards, D. P., Gille, J. C., and Andrews, A. E.: Evaluation of MOPITT
retrievals of lower-tropospheric carbon monoxide over the United States, J. Geophys. Res., 117, D13,
575   doi:10.1029/2012JD017553, 2012.

Devasthale, A. and Thomas, M. A.: An investigation of statistical link between inversion strength
and carbon monoxide over Scandinavia in winter using AIRS data, Atmos. Environ., 56, 109–114,
doi:0.1016/j.atmosenv.2012.03.042, 2012.

Divakarla, M.: Evaluation of Atmospheric Infrared Sounder ozone profiles and total ozone retrievals with
580   matched ozonesonde measurements, ECMWF ozone data, and Ozone Monitoring Instrument retrievals, J.
Geophys. Res., 113, D15, doi:10.1029/2007JD009317, 2008.

Fagerli H. and Schulz M. and Gauss M. and Tsyro S. and Jonson J.E. and Benedictow A. and Simpson D. and
Valdebenito Á. and Griesfeller J. and Semeena V. S. and Wind P. and Olivié D. and Aas W. and Hamburger T.
and Hjellbrekke A.-G. and Solberg S. and Tørseth K. and Yttri K. E. and Karl M. and Mareckova K. and
585   Wankmüller R. and Alastuey A. and Posch M.and Tuovinen J.-P.: Transboundary particulate matter, photo-
oxidants, acidifying and eutrophying components - EMEP Status Report 1/2014, Norwegian Meteorological
Institut (MET.NO), ISSN 1504-6192, 2014

Fagerli, H. and Aas, W.: Trends of nitrogen in air and precipitation: model results and observations at EMEP
sites in Europe, 1980–2003, Environ. Pollut., 154, 448–461, 2008.

590 Fetzer, E. J.: Preface to special section: Validation of Atmospheric Infrared Sounder Observations, J. Geophys.
Res., 111, D9, doi:10.1029/2005JD007020, 2006.

Fiore, A. M., Jacob, D. J., Bey, I., Yantosca, R. M., Field, B. D., Fusco, A. C., and Wilkinson, J. G.: Background
ozone over the United States in summer: origin, trend, and contribution to pollution episodes, J. Geophys.
Res., 107, ACH11.1–ACH11.25, 2002.

595 Fiore, A. M., Dentener, F. J., Wild, O., Cuvelier, C., Schulz, M. G., Hess, P., Textor, C., Schulz, M., Do-
herty, R. M., Horowitz, L. W., MacKenzie, I. A., Sanderson, M. G., Shindell, D. T., Stevenson, D. S.,
Szopa, S., Dingenen, R. V., Zeng, R. V., Atherton, C., Bergmann, D., Bey, I., Carmichael, G., Collins, W. J.,
Duncan, B. N., Faluvegi, G., Folberth, G., Gauss, M., Gong, S., Hauglustaine, D., Holloway, T., Isak-
sen, I. S. A., Jacob, D. J., Jonson, J. E., Kaminski, J. W., Keating, T. J., Lupu, A., Marmer, E., Montanaro, V.,
600   Park, R. J., Pitari, G., Pringle, K. J., Pyle, J. A., Schroeder, S., Vivanco, M. G., Wind, P., Wojcik, G., Wu, S.,
and Zuber, A.: Multimodel estimates of intercontinental source-receptor relationships for ozone polution, J.
Geophys. Res., 114, D4, doi:10.1029/2008JD010816, 2009.

Fuhrer, J., Skärby, L., and Ashmore, M.: Critical levels for ozone effects on vegetation in Europe, Environ.
Pollut., 97, 91–106, 1997.

605 Gidhagen, L., Engardt, M., Lövenheim, B., and Johansson, C.: Modeling effects of climate change on air
quality and population exposure in urban planning scenarios, Advances in Meteorology, 12, 240894,
doi:10.1155/2012/240894, 2012.

Heald, C. L., Jacob, J., Fiore, A. M., Emmons, L. K., Gille, J. C., Deeter, M. N., Warner, J., Edwards, D. P., Crawford, J. H., Hamlin, A. J., Sachse, G. W., Browell, E. V., Avery, M. A., Vay, S. A., Westberg, D. J., Blake, D. R., Singh, H. B., Sandholm, S. T., Talbot, R. W., and Fuelberg, H. E.: Asian outflow and trans-Pacific transport of carbon monoxide and ozone pollution: an integrated satellite, aircraft, and model perspective, J. Geophys. Res., 108, D24, doi:10.1029/2003JD003507, 2003.

Henderson, B. H., Akhtar, F., Pye, H. O. T., Napelenok, S. L., and Hutzell, W. T.: A database and tool for boundary conditions for regional air quality modeling: description and evaluation, Geosci. Model Dev., 7, 339–360, doi:10.5194/gmd-7-339-2014, 2014.

Jiménez, P., Parra, R., and Baldasano, J. M.: Influence of initial and boundary conditions for ozone modeling in very complex terrains: a case study in the northeastern Iberian Peninsula, Environ. Modell. Softw., 22, 1294–1306, 2007.

Jonson, J. E., Simpson, D., Fagerli, H., and Solberg, S.: Can we explain the trends in European ozone levels?, Atmos. Chem. Phys., 6, 51–66, doi:10.5194/acp-6-51-2006, 2006.

Jonson, J. E., Stohl, A., Fiore, A. M., Hess, P., Szopa, S., Wild, O., Zeng, G., Dentener, F. J., Lupu, A., Schultz, M. G., Duncan, B. N., Sudo, K., Wind, P., Schulz, M., Marmer, E., Cuvelier, C., Keating, T., Zuber, A., Valdebenito, A., Dorokhov, V., De Backer, H., Davies, J., Chen, G. H., Johnson, B., Tarasick, D. W., Stübi, R., Newchurch, M.J., von der Gathen, P., Steinbrecht, W., and Claude, H.: A multi-model analysis of vertical ozone profiles, Atmos. Chem. Phys., 10, 5759–5783, doi:10.5194/acp-10-5759-2010, 2010.

Kahnert, M.: Variational data analysis of aerosol species in a regional CTM: background error covariance constraint and aerosol optical observation operators, Tellus B, 60, 753–770, 2008.

Kahnert, M.: On the observability of chemical and physical aerosol properties by optical observations: Inverse modelling with variational data assimilation, Tellus B, 61, 747–755, 2009.

Karl, M., Castell, N., Simpson, D., Solberg, S., Starrfelt, J., Svendby, T., Walker, S.-E., and Wright, R. F.: Uncertainties in assessing the environmental impact of amine emissions from a CO_2 capture plant, Atmos. Chem. Phys., 14, 8533–8557, doi:10.5194/acp-14-8533-2014, 2014.

Kato, S., Ackerman, T. P., Mather, J. H., and Clothiaux, E.: The k-distribution method and correlated–k approximation for a shortwave radiative transfer model, J. Quant. Spectrosc. Ra., 62, 109–121, 1999.

Kokkola, H., Korhonen, H., Lehtinen, K. E. J., Makkonen, R., Asmi, A., Järvenoja, S., Anttila, T., Partanen, A.-I., Kulmala, M., Järvinen, H., Laaksonen, A., and Kerminen, V.-M.: SALSA – a Sectional Aerosol module for Large Scale Applications, Atmos. Chem. Phys., 8, 2469–2483, doi:10.5194/acp-8-2469-2008, 2008.

Kroon, M., de Haan, J. F., Veefkind, J. P., Froidevaux, L., Wang, R., Kivi, R., and Hakkarainen, J. J.: Validation of operational ozone profiles from the Ozone Monitoring Instrument, J. Geophys. Res., 116, D18, doi:10.1029/2010JD015100, 2011.

Kylling, A., Bais, A. F., Blumthaler, M., Schreder, J., Zerefos, C. S., and Kosmidis, E.: The effect of aerosols on solar UV irradiances during the photochemical activity and solar ultraviolet radiation campaign, J. Geophys. Res., 103, 26051–26060, 1998.

Loibl, W., Winiwarter, W., Kopsca, A., and Zueger, J.: Estimaing the spatial distribution of ozone concentration in complex terrain, Atmos. Environ., 28, 2557–2566, 1994.

Mathur, R.: Estimating the impact of the 2004 Alaskan forest fires on episodic particulate matter pollution over the eastern United States through assimilation of satellite-derived aerosol optical depths in a regional air quality model, J. Geophys. Res., 113, D17, doi:10.1029/2007JD009767, 2008.

McMillan, W. W., Evans, K. D., Barnet, C. D., S., M. E., Sachse, G. W., and Diskin, G. S.: Validating the AIRS version 5 CO retrieval with DACOM in situ measurements during INTEX-A and -B, IEEE T. Geosci. Remote, 49, 2802–2813, 2011.

Monks, S. A., Arnold, S. R., Emmons, L. K., Law, K. S., Turquety, S., Duncan, B. N., Flemming, J., Huij-nen, V., Tilmes, S., Langner, J., Mao, J., Long, Y., Thomas, J. L., Steenrod, S. D., Raut, J. C., Wilson, C., Chipperfield, M. P., Diskin, G. S., Weinheimer, A., Schlager, H., and Ancellet, G.: Multi-model study of chemical and physical controls on transport of anthropogenic and biomass burning pollution to the Arctic, Atmos. Chem. Phys., 15, 3575–3603, doi:10.5194/acp-15-3575-2015, 2015.

Näs A., Moldanová J., Lindskog A., Bergström R. and Langner J.: Identification and management of critical environmental impacts from air transportation over North Europe EIATNE., EU-LIFE, Swedish Civil Aviation Administration, LIFE99 ENV/S/000631, 2003.

Oltmans, S. J., Lefohn, A. S., Harris, J. M., Tarasick, D. W., Thompson, A. M., Wernli, H., Johnson, B. J., Novelli, P. C., Montzka, S. A., Ray, J. D., Patrick, L. C., Sweeney, C., Jefferson, A., Dann, T., Davies, J., Shapiro, M., and Holben, B. N.: Long-term changes in tropospheric ozone, Atmos. Environ., 40, 3156–3173, 2006.

Pfister, G. G., Parrish, D. D., Worden, H., Emmons, L. K., Edwards, D. P., Wiedinmyer, C., Diskin, G. S., Huey, G., Oltmans, S. J., Thouret, V., Weinheimer, A., and Wisthaler, A.: Characterizing summertime chemical boundary conditions for airmasses entering the US West Coast, Atmos. Chem. Phys., 11, 1769–1790, doi:10.5194/acp-11-1769-2011, 2011.

Pour-Biazar, A., McNider, R. T., Newchurch, M., Khan, M., Park, Y. H., and Wang, L.: Evaluation of NASA AURA's data products for use in air quality studies over the Gulf of Mexico, OCS Study BOEMRE 2010–051, US Dept. of the Interior, Bureau of Ocean Energy Management, Regulation and Enforcement, Gulf of Mexico OCS Region, Huntsville, Alabama 25805, 2010.

Pour-Biazar, A., Khan, M., Wang, L., Park, Y.-H., Newchurch, M., McNider, R. T., Liu, X., Byun, D. W., and Cameron, R.: Utilization of satellite observations of ozone and aerosols in providing initial and boundary condition for regional air quality studies, J. Geophys. Res., 116, D18, doi:10.1029/2010JD015200, 2011.

Robertson, L., Langner, J., and Engardt, M.: An Eulerian limited-area atmospheric transport model, J. Appl. Meteorol., 38, 190–210, 1999.

Rodgers, C. D.: Inverse Methods for Atmospheric Sounding – Theory and Practice, World Scientific, Singapore, 2000.

Rudich, Y., Kaufman, Y. J., Dayan, U., Yu, H., and Kleidman, R. G.: Estimation of transboundary transport of pollution aerosols by remote sensing in the eastern Mediterranean, J. Geophys. Res., 113, D14, doi:10.1029/2007JD009601, 2008.

Sanderson, M., Dentener, F., Fiore, A., Cuvelier, K., Keating, T., Zuber, A., Atherton, C., Bergmann, D., Diehl, T., Doherty, R., Duncan, B., Hess, P., Horowitz, L., Jacob, D., Jonson, J., Kaminski, J., Lupu, A., Mackenzie, I., Mancini, E., Marmer, E., Park, R., Pitari, G., Prather, M., Pringle, K., Schroeder, S.,

685   Schultz, M., Shindell, D., Szopa, S., Wild, O., and Wind, P.: A multi-model study of the hemispheric transport and deposition of oxidised nitrogen, Geophys. Res. Lett., 35, L17815, doi:10.1029/2008GL035389, 2008.

Schulz, M., Jonson, J. E., Fagerli, H., and Valiyaveetil, S.: ANNEX I – Upgrade of the model framework, Tech. rep., The Norwegian Meteorological Institute, Oslo, Norway, 2014.

Simpson, D.: The EMEP MSC-W modelling programme: its relationship to policy support, current challenges

690   and future perspectives, in: Air Pollution Modelling and its Application XXII, edited by: Steyn, D., Builtjes, P., and Timmermans, R., 265–271, 2013.

Simpson, D., Ashmore, M., Emberson, L., and Tuovinen, J.-P.: A comparison of two different approaches for mapping potential ozone damage to vegetation. A model study, Environ. Pollut., 146, 715–725, doi:10.1016/j.envpol.2006.04.013 2006.

695   Simpson, D., Butterbach-Bahl, K., Fagerli, H., Kesik, M., Skiba, U., and Tang, S.: Deposition and emissions of reactive nitrogen over European forests: a modelling study, Atmos. Environ., 40, 5712–5726, doi:10.1016/j.atmosenv.2006.04.063, 2006b.

Simpson, D., Benedictow, A., Berge, H., Bergström, R., Emberson, L. D., Fagerli, H., Flechard, C. R., Hayman, G. D., Gauss, M., Jonson, J. E., Jenkin, M. E., Nyíri, A., Richter, C., Semeena, V. S., Tsyro, S.,

700   Tuovinen, J.-P., Valdebenito, Á., and Wind, P.: The EMEP MSC-W chemical transport model – technical description, Atmos. Chem. Phys., 12, 7825–7865, doi:10.5194/acp-12-7825-2012, 2012.

Simpson, D., Schulz, M., Shamsudheen, V., Tsyro, S., Valdebenito, A., Wind, P., and Steensen, B. M.: EMEP model development and performance changes, in: Transboundary acidification, eutrophication and ground level ozone in Europe in 2011, EMEP Status Report 1/2013, the Norwegian Meteorological Institute, Oslo,

705   Norway, 45–59, 2013.

Solberg S., Bergström R., Langner J., Laurila T., Lindskog A.: Changes in Nordic surface ozone episodes due to European emission reductions in the 1990s, Atmos. Env., 39, 179–192, doi:10.1016/j.atmosenv.2004.08.049, 2005.

Song, C.-K., Byun, D. W., Pierce, R. B., Alsaadi, J. A., Schaack, T. K., and Vukovich, F.: Downscale linkage of

710   global model output for regional chemical transport modeling: method and general performance, J. Geophys. Res., 113, D8, doi:10.1029/2007JD008951, 2008.

Stamnes, K., Tsay, S.-C., Wiscombe, W., and Jayaweera, K.: Numerically stable algorithm for discrete-ordinate-method radiative transfer in multiple scattering and emitting layered media, Appl. Optics, 27, 2502–2509, 1988.

715   Stein, O., Schultz, M. G., Bouarar, I., Clark, H., Huijnen, V., Gaudel, A., George, M., and Clerbaux, C.: On the wintertime low bias of Northern Hemisphere carbon monoxide found in global model simulations, Atmos. Chem. Phys., 14, 9295–9316, doi:10.5194/acp-14-9295-2014, 2014.

Tang, Y., Carmichael, G. R., Thongboonchoo, N., Chai, T., Horowitz, L. W., Pierce, R. B., Al-Saadi, J. A., Pfister, G., Vukovich, J. M., Avery, M. A., Sachse, G. W., Ryerson, T. B., Holloway, J. S., Atlas, E. L.,

720   Flocke, F. M., Weber, R. J., Huey, L. G., Dibb, J. E., Streets, D. G., and Brune, W. H.: Influence of lateral and top boundary conditions on regional air quality prediction: a multiscale study coupling regional and global chemical transport models, J. Geophys. Res., 112, D10, doi:10.1029/2006JD007515, 2007.

Tang, Y., Lee, P., Tsidulko, M., Huang, H.-C., McQueen, J. T., DiMego, G. J., Emmons, L. K., Pierce, R. B., Thompson, A. M., Lin, H.-M., Kang, D., Tong, D., Yu, S., Mathur, R., Pleim, J. E., Otte, T. L., Pouliot, G.,

725   Young, J. O., Schere, K. L., Davidson, P. M., and Stajner, I.: The impact of chemical lateral boundary condi-
tions on CMAQ predictions of tropospheric ozone over the continental United States, Environ. Fluid Mech.,
9, 43–58, 2009.

Taylor, K. E.: Summarizing multiple aspects of model performance in a single diagram, J. Geophys. Res., 106,
7183–7192, 2001.

730   AIRS   Science   Team/Texeira   J.   (2013):   Aqua   AIRS   Level   3   Monthly   Stan-
dard   Physical   Retrieval   (AIRS+AMSU),   Greenbelt,   MD,   USA:NASA   Goddard
Earth   Science   Data   and   Information   Services   Center   (GES   DISC),   Januay   2015
,doi:http://dx.doi.org/10.5067/AQUA/AIRS/DATA31910.5067/AQUA/AIRS/DATA319.

Thomas, M. A. and Devasthale, A.: Sensitivity of free tropospheric carbon monoxide to atmospheric weather
735   states and their persistency: an observational assessment over the Nordic countries, Atmos. Chem. Phys., 14,
11545–11555, doi:10.5194/acp-14-11545-2014, 2014.

Thomas, M. A., Kahnert, M., Andersson, C., Kokkola, H., Hansson, U., Jones, C., Langner, J., and Dev-
asthale, A.: Integration of prognostic aerosol–cloud interactions in a chemistry transport model coupled of-
fline to a regional climate model, Geosci. Model Dev., 8, 1885–1898, doi:10.5194/gmd-8-1885-2015, 2015.

740   Tian, B.: AIRS-V6L3UG: AIRS Version 6 Level 3 data user guide, July 2015, http://disc.sci.gsfc.nasa.gov/
AIRS/documentation/v6_docs/v6releasedocs-1/V6_L3_User_Guide.pdf, 2013.

Tsyro, S., Karl, M., Simpson, D., Valdebenito, A., and Wind, P.: Updates to the EMEP/MSC-W model, in:
Transboundary Particulate Matter, Photo-Oxidants, Acidifying and Eutrophying Components, Status Report
1/2014, the Norwegian Meteorological Institute, Oslo, Norway, 143–146, 2014.

745   Tuovinen, J.-P., Simpson, D., Emberson, L., Ashmore, M., and Gerosa, G.: Robustness of modelled ozone
exposures and doses, Environ. Pollut., 146, 578–586, 2007.

Undén, P., Rontu, L., Järvinen, H., Lynch, P., Calvo, J., Cats, G., Cuxart, J., Eerola, K., Fortelius, C., Garcia-
Moya, J. A., Jones, C., Lenderlink, G., McDonald, A., McGrath, R., Navascues, B., Nielsen, N. W., Øde-
gaard, V., Rodriguez, E., Rummukainen, M., Rõõm, R., Sattler, K., Sass, B. H., Savijärvi, H., Schreur, B. W.,
750   Sigg, R., The, H., and Tijm, A.: HIRLAM-5 Scientic Documentation, July 2015, http://www.hirlam.org,
2002.

Vieno, M., Dore, A. J., Stevenson, D. S., Doherty, R., Heal, M. R., Reis, S., Hallsworth, S., Tarrason, L.,
Wind, P., Fowler, D., Simpson, D., and Sutton, M. A.: Modelling surface ozone during the 2003 heat-wave
in the UK, Atmos. Chem. Phys., 10, 7963–7978, doi:10.5194/acp-10-7963-2010, 2010.

755   Warner, J., Carminati, F., Wei, Z., Lahoz, W., and Attié, J.-L.: Tropospheric carbon monoxide variability from
AIRS under clear and cloudy conditions, Atmos. Chem. Phys., 13, 12469–12479, doi:10.5194/acp-13-12469-
2013, 2013.

Warner, J. X., Wei, Z., Strow, L. L., Barnet, C. D., Sparling, L. C., Diskin, G., and Sachse, G.: Improved
agreement of AIRS tropospheric carbon monoxide products with other EOS sensors using optimal estimation
760   retrievals, Atmos. Chem. Phys., 10, 9521–9533, doi:10.5194/acp-10-9521-2010, 2010.

Xiong, X., Barnet, C., Maddy, E., Sweeney, C., Liu, X., Zhou, L., and Goldberg, M.: Characterization and
validation of methane products from the Atmospheric Infrared Sounder (AIRS), J. Geophys. Res., 113, G3,
doi:10.1029/2007JG000500, 2008.

Zhang, L., Jacob, D. J., Boersma, K. F., Jaffe, D. A., Olson, J. R., Bowman, K. W., Worden, J. R., Thompson, A. M., Avery, M. A., Cohen, R. C., Dibb, J. E., Flock, F. M., Fuelberg, H. E., Huey, L. G., McMillan, W. W., Singh, H. B., and Weinheimer, A. J.: Transpacific transport of ozone pollution and the effect of recent Asian emission increases on air quality in North America: an integrated analysis using satellite, aircraft, ozonesonde, and surface observations, Atmos. Chem. Phys., 8, 6117–6136, doi:10.5194/acp-8-6117-2008, 2008.

Paper B

Coupling aerosol optics to a chemical transport and aerosol dynamics model

Authors:
E. Andersson and M. Kahnert

Coupling aerosol optics to a chemical transport and aerosol dynamics model

E. Andersson[1] and M. Kahnert[1,2]

[1]Department of Earth and Space Sciences, Chalmers University of Technology, 41296 Gothenburg, Sweden
[2]Swedish Meteorological and Hydrological Institute, 60176 Norrköping, Sweden

Correspondence to: M. Kahnert (michael.kahnert@smhi.se)

Abstract. Modelling aerosol optical properties is a notoriously difficult task due to the particles' complex morphologies and compositions. Yet aerosols and their optical properties are important for Earth system modelling and remote sensing applications. Operational optics models often make drastic and non realistic approximations regarding morphological properties, which can introduce errors. In this study a new aerosol optics model is implemented, in which more realistic morphologies and mixing states are assumed, especially for black carbon aerosols. The model includes both external and internal mixing of all chemical species, it treats externally mixed black carbon as fractal aggregates, and it accounts for inhomogeneous internal mixing of black carbon by use of a novel "core-grey shell" model. Simulated results of radiative fluxes, backscattering coefficients and the Ångström exponent from the new optics model are compared with results from another model simulating particles as externally mixed homogeneous spheres. To gauge the impact on the optical properties from the new optics model, the known and important effects from using aerosol dynamics serves as a reference. The results show that using a more detailed description of particle morphology and mixing states influences the optical properties to the same degree as aerosol dynamics. This is an important finding suggesting that over-simplified optics models coupled to a chemical transport model can introduce considerable errors; this can strongly effect simulations of radiative fluxes in Earth-system models, and it can compromise the use of remote sensing observations of aerosols in model evaluations and chemical data assimilation.

1   Introduction

Aerosol optics models are employed in large-scale chemical transport models (CTMs) in mainly two contexts, namely, in Earth-system climate modelling, and in conjunction with remote sensing

1

observations. In Earth-system modelling one couples a CTM to an atmosphere-ocean general circulation model (GCM). One purpose is to account for the dynamic effects of aerosols on cloud microphysics. Another is to obtain a better description of the direct effect of aerosols and radiatively active trace gases on the radiative balance. The aerosol optics model provides a link that converts the aerosol fields delivered by the CTM to the aerosol optical properties that are required as input to the radiative transfer model, with which one computes the radiative energy budget. In remote sensing applications one is faced with the obstacle that the aerosol concentration fields computed with a CTM are not directly comparable to the radiometric quantities that are observed with remote sensing instruments. The aerosol optics model provides the observation operator that maps the CTM output to radiometric variables that can be compared to satellite observations or satellite retrieval products. This allows us to either employ satellite observations for evaluating CTM model results, or to assimilate satellite data into a CTM-based air-quality forecasting system. It is clear that the aerosol optics model has a pivotal role in these kinds of applications. It may constitute an additional source of error that could compromise the reliability of Earth-system climate models, impair the reliability of CTM evaluations, or degrade chemical data assimilation results. It is, therefore, important to better understand this potential source of error, quantify its possible impact on model predictions of aerosol radiometric quantities, and assess the level of morphological detail that is required in aerosol optics models coupled to CTMs.

A main difficulty is that aerosols in nature can have a high degree of morphological complexity. For instance, mineral dust particles can have irregular shape, small-scale surface roughness, and inhomogeneous mineralogical composition (e.g. Nousiainen (2009)). Black carbon aerosols are fractal aggregates (e.g. Jones (2006)) that can be coated by weakly absorbing liquid-phase components that condense onto the aggregates as they age in the atmosphere (e.g. Adachi and Buseck (2008)). Volcanic ash particles are composed of crustal material in which multiple air vesicles may have been trapped during the generation of the particles. In aerosol optics models one has to make a choice what level of morphological detail is necessary and affordable. A detailed discussion of this question can be found in Kahnert et al. (2014).

In environmental modelling practical and computational constraints often force us to invoke drastically simplifying assumptions about aerosol morphology. For instance, one frequently computes aerosol optical properties based on the assumption that all chemical aerosol components are contained in separate particles, and that each such particle can be approximated as a homogeneous sphere. As pointed out in Kahnert (2008); Benedetti et al. (2009), this approach is highly attractive from a practical point of view, because the aerosol optical observation operators, which map mixing ratios to radiometric properties, become linear functions of the mixing ratios of the different chemical species. A linearisation of the observation operator is a prerequisite for most of the commonly used data assimilation methodologies, such as the variational method (e.g. Kahnert (2008); Benedetti et al. (2009)). However, such approximations can also introduce substantial errors. In the remote sensing

2

community awareness for this problem has been growing over the past 1–2 decades. As a result, one

60 has developed retrieval methods for desert dust aerosols that are based on spheroidal model particles (e.g. Dubovik et al. (2006)), which can mimic the optical properties of mineral dust particles better than homogeneous spheres Kahnert (2004); Nousiainen et al. (2006). In chemical data assimilation, the problem is still treated rather negligently. A few assimilation studies account for internal mixing of different chemical components (e.g. Saide et al. (2013)). But the particles are still assumed to be

65 perfectly homogeneous spheres. To the best of our knowledge there are currently no aerosol optical observation operators in chemical transport models that take complex morphological properties of aerosols such as nonsphericity or inhomogeneous internal structure into account.

This study describes the coupling of two different aerosol optics models to a regional CTM. One optics model is based on the simple external-mixture and homogeneous-sphere approximations. The

70 second model takes both external and internal mixing of aerosol components into account. Also, it employs morphologically more realistic models for black carbon aerosols. Although black carbon contributes, on average, only some 5 % to the mass mixing ratio of particulate matter over Europe, it can have a significant global radiative warming effect. Previous theoretical studies on the optical properties of black carbon aerosols suggest that the use of homogeneous sphere models can intro-

75 duce substantial errors in the absorption cross section and single scattering albedo of such particles (e.g. Kahnert (2010a); Kahnert et al. (2013). The main goal of this study is to assess the impact of aerosol morphology and mixing state on radiometric quantities and radiative forcing rates simulated with a chemical transport model. To this end we compare the two optics models, and we gauge the significance of morphology by comparing the differences in the optics models to other sources of

80 error. As a gauge we use the impact of including or omitting aerosol dynamic processes; this provides us with a reference which is generally agreed to have a significant effect on aerosol transport models.

The CTM, its aerosol dynamics and mass transport modules, and the aerosol optics model are described in Sect. 2. There we also explain the methodology we employ for evaluation of the optics

85 model. In Sect. 3 we present and discuss computational results for selected cases and for several radiative and optical parameters. Concluding remarks are given in Sect. 4.

2 Model Description and Methods

2.1 General considerations and terminology

Aerosol particles typically originate from different emission sources, such as seasalt particles com-

90 ing from marine sources, wind-blown dust from dry land surfaces, volcanic ash from magmatic or phreatomagmatic eruptions, or black carbon produced during combustion of fossil fuel, biofuel, or biomass. During atmospheric transport particles from different sources can be mixed, resulting in heterogeneous aerosol populations consisting of particles of different morphologies, sizes, and

chemical composition. A mixture in which different chemical species are contained in separate particles is referred to as an *external mixture*. On the other hand, aerosol dynamic processes, such as nucleation, condensation, and coagulation, give rise to the formation and growth of secondary particles from precursor gases, as well as to the condensation of precursor gases onto existing primary particles. These processes result in particles in which several chemical species are mixed with each other in one and the same particle. Such a population is referred to as an *internal mixture*. There are two types of internal mixtures. If, e.g., hydrophillic liquid-phase components mix with each other, one can obtain a *homogeneous internal mixture* of different chemical species. On the other hand, condensation of gas-phase species onto non-soluble primary particles, or cloud processing of aerosols can result in liquid-phase material coating a solid core of, e.g, mineral dust or black carbon. We refer to the latter as an *inhomogeneous internal mixture*. Aerosol populations in nature are often both externally and internally mixed, i.e, they contain particles that are composed of a single chemical species as well as other particles that are composed of different chemical species, which can be homogeneously or inhomogeneously internally mixed.

Aerosol optical properties are strongly dependent on not only the size and chemical composition, but also on the mixing state, shape, and internal structure of particles. Therefore, before explaining the aerosol optics model, we first need to briefly describe the kind of information that can be provided by the aerosol transport model. In particular, we need to understand the level of detail with which the size distribution, size-dependent chemical composition, and the mixing state of the aerosols can be computed in a large-scale model.

2.2 Aerosol transport modelling with MATCH

As a regional model we employ the Multiple-scale Atmospheric Transport and CHemistry modelling system (MATCH) Andersson et al. (2007). The MATCH model allows us to choose between two aerosol model versions, a simpler mass transport model, and a more sophisticated aerosol dynamic transport model.

2.2.1 Mass transport model

A simple version, which we refer to as the "mass transport model", neglects all aerosol dynamic processes. It contains a photochemistry model that computes mass concentrations of secondary inorganic aerosols (SIA), which are formed from precursor gases. The SIA fraction consists of ammonium sulphate ($(NH_4)_2SO_4$), ammonium nitrate (NH_4NO_3), other particulate sulphates (PSO_x), and other particulate nitrates (PNO_x). The mass transport model further contains a seasalt module that computes NaCl emissions based on the parametrisations described in Mårtensson et al. (2003); Monahan et al. (1986). It also contains a simple wind-blown dust model and a module for transport of primary particulate matter (PPM), i.e., aerosols other than seasalt and windblown dust that are emitted as particles, rather than being formed from gas precursors. The size bins in the PPM model

4

Table 1. Size bins (characterised by the radius r) and chemical species in the MATCH mass transport model. The labels "p" and "s" refer to primary emitted particles and secondary particles generated from gas precursors.

size bin	r (nm)	OC	BC	wind blown	other PPM	NaCl	$(NH_4)_2SO_4$	NH_4NO_3	other PSO_x	other PNO_x
1	10–50	p	p		p	p	s	s	s	s
2	50–500	p	p		p	p	s	s	s	s
3	500–1250					p	s	s	s	s
4	1250–5000	p	p	p	p	p	s	s	s	s

are flexible. In the current model set-up the sea salt and PPM models were run for four size bins as shown in Table 1. We used EMEP PPM emission data for the year 2007, and, based on those and on Kupiainen and Klimont (2004, 2007), we generated gridded emission data for black carbon (BC), organic carbon (OC), and all other PPM. (Here, OC refers to the mass of all organic matter, not just the mass of carbon atoms in organic compounds.) The primary particle emissions are distributed among the four size classes; during atmospheric transport they remain chemically and dynamically inert in the model. Thus no chemical transformation, mixing processes with other compounds, or other size transformation processes are included in the model. The SIA components are given as total mass concentrations without any information about their size distribution. In the optics model a fixed size distribution is assumed to assign the total SIA mass to the four size bins. Water adsorption by particles is computed in the optics model as described in Sect. 2.3.1. More details on the MATCH photochemistry model can be found in Robertson et al. (1999); Andersson et al. (2007). The MATCH seasalt model is described in Foltescu et al. (2005).

2.2.2 Aerosol dynamics model

A more realistic description of particles can be achieved by accounting for aerosol dynamic processes. To this end the Sectional Aerosol module for Large Scale Applications (SALSA) (Kokkola et al., 2008) has recently been coupled to the MATCH photochemistry model (Andersson et al., 2015). The description of PNO_x, wind-blown dust, and secondary organic aerosols (SOA) is still under development in MATCH-SALSA. A simplified PNO_x description has been included in the model version employed here, while wind-blown dust and SOA are absent. The number and range of size bins is flexible in SALSA. Table 2 shows the current model set-up.

As is evident from the table, MATCH-SALSA accounts for both internally and externally mixed aerosols. For instance, size bins 12, 15, and 18 describe the same size range (350–873 nm), but different internal mixtures of various species. Similarly, bins 4 and 8 have the same size range (25-49 nm), but one describes an internal mixture, the other an external mixture of aerosol species.

Note that water is not directly calculated as a prognostic variable in MATCH-SALSA. Rather, it is a diagnostic variable computed in the MATCH-optics model as explained in Sect. 2.3.2. The table

5

Table 2. Size bins and chemical species in the MATCH-SALSA aerosol dynamic transport model. An "x" marks that the species is present in a particular size bin.

size bin	r (nm)	mixing state	OC	BC	other PPM	NaCl	PSO_x	PNO_x	PNH_x
1	1.5–3.8	internal	x				x		x
2	3.8–9.8	internal	x				x		x
3	9.8–25	internal	x				x		x
4	25–49	internal+H_2O	x	x	x	x	x		x
5	49–96	internal+H_2O	x	x	x	x	x		x
6	96–187	internal+H_2O	x	x	x	x	x		x
7	187–350	internal+H_2O	x	x	x	x	x		x
8	25–49	external	x	x			x		x
9	49–96	external	x	x			x		x
10	96–187	external	x	x			x		x
11	187–350	external	x	x	x		x		x
12	350–873	NaCl+H_2O				x			
13	873–2090	NaCl+H_2O				x			
14	2090–5000	NaCl+H_2O				x			
15	350–873	internal+H_2O	x	x	x		x	x	x
16	873–2090	internal+H_2O	x		x		x		x
17	2090–5000	internal+H_2O	x		x		x		x
18	350–873	internal+H_2O			x		x		x
19	873–2090	internal+H_2O			x		x		x
20	2090–5000	internal+H_2O			x		x		x

merely indicates which size bins are assumed in the optics model to be internally mixed with adsorbed water. A more detailed description of the MATCH-SALSA model can be found in Andersson et al. (2015).

2.3 Aerosol optics modelling

160 Aerosol optics models coupled to a CTM have to make consistent use of the information provided by the CTM, while invoking assumptions on optically relevant parameters that are not provided by the CTM. The parameters that influence the particles' optical properties are

- the aerosol size distribution;

- the refractive index of the materials of which the aerosols are composed;

165 - the morphology of the particles.

Morphology refers to both the overall shape of the particle, and, in case of inhomogeneously mixed particles, the variation of the refractive index inside the particle.

The information provided by the CTM depends on the level of detail in the process descriptions. In the MATCH mass transport model, we have size information for the primary particles, but only the total mass for secondary inorganic aerosols. Thus we have to invoke assumptions about the size distribution of these particles. The MATCH optics models in conjunction with the MATCH mass transport model assume that 10 % of the SIA aerosol mass are in the smallest size class (see Table 1), 60 % in the second, 20 % in the third, and 10 % in the fourth size class. Also, the mass transport model lacks any information about the mixing state of the particles. We therefore have to invoke appropriate assumptions on whether the aerosols are externally or internally mixed. Both the mass transport model and MATCH-SALSA lack information on whether the internally mixed particles are homogeneous or inhomogeneous. Also, neither model provides any information on the shape of the particles. The refractive index of the different chemical components in the aerosol phase and their spectral variation is given in Fig. 4 of Kahnert (2010a). That reference also contains detailed information about the different literature sources from which the refractive indices are taken.

2.3.1 Optics model for externally mixed aerosols

The simplest conceivable optics model assumes that all particles are homogeneous spheres, and that all chemical species are each in separate particles, i.e., externally mixed. As explained in Kahnert (2008), the external-mixture assumption results in a linear relation between the mass mixing ratios and the optical properties. Owing to the linearity, this model is particularly attractive for data assimilation applications (e.g. Benedetti et al. (2009)), which require linearised observation operators. However, this is also the crudest possible optics model, as it neglects both the effect of internal mixing and of particle morphology on optical properties.

The external-mixture model is implemented in the MATCH mass transport model, where it is primarily being used in the MATCH 3DVAR data assimilation system Kahnert (2008). Optical properties are pre-computed for twelve wavelength bands ranging from the UV-C to the mid-IR. Dust and black carbon are assumed to be hydrophobic, while sea salt, OC, and SIA components can each mix internally with water. The water volume fraction depends on temperature and humidity; it is computed by use of the parametrisation given in Gerber (1985). The aerosol/water mixture is assumed to be homogeneous. The dielectric properties of a homogeneous mixture of two or more components are described by a complex effective refractive index m_{eff}, which is usually computed by effective medium theory (EMT) (although chemical transport modellers often use simple volume mixing rules, most likely because EMTs are not commonly known in that field). We use Bruggemann's EMT (Bruggemann, 1935). Optical properties are pre-computed for eleven water volume fractions between 0 and 0.98; for intermediate volume fractions the optical properties are interpolated. The optical properties contained in the database are the extinction cross section C_{ext}, the scattering cross

7

section C_{sca}, the value of the phase function in the exact backscattering direction $p(180°)$, and the asymmetry parameter g.

As explained in Kahnert (2008), size-averaged optical properties are pre-computed by averaging over a log-normal size distribution $n_i(r) = N_i/(\sqrt{2\pi}r\ln\sigma_i)\exp[-\ln^2(r/r_i)/(2\ln^2\sigma_i)]$ for each size class i, where N_i represents the number density of particles in size bin i, r denotes the particle radius, $r_1 =$0.022 μm, $r_2 =$0.158 μm, $r_3 =$0.791 μm, $r_4 =$2.5 μm are the mean radii in each size mode, and the variances $\sigma_1 = \sigma_3 = \sigma_4 =$1.8, $\sigma_2 =$1.5 are based on measurements in Neusüß et al. (2002). The volume per size bin can be obtained by integrating $(4/3)\pi r^3 n_i(r)$ over the ith size bin interval; this can be used for converting mass mixing ratios into number densities in each size bin, which, in turn, allows us to compute radiative properties, such as aerosol optical depth (AOD), single-scattering albedo (SSA), asymmetry parameter g, and backscattering coefficient β_{bak} in each atmospheric grid cell in MATCH — see Kahnert (2008) for details.

2.3.2 Optics model for aerosols of different mixing states

The new MATCH-optics model accounts for both internally and externally mixed aerosols, and it contains both homogeneously and inhomogeneously mixed aerosols. Different shapes and morphologies are assumed for different types of particles.

1. Pure, externally mixed black carbon aerosols are assumed to have a fractal aggregate morphology as shown in Fig. 1. The fractal morphology can be described by the statistical scaling law $N_s = k_0(R_g/a)^{D_f}$, where N_s denotes the number of spherical monomers in the aggregate, D_f and k_0 are the fractal dimension and fractal prefactor, a is the monomer radius, and $R_g = \sqrt{\sum_{n=1}^{N_s} r_n^2/N_s}$ is the radius of gyration, where r_n describes the distance of the nth monomer from the aggregate's centre of mass. We use $D_f =$1.8, $k_0 =$1.3, which is based on the review in Bond and Bergstrom (2006). Although in the atmosphere black carbon aggregates may also have higher fractal dimensions (e.g. Adachi et al. (2007)), assuming a lower fractal dimension around 1.8 yields mass absorption cross sections that lie closer to experimental data, as was shown in Kahnert and Devasthale (2011). The monomer radius was assumed to be $a = 25$ nm. This is consistent with field observations (Adachi and Buseck, 2008); also, it was shown (Kahnert, 2010b) that this choice of monomer radius in light scattering computations yields results for the single-scattering albedo of black carbon aggregates consistent with observations

The calculation in Kahnert and Devasthale (2011) were limited to aggregates up to $N_s =$600. In order to cover the size range of externally mixed black carbon in SALSA we had to extend these calculations to aggregate sizes up to $N_s =$2744, which corresponds to a volume-equivalent radius of $R_V =$350 nm (compare with Table 2). We used the multiple-sphere T-matrix code (Mackowski and Mishchenko, 2011), which is based on the numerically exact superposition T-matrix method for solving Maxwell's equations. Figure 2 shows some of the
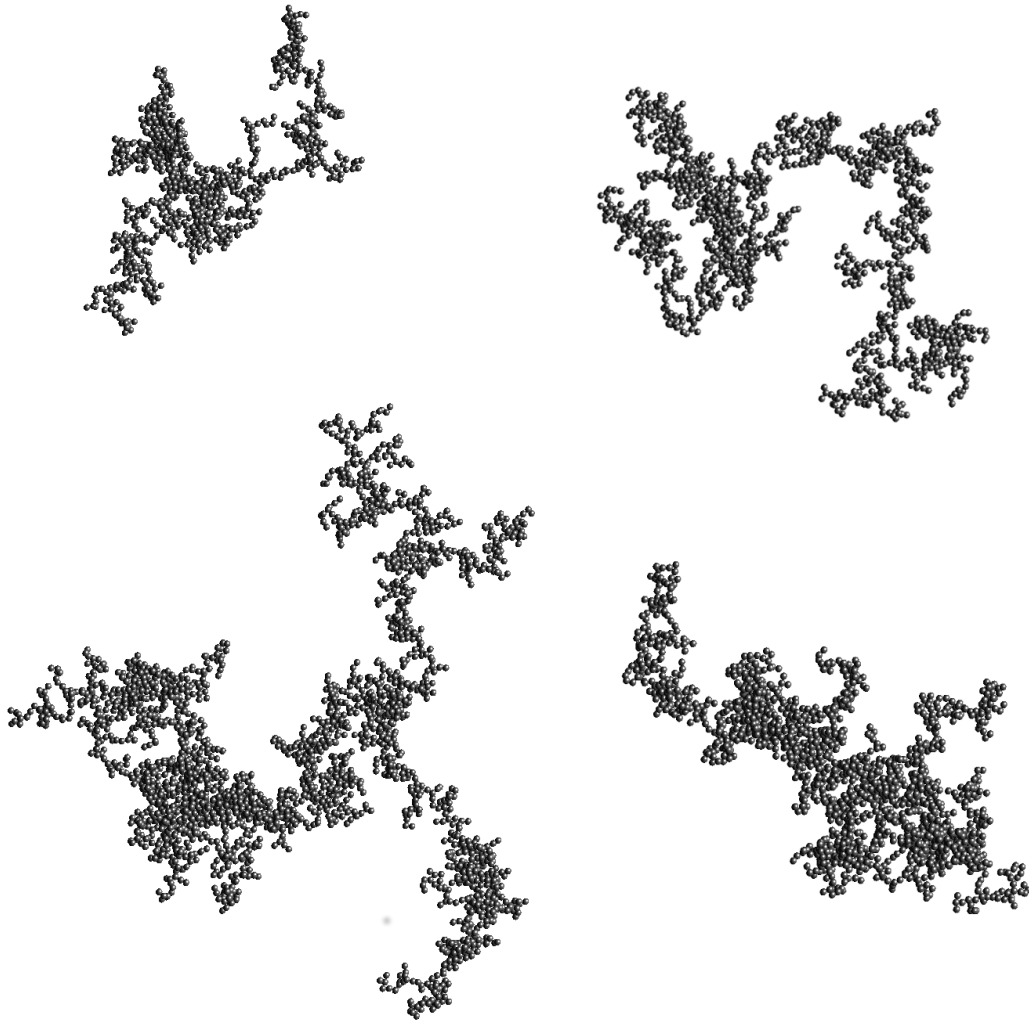
8

Figure 1. Examples of fractal aggregate model particles for computing optical properties of externally mixed black carbon. The aggregates consist of 1000, 1500, 2000, and 2744 monomers (in clockwise order, starting from upper left).
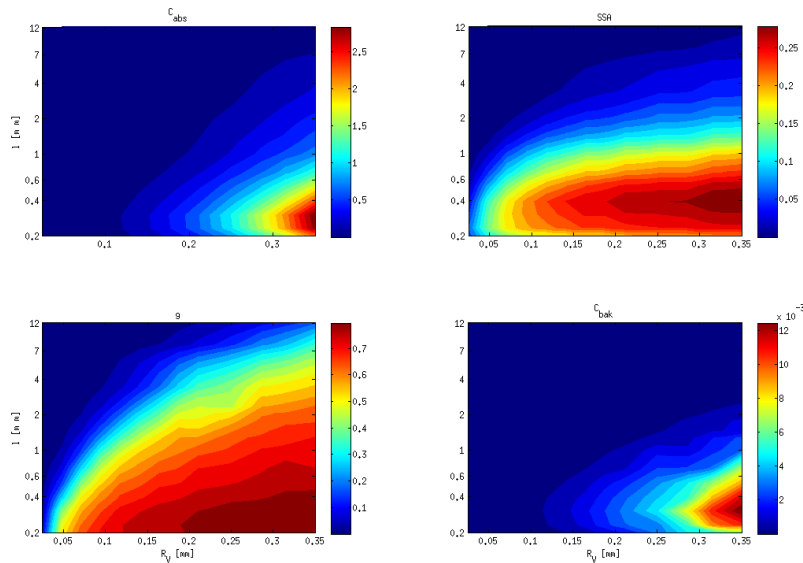
Figure 2. Absorption cross section C_{abs} (upper left), single-scattering albedo SSA (upper right), asymmetry parameter g (bottom left), and backscattering cross section C_{bak} (bottom right) of black carbon aggregates as a function of volume-equivalent radius R_V and wavelength λ.

computed black carbon optical properties as a function of particle size and wavelength. All optical properties are averaged over particle orientations. The absorption cross section C_{abs} shows the characteristic decline $\sim 1/\lambda$ at long wavelengths, where the refractive index of black carbon is changing only slowly (Chang and Charalampopoulos, 1990). Also, C_{abs} increases with particle size. For small particle sizes this increase goes as $\sim R_V^3$, which is typical for the Rayleigh scattering regime (Mishchenko et al., 2002).

2. Black carbon aerosols that are internally mixed with other aerosol components are morphologically very complex. It is technically beyond the reach of our present capabilities to build an aerosol optics database with the use of morphologically realistic model particles. However, it is possible to employ realistic model particles in reference computations for some selected cases. This has recently been done in Kahnert et al. (2013). In that study, optical properties of encapsulated aggregate model particles, such as the one shown in Fig. 3 (left), were computed in the size range from 100–500 nm, for different black carbon volume fractions, and for wavelengths from the UV-C to the mid-IR. The morphological parameters characterising these model particles were based on field observations (Adachi and Buseck, 2008); the coating material was sulphate. The computations were performed with the discrete dipole approximation (Yurkin and Hoekstra, 2007).
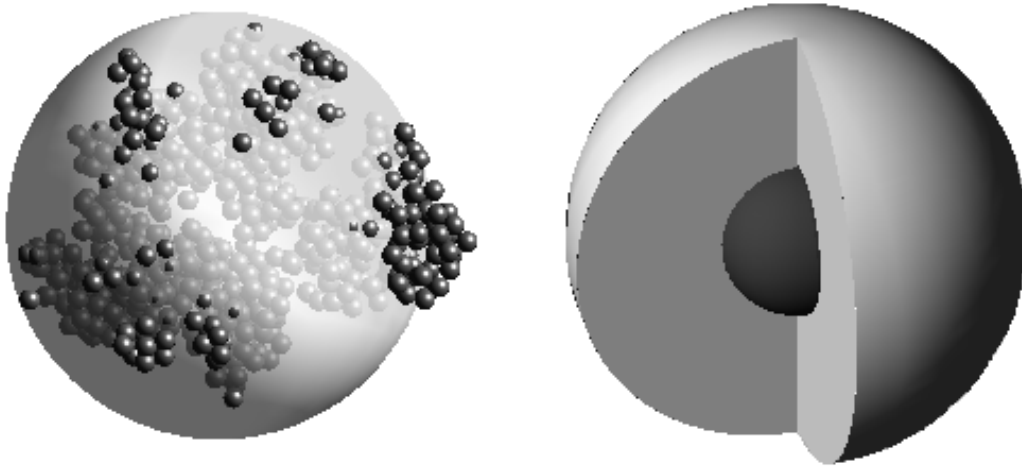
10

Figure 3. Morphologically realistic encapsulated aggregate model for internally mixed black carbon (left), and core-grey-shell model (right).

In Kahnert et al. (2013) the computational results were compared to those obtained with simple model particles, such as externally mixed homogeneous spheres, internally mixed homogeneous spheres, and concentric core-shell particles with a carbon core and a sulphate shell. The analysis revealed which morphological properties of the encapsulated aggregate particles had the dominant impact on the optical properties. There are two important properties: (1) The amount of carbon mass that interacts with the electromagnetic field has a major impact on the absorption cross section C_{abs}. In a core-shell model as well as in a model based on externally mixed homogeneous spheres, all of the black carbon is concentrated in a single sphere. Owing to absorption the electromagnetic field does not penetrate deeply into this sphere. Hence much of the carbon mass is shielded from interacting with the field, resulting in an underestimation of C_{abs} compared to the encapsulated aggregates, in which a much larger fraction of the carbon mass can contribute to the absorption of electromagnetic energy. By contrast, in a homogeneous internal mixture model the black carbon is distributed evenly throughout the sulphate host, which allows too much of the carbon mass to interact with the field. This results in an overestimation of C_{abs}. (2) Compared to a bare black carbon aggregate, a coated aggregate has a larger geometric cross section. Hence more light is intercepted by an internally mixed particle and focused onto the black carbon inclusion, thus enhancing C_{abs}. This effect is neglected in the external mixture model, resulting in an underestimation of C_{abs}.

Once we understand which morphological properties are most essential, and which ones make a minor contribution to the optical properties, we can devise model particles that account for the most important morphological effects, yet are sufficiently simple for computing a look-up table for large-scale modelling. It was proposed in Kahnert et al. (2013) to use a core-shell

model (hence accounting for the coating effect) in which only part of the carbon mass is contained in the core, and the remaining part is homogeneously mixed with the shell. The model particle is illustrated in Fig. 3 (right). The core-shell partitioning of the carbon mass is a free parameter, with which one can interpolate between the two extreme models of the homogeneous mixture (all carbon mass mixed with the shell) and the regular core-shell model (all carbon mass in the core). This model has been referred to as the concentric core-grey-shell (CGS) model. The tuning of the free parameter in the model was done to fit the reference model of encapsulated aggregates as described in Kahnert et al. (2013). The CGS model has been employed in generating the new MATCH-optics look-up table. The shell material can be any mixture of water-soluble components. In the mass transport model, we assume that all SIA components and all sea salt is internally mixed. We further assume that in size classes 1–4, 0, 70, 70, and 100 %, respectively, of the black carbon, 0, 70, 70, and 70 % of the organic carbon, and 0, 1.3, 1.3, and 1.3 % of the dust are internally mixed; the remaining BC, OC, and dust mass is externally mixed. In SALSA, the mixing state depends on the size bin (see Table 2), and the mixing proportions are provided by the model results. In both the mass transport model and in MATCH-SALSA, the contribution to the effective refractive index of dust and black carbon is computed by the Maxwell-Garnett EMT Maxwell Garnett (1904), while for all other components we use the Bruggemann EMT (Bruggemann, 1935).

3. All other externally mixed particles not containing black carbon are assumed to be homogeneous spheres in the present version of the look-up table.

The look-up tables contain results for C_{ext}, C_{sca}, g, and C_{bak} in 28 wavelength bands from the UV-C to the mid-IR. Computations with the CGS model were performed for 37 discrete BC volume fractions. For the shell material, as well as for non-carbon containing particles, the table contains (depending on the wavelength band) up to 40 discrete values of the real part and up to 18 discrete values of the imaginary part of the refractive index. The range of the refractive indices varies with wavelength; it is determined by those chemical components that, at each given wavelength, have the most extreme values of the refractive index. The optical properties are pre-averaged over particle sizes for each size bin. Thus we generated one look-up table each for the mass transport model with its four size bins, and for SALSA with its 20 size bins. It is assumed that the number density is constant in each size bin.

The MATCH-optics model computes in each grid cell and for each size bin the effective refractive index of the internally mixed material by use of EMT. The corresponding optical properties are obtained by interpolating the closest pre-computed results in the look-up table. Size-averaging is performed by weighing the optical cross sections as well as $g \cdot C_{\text{sca}}$ in each size bin with the number density per bin and adding over all bins. The integrated quantities are then divided by the total particle number density; the integral over $g \cdot C_{\text{sca}}$ is also divided by the size-averaged scattering cross section.

12

2.4 Evaluation of the optics models

315 The new internal-mixture optics model with its BC fractal aggregate and core-grey-shell model parti-
cles accounts for significant morphological details in aerosols. The main question we want to address
is whether or not this high level of detail is really necessary, i.e., if it has any *significant* impact on
optical properties modelled with a CTM. By *significant* we mean an impact that is comparable to
other effects whose importance is well understood. Thus to make such an assessment we need to

320 pick a well-understood effect that can serve as a gauge, i.e., to which we can compare the impact of
particle morphology on optical properties. We take the effect of aerosol dynamics as a gauge. Thus
we compute aerosol optical properties

1. with the MATCH mass-transport model (i.e., with aerosol dynamics switched off), in conjunc-
   tion with the old optics model (abbreviated by MT-EXT, "mass-transport external mixture");

325 2. with the MATCH mass-transport model in conjunction with the new optics model (MT-CGS,
   "mass-transport core-grey-shell");

3. with the MATCH-SALSA model (i.e., with aerosol dynamics switched on), in conjunction
   with the new optics model (SALSA-CGS, "MATCH-SALSA core-grey-shell").

Comparison of 1. and 2. will allow us to assess the impact of the morphological assumptions in the

330 aerosol optics model. Comparison of 2. and 3. will give us an estimate of how much the inclusion or
omission of aerosol dynamic processes impacts modelling results of aerosol radiometric properties.
As aerosol dynamics is well-known to have a substantial impact on aerosol concentrations and size
distributions, this effect will provide us with a reference to which we can compare the impact of the
morphological assumptions made in the aerosol optics model.

335 As an example, Fig. 2.4 shows the extinction aerosol optical depth (AOD) over the European
model domain computed on December 22 2007 at 12:00 UTC with MT-EXT (left), MT-CGS (cen-
tre), and SALSA-CGS (right). The general spatial patterns are similar, as they should, since all three
runs used the same EMEP emissions and HIRLAM meteorological data. However, the magnitude
of the AOD results can differ significantly among the three model runs (note the semi-logarithmic

340 scale!). Interestingly, differences between the two optics models (left and centre) are roughly on the
same order as those between the mass-transport and aerosol dynamic models (centre and right).

Thus a first inspection of computed fields of aerosol optical properties suggests that the level
of detail in the morphological assumptions of the aerosol optics model may be significant for the
modelling results. In a next step we quantify differences in modelled aerosol radiative forcing among

345 the three model versions. To this end we pick four geographic locations that are indicated by circles
in Fig. 2.4; (i) one site over Northern Italy (45.0° N, 8.5° E), one over the Mediterranean Sea (37.5°
N, 5.5° E), one over Poland (52.6° N, 21.0° E), and one over the North Sea (52.0° N, 2.7° E). We
further pick two instances representing low-BC summer and high-BC winter conditions, namely,
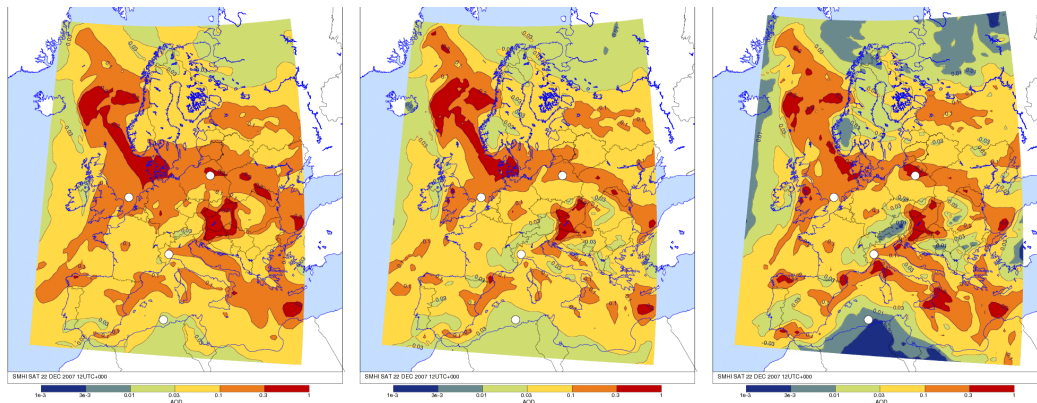
13

Figure 4. Aerosol optical depth over Euope on December 22 2007, 12:00 UTC (noon). Results are shown for the mass transport model in conjunction with the old external-mixture optics model (left), and with the new internal-mixture/core-grey-shell/fractal BC aggregate model (center), as well as for the MATCH-SALSA model in conjunction with the new optics model (right). The circles indicate the four locations used for radiative transfer studies. Note the semi-logarithmic colour scale!

22 June 2007 12:00 UTC, and 22 December 2007 12:00 UTC. Radiative transfer calculations are
350   performed for each of these four sites and for both instances. Vertical profiles of the aerosol optical depth per layer, the single-scattering albedo, and the asymmetry parameter are used as input to the libRadtran radiative transfer package (Kylling et al., 1998), assuming a plane-parallel atmosphere. For the surface albedo of the ocean we assume a spectrally constant value of 0.065, while for the spectrally varying surface albedo of the two land locations we used MODIS observations for each of
355   the two instances. The results were spectrally integrated to obtain the broadband radiative fluxes. The radiative transfer simulations were repeated for corresponding profiles of optical properties in the absence of black carbon, as well as for clear-sky conditions. This allows us to compute differences in broadband radiative fluxes, i.e., the radiative effect of black carbon, and the radiative effect of all aerosols. The results of this radiative transfer study are discussed in Sect. 3.1.
360   To further investigate the significance of the optics model on radiometric properties, we look at re- mote sensing-related optical properties, namely, backscattering coefficient and Ångström exponent. These results are discussed in Sect. 3.3 and 3.4, respectively.

3   Results

3.1   Optical properties and radiative forcing

365   The result for the optical properties obtained with the three model versions (AOD per layer, SSA and g) at the wavelength 532(CGS)/500(EXT) nm, together with the radiative forcing for aerosols and black carbon can be seen in Figs. 5 – 8 for Northern Italy and the Mediterranean on June 22

14

2007. Each figure shows the differences in direct solar flux ΔF_s (top left), diffuse downwelling flux ΔF_d (top right), diffuse upwelling flux ΔF_u (centre left), and net radiative flux $\Delta F_{net} = \Delta F_s + \Delta F_d - \Delta F_u$ (centre right), where either the difference between aerosol-laden and clear sky conditions are considered (Figs. 5–6), or the difference between fluxes in the presence and absence of black carbon (7–8). Top-of-atmosphere (TOA) results for the other geographical locations are summarized in terms of aerosol forcing in table 3 and black carbon forcing in table 4. The wavelengths 532(CGS)/500(EXT) nm are near the maximum of the solar spectrum. At other wavelengths (not shown) the optical properties behave similarly. Each figure has a vertical span of 6 km, which comprises that part of the troposphere where almost all aerosols are concentrated in the cases we picked.

Before starting our analysis, we note that the magnitude of the radiative fluxes generally depends on the concentration of aerosols. As we cannot claim that the test cases we happened to pick are in any way representative for *typical* aerosol and black carbon loads, we are not focusing on the *magnitude* of the radiative fluxes here. Rather, we want to compare the *differences* in radiative fluxes among the three model versions.

3.1.1   Comparison of aersol dynamics and mass-transport model

We start by comparing radiative fluxes in the presence and absence of aerosols, which we refer to as the "aerosol radiative effects". Figures 5 and 6 show the aerosol radiative effects modelled over Northern Italy and over the Mediterranean north of Algier, respectively. The general patterns in both plots can be understood as follows. In the presence of aerosols, optical extinction is stronger than in clean air. Thus the presence of aerosols gives a reduction ΔF_s of the direct solar flux (upper left). As the aerosol optical depth per atmospheric layer strongly increases near the ground, the magnitude of ΔF_s increases with decreasing altitude. Further, aerosol extinction results in the generation of diffuse flux; the downwelling diffuse flux accumulates downward, resulting in an increasing excess of downwelling flux ΔF_d in the presence of aerosols as one approaches the surface. The upwelling flux F_u is generated by scattering in the atmosphere and reflection at the surface. Since aerosol extinction reduces the total flux as one approaches the surface, less upwelling diffuse flux is generated at low altitudes; hence the difference in upwelling flux ΔF_u between an aerosol-laden and a clear sky atmosphere is negative near the surface. However, it increases with altitude, because at higher altitudes the difference (aerosol - clear sky) in the total flux that can be converted into upwelling diffuse flux decreases at higher altitudes.

If we focus now on differences in the radiative net flux ΔF_{net} at high altitudes, i.e., the radiative forcing effect of aerosols, then we see significant differences between the mass transport model (MT, red) and SALSA (green) at both geographic locations. It is evident that the main cause for these are corresponding differences in the diffuse upwelling flux ΔF_u.

15

At both locations the diffuse upwelling flux is smaller for SALSA then for MT, but for different reasons. Over the Mediterranean (Fig. 6), the AOD is significantly smaller for SALSA than for MT, resulting in less extinction of the direct flux, hence less generation of diffuse flux, and a smaller radiative cooling effect for SALSA.

Over Northern Italy (Fig. 5), there is almost no difference in AOD between the two models. It can be seen from the AOD profile that the majority of aerosols reside in the lowest 1 km near the surface. However, above 1 km the results of ΔF_u obtained with SALSA and MT diverge with increasing altitude. This is a result of the reflection by the near-surface aerosol layer, which is slightly different in the two models. In MT the SSA is higher than in SALSA, resulting in more scattering, thus in more diffuse radiation. The asymmetry parameter is slightly larger in MT than in SALSA; correspondingly, the partitioning in MT between downwelling and upwelling radiation is somewhat shifted in favour of the former. However, this only partially counteracts the generation of a higher amount of diffuse upwelling radiation in MT due to the higher SSA. The net effect is a higher value of ΔF_u in MT, hence a larger radiative cooling effect at higher altitudes.

To further analyse the difference in optical properties between MT and SALSA, we look at the aerosol masses and the relative sizes of the particles. Figure 9 shows vertical profiles of the effective radius of the size distributions in SALSA (green) and the MT model (black) over Northern Italy (left) and over the Mediterranean (right). Figure 10 shows profiles for the total aerosol mass (1st row), BC (black carbon) (2nd row), sulphate (3rd row), and nitrate (4th row) for both Northern Italy (1st column) and Mediterranean (2nd column). We focus on the total aerosol mass, which is expected to impact the aerosol optical depth. The aerosol optical depth is dependent on the number density (which, in turn, increases with the mass mixing ratio), as well as on the extinction cross section (which generally increases with the effective radius of the particles). Over Northern Italy, the SALSA model predicts a larger mass mixing ratio than the MT model (Fig. 10, upper left), but also a smaller particle size (Fig. 9, left). These two effects cancel almost exactly, resulting in nearly identical aerosol optical depths predicted with the two models (Fig. 5, bottom left). By contrast, over the Mediterranean the two models predict similar mass mixing ratios (Fig. 10, upper right), while SALSA predicts a much lower effective radius than the MT model (Fig. 9, right). As a consequence, the optical depth is significantly lower in SALSA than in MT (Fig. 6, bottom left). The SSA is lower in SALSA than in MT. This is mainly caused by the fact that the effective radius is smaller in SALSA than in MT, since SSA is usually increasing with size.

The radiative impacts summarised in table 3 show the same behaviour as Fig. 5 and 6 at three of the four geographical locations. The Polish site deviates, since SALSA produces a much larger radiative cooling than the MT model. This can be explained by SALSA having a larger amount of aerosols throughout the column at that site, especially more sulphate, which, when externally mixed, contributes to a larger amount of scattering and therefore a higher SSA and a larger diffuse upwelling radiative flux.

16

440   We now compare radiative fluxes in the presence and absence of black carbon, which we refer
to as the "black carbon radiative effect". Figure 7 and 8 show the radiative effect of black carbon
together with the optical properties with and without black carbon. Again, the dominant feature of
ΔF_{net} at TOA comes from corresponding differences in the upwelling diffuse radiative flux ΔF_u.
In these figures, we have to focus on the difference in the optical properties when analysing the
445   radiative fluxes. The general pattern can be seen in Fig. 7, which shows the differences in radiative
fluxes and in the optical properties over Northern Italy. The direct solar flux (upper left) decreases
with decreasing altitude owing to extinction. The magnitude of the decrease mainly reflects the
differences in optical depth in the presence and absence of black carbon (bottom left), which is
slightly larger in SALSA than in MT. The decrease in solar flux does not automatically result in
450   an increase in the downwelling diffuse flux with decreasing altitude (upper right), as it was in the
comparison of fluxes in the presence and absence of *all* aerosols. The situation is more complex
now. Near the surface, where the optical depth is largest, the difference in SSA in the presence
and absence of black carbon is quite large in the MT model (bottom centre, red lines), and slightly
smaller in SALSA (green lines). As a result, absorption contributes more to the total extinction in
455   the MT model than in SALSA (at least near the surface). Hence, the portion of the downwelling
flux that is absorbed on its way downward is larger in the MT model than in SALSA, resulting
in a decrease of the diffuse downwelling flux with decreasing altitude (upper right, red line). The
differences between the two models in the diffuse upwelling flux are very small (centre left, red and
green lines). This is the result of cancelling effects; for instance, there is less direct solar flux, but
460   more diffuse downwelling flux in SALSA that can be converted into diffuse upwelling flux through
scattering. As a result, the differences between both models in the net flux (centre right, red and
green lines) are almost negligible.

    Figure 8 shows the radiative effect of black carbon over the Mediterranean. Again, the dominant
feature of ΔF_{net} at TOA comes from corresponding differences in the upwelling diffuse radiative
465   flux ΔF_u. The difference between MT and SALSA are not as prominent here, mainly due to the
fact that the differences in the optical properties are similar, especially in the SSA. There is still a
small difference for the Mediterranean, where SALSA has a larger radiative cooling than MT. This
difference is very small, but it may come from the slight difference in the AOD combined with the
difference in SSA from above 1 km, where SALSA has a marginally larger difference than MT,
470   creating the difference in the net radiative flux above 1 km. Another possibility is that these small
differences are caused by multiple scattering effects, which are notoriously difficult to understand by
an intuitive approach. If studying the differences in AOD and SSA for the twelve wavelengths used
in this study (not shown), the differences for SALSA AOD and SSA are smaller for the long-wave
(LW) part of the spectrum (533.2-3461.5 nm). This results in less LW extinction and scattering and
475   slightly more radiative cooling for SALSA.

17

Table 4 shows the black carbon forcing for all the four geographical locations and both months. In June the difference at the TOA is very small between MT and SALSA for all the locations, but larger for the Mediterranean as noted in Fig. 8. The month of December shows a pattern where SALSA has a higher radiative heating over land, and smaller over the ocean compared to MT. This is strongly coupled to the larger difference in BC amounts over land than over the oceans, where the two models have similar values all through the column, see Fig. 10 for Northern Italy and Mediterranean. Poland and North Sea are not shown here, but show similar behaviour.

3.1.2 Comparison of the two optics models

The comparison between SALSA and the MT model in the previous section served two purposes. First, it helped us to develop a basic understanding for the effects of aerosols and black carbon on radiative fluxes. Second, it provided us with a gauge for assessing the importance of the aerosol optics model, which will be the subject of this section.

We compare the old EXT (blue line) and the new CGS (red line) optics models in Figs. 5 and 6, each used in conjunction with the MT-version of MATCH. The net radiative flux ΔF_{net} in the CGS model shows a weaker TOA cooling effect than the EXT model, both over Northern Italy and over the Mediterranean. Again, the upwelling flux has the dominant impact on the behaviour of the TOA net radiative flux. Over Northern Italy (Fig. 5) the diffuse upwelling flux is larger for the EXT model above 1 km, whereas it is smaller below 1km and at the bottom of the atmosphere (BOA). The AOD profile reveals that in the EXT model extinction is stronger than in the CGS model throughout the tropospheric column. As a result, there is more diffuse downwelling flux being generated in EXT than in CGS. At the bottom of the atmosphere (BOA) extinction of the direct flux is stronger than generation of diffuse downwelling flux; hence less downwelling flux is reflected by the surface, resulting in less BOA upwelling diffuse flux in EXT than in CGS. Higher up in the troposphere, the upwelling diffuse flux is mostly generated by atmospheric scattering rather than reflection from the surface. As the SSA in EXT is higher than in CGS, more diffuse flux is generated, resulting in a stronger radiative cooling effect in EXT than in CGS.

Over the Mediterranean (Fig. 6), the EXT and CGS model have almost identical AOD profiles in the green part of the spectrum. However, at longer wavelengths (not shown) EXT predicts substantially higher AOD values than CGS. This explains the larger amount of diffuse broadband radiation generated in the EXT model, which results in a stronger negative TOA net flux in EXT as compared to the CGS model. Note that the differences in SSA between EXT and CGS are fairly small, while the differences in g are rather large. The higher values of g in EXT may contribute to the large amount of diffuse downdwelling radiation in that model; however, the dominant effect is likely to be the high optical depth at red and IR wavelengths.

Table 3 summarises the TOA net radiative flux at all four geographical locations for both June and December. The largest differences among the models are seen in December at the two northernmost
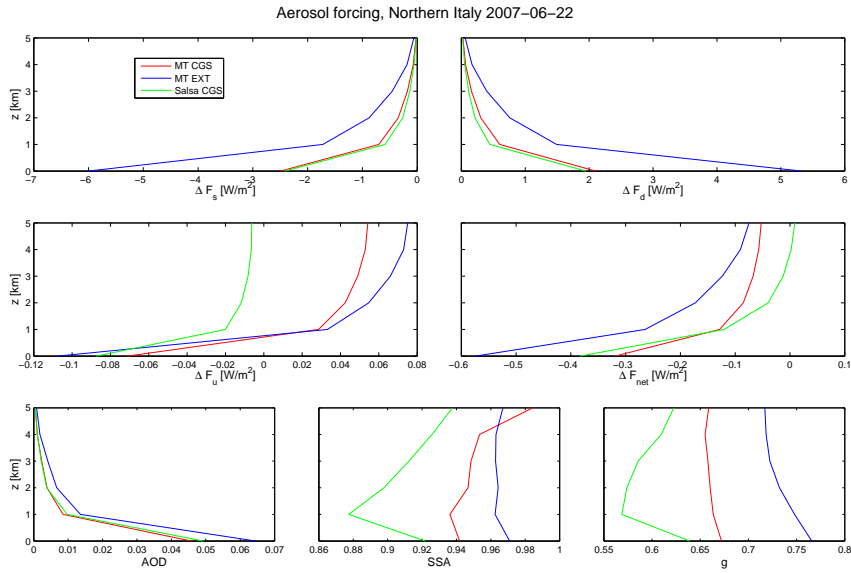
18

Figure 5. Aerosol forcing and optical properties at 532(CGS)/500(EXT) nm for Northern Italy in June.

locations, i.e., Poland and the North Sea. At these two places, the total aerosol amount (not shown) is significantly higher than at the other two locations farther south, giving rise to a larger absolute changes in the aerosol forcing.

515   The black carbon forcing looks rather different at the two geographical locations. Over Northern Italy, the black carbon forcing is more significant due to higher levels of BC, see Fig. 10. As can be seen in Fig. 7, the differences in optical properties computed with and without black carbon are larger in the CGS model than in the EXT model, particularly for the SSA. This means that in the CGS model the presence of black carbon causes more absorption than in the EXT model, thus generating

520   less diffuse down- and updwelling flux by scattering. As a result, the CGS model predicts more radiative warming, i.e., a higher TOA radiative net flux than the EXT model. The reason for this is that (i) the CGS model treats externally mixed soot as aggregates, which have a lower SSA than the massive black carbon spheres in the EXT model; and (ii) the CGS model treats internally mixed soot as a coated core-grey-shell model, which accounts for focusing of electromagnetic radiation onto

525   the carbon core, thus enhancing absorption, i.e., lowering the SSA, while the EXT model treats *all* black carbon as externally mixed.
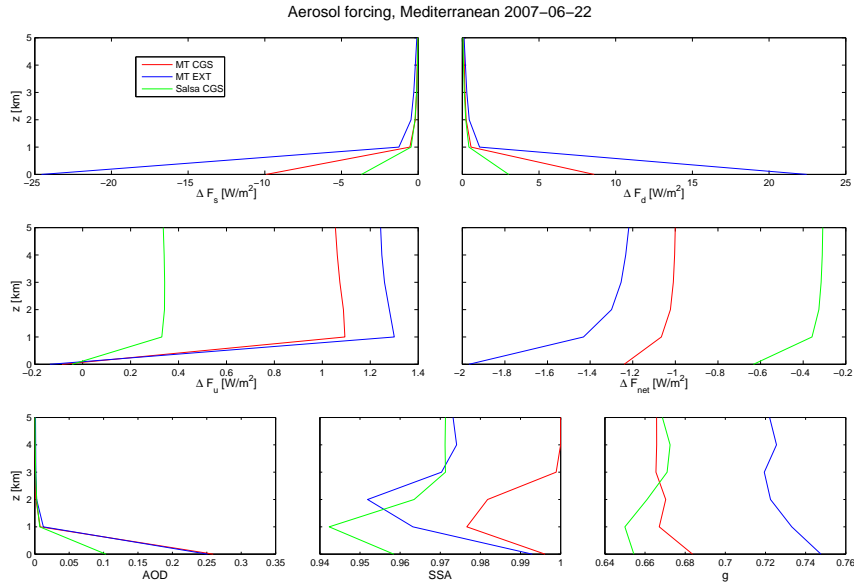
19

Figure 6. Aerosol forcing and optical properties at 532(CGS)/500(EXT) nm for the Mediterranean in June.

Table 3. The aerosol forcing at the top of the atmosphere (TOA), $\Delta F_{net,TOA}$ [W/m^2], for the four different geographical locations, one summer and one winter event, and three model versions.

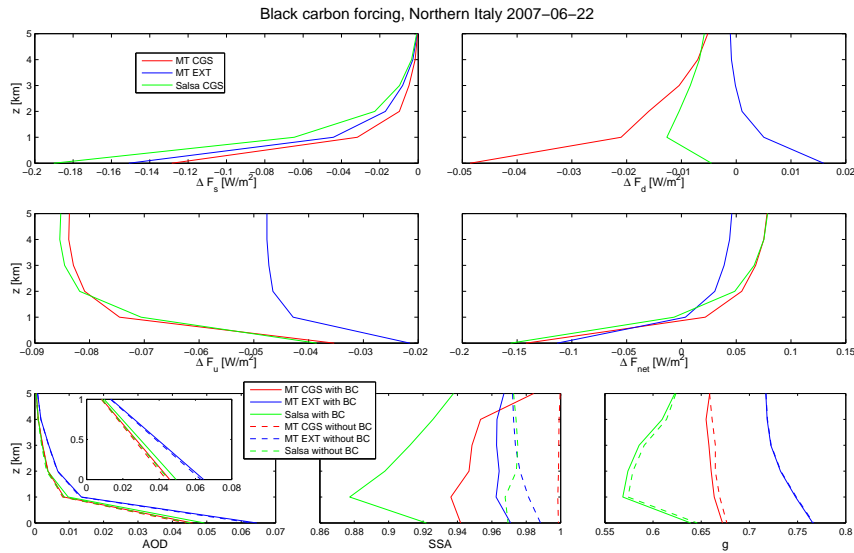|		MT-EXT	MT-CGS	SALSA-CGS
	Poland	-0.21	-0.21	-0.77
	North Sea	-0.34	-0.29	-0.24
Summer	Northern Italy	-0.06	-0.05	0.01
	Mediterranean	-1.20	-0.99	-0.30
	Polen	-4.41	-2.00	-2.18
	North Sea	-2.85	-1.21	-0.86
Winter	Northern Italy	-1.15	-0.53	-0.57
	Mediterranean	-0.09	-0.04	-0.03

Figure 7. Black carbon forcing and optical properties at 532(CGS)/500(EXT) nm for Northern Italy in June.

Table 4. The black carbon forcing at the top of the atmosphere (TOA), $\Delta F_{net,TOA}$ [W/m^2], for the four different geographical locations, one summer and one winter event, and three model versions.

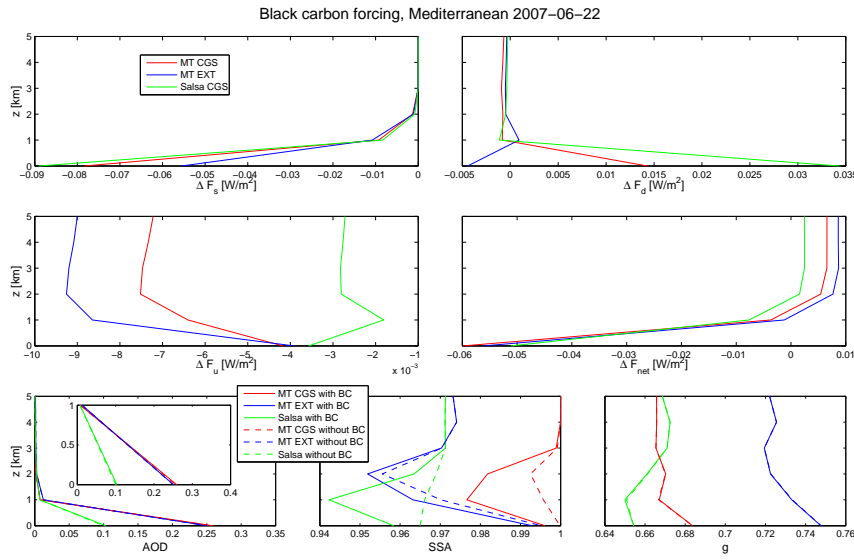|		MT-EXT	MT-CGS	SALSA-CGS
	Poland	1.02e-02	1.16e-02	1.20e-02
	North Sea	1.71e-02	1.54e-02	1.49e-02
Summer	Northern Italy	4.61e-02	7.77e-02	7.86e-02
	Mediterranean	8.54e-03	6.45e-03	2.41e-03
	Poland	4.03e-02	3.56e-02	6.83e-02
	North Sea	1.95e-02	2.28e-02	4.97e-03
Winter	Northern Italy	6.73e-02	1.08e-01	1.46e-01
	Mediterranean	6.03e-04	1.34e-03	3.13e-04

Figure 8. Black carbon forcing and optical properties at 532(CGS)/500(EXT) nm for the Mediterranean in June.
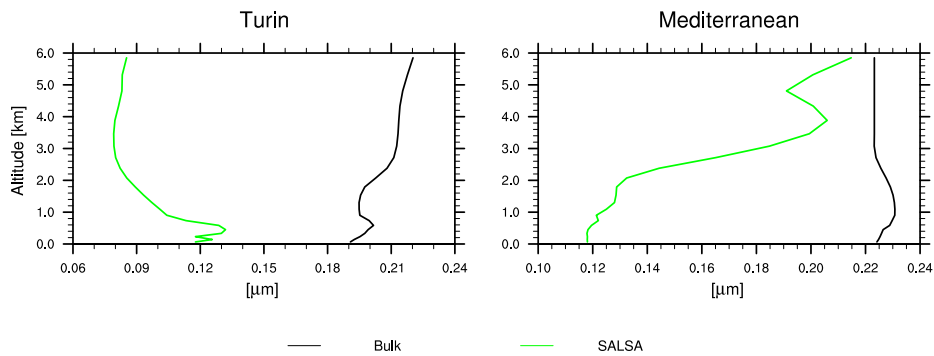

Figure 9. Effective radius for the two chemical transport model versions MT and SALSA over Northern Italy and Mediterranean in June.
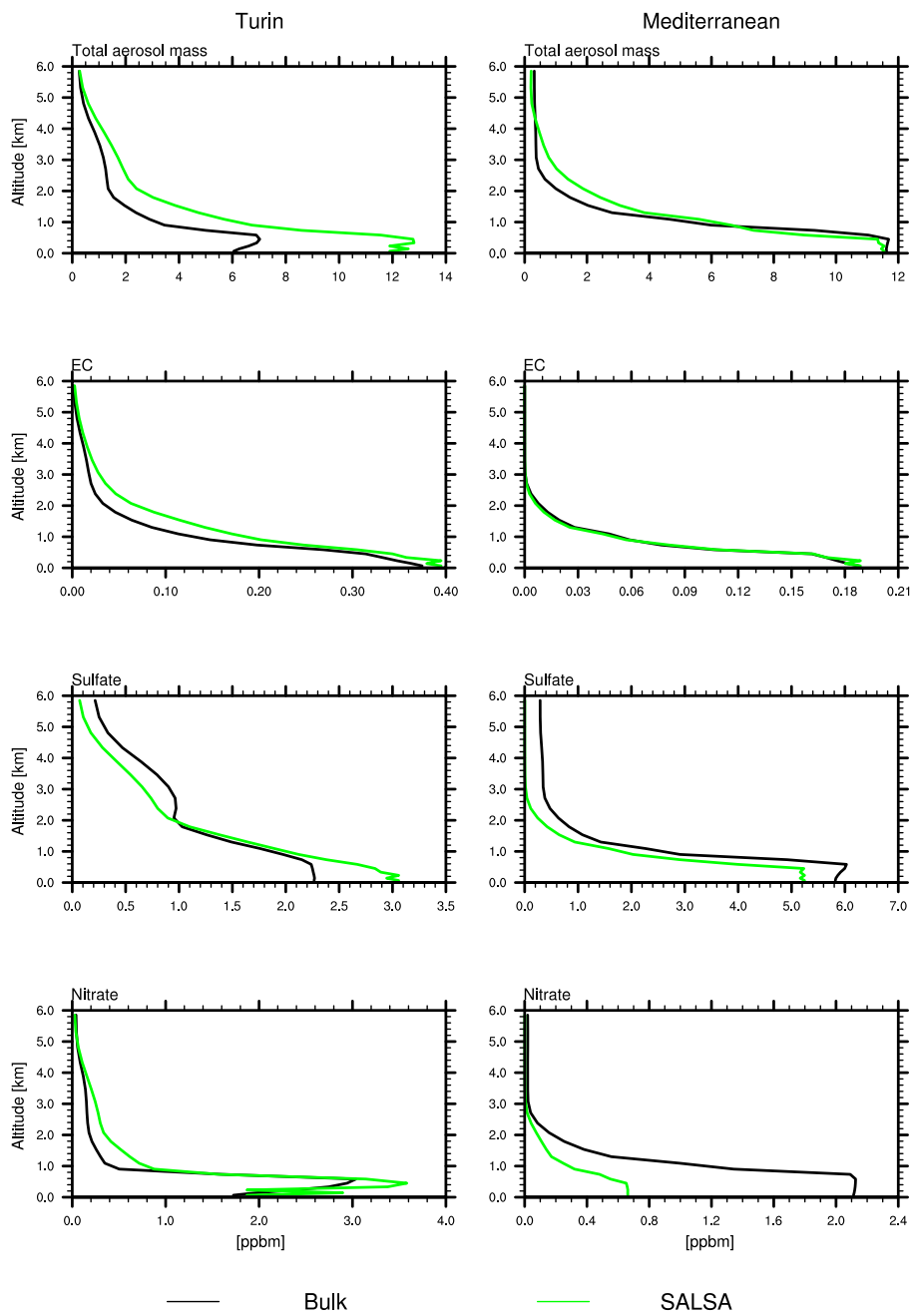
Figure 10. Vertical distribution of aerosols at Northern Italy and Mediterranean in June.

3.2 Gauging the significance of aerosol optics modelling

Now that we have understood the impact of the aerosol optical properties on radiative fluxes, we finally turn to the main question of this study. We ask if the level of detail in aerosol optics modelling has a significant impact on observable radiometric properties. As a gauge we consider the changes in radiometric properties caused by the inclusion or omission of aerosol dynamic processes. Thus we compare in Figs. 5–8 the differences in radiative forcing between the red and green lines to the corresponding differences in the red and blue lines. We see that in some cases the choice of optics model has a stronger effect than the inclusion of aerosol dynamics (e.g. 7), while in other cases it is the other way round (e.g. 6). We can also inspect Tables 3 and 4 and arrive at the same result. On average, the effect of including aerosol dynamics on the TOA radiative forcing is of comparable magnitude as the effect caused by employing a more realistic aerosol optics model. In the following two subsections, we will discuss the significance of the optics model for radiometric quantities that are relevant for remote sensing applications.

3.3 Backscattering coefficient

From ground-based and space-borne lidars measurements one can obtain the aerosol backscattering coefficient β, which is proportional to the backscattering cross section C_{bak} of the particles and the aerosol number density. Figure 11 shows vertical profiles of β computed at two locations and at two instances, as indicated in the figure headings. Each panel shows computational results obtained with the three different model versions. The figure shows results for the second Nd:YAG harmonic of 532 nm. Corresponding results computed for wavelengths of 355 and 1064 nm lead to similar conclusions.

We saw in Fig. 10 for June over Northern Italy (upper left) that SALSA predicts an aerosol mass mixing ratio, hence a particle number density, that is higher than that in the MT model. But we also saw in Fig. 9 (left) that SALSA predicts lower values of r_{eff}. This results in lower values of C_{bak}. We see in Fig. 11 (upper left) that the effect on β of the higher number density dominates over the effect of the lower r_{eff}, resulting in values of β that are about 30 % higher in SALSA (green line) than in the MT model (red line). Over the Mediterranean, both SALSA and the MT model predict similar mass densities (Fig. 10, upper right); but SALSA still predicts substantially lower values of r_{eff} (Fig. 9, right). The result is that β computed with the MT model (red line) is almost twice as high as the corresponding results obtained with SALSA (green line) (Fig. 11, upper right).

A similar comparison of the two optics models (red and blue lines in Fig. 11) shows that the new CGS optics model consistently predicts substantially lower values of β than the old EXT optics model. This agrees with the comparison shown in Kahnert et al. (2013) between encapsulated black carbon aggregates and externally mixed homogeneous spheres. (In a retrieval algorithm, an optics model that overestimates the backscattering cross section would result in underestimated retrieval
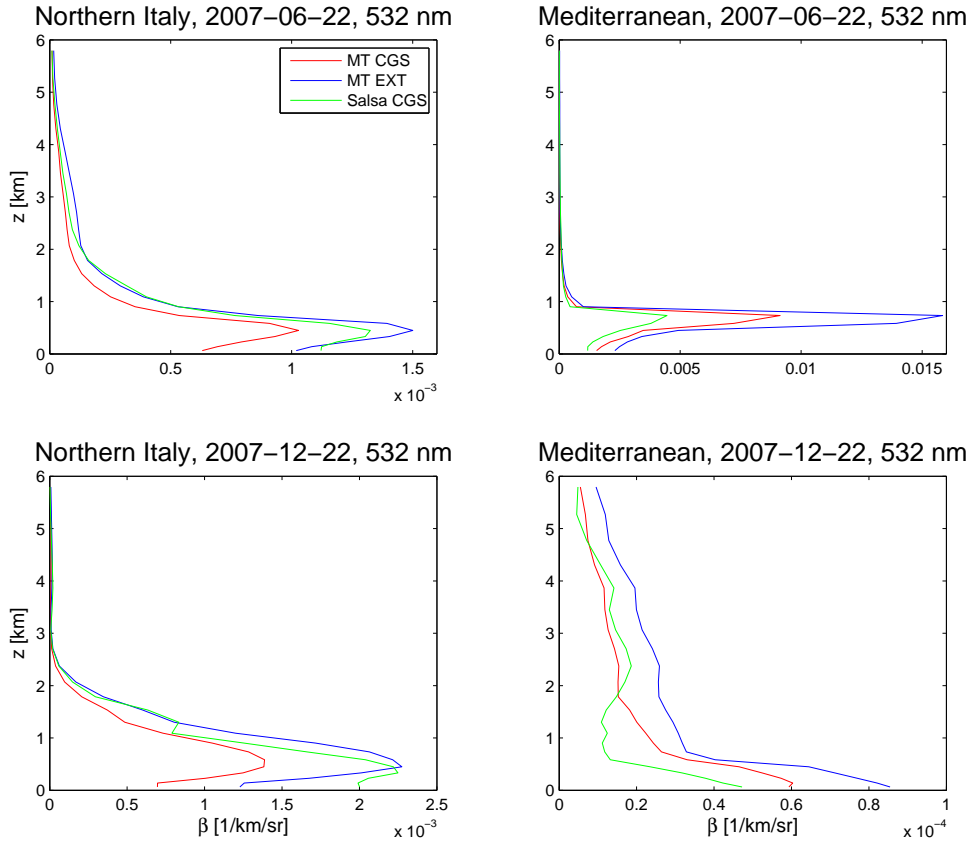
24

Figure 11. Backscattering coefficient at a wavelength of 532 nm at two different locations and at two different instances, computed with the three model versions.

results for the particle number density.) The differences between the two optics models are on the same order of magnitude (and often even slightly larger) than the corresponding differences between the SALSA and the MT versions of the aerosol transport model.

3.4 Ångström exponent

The Ångström exponent α in a wavelength interval $[\lambda_1, \lambda_2]$ is defined as

$$\alpha = -\frac{\log(\tau(\lambda_1)/\tau(\lambda_2))}{\log(\lambda_1/\lambda_2)}, \tag{1}$$

where τ denotes the extinction optical depth. This quantity is often used for obtaining particle size information (usually, the smaller the particle size, the larger α). Table 5 shows values of α for our different test cases computed with the three model versions in the wavelength interval 532–1064

25

Table 5. Ångström exponent in the wavelength region 532–1064 nm for the four different geographical locations, one summer and one winter event, and three model versions.

		MT-EXT	MT-CGS	SALSA-CGS
	Poland	0.32e+00	0.12e+01	0.28e+01
	North Sea	0.80e+00	0.12e+01	0.21e+01
Summer	Northern Italy	0.11e+01	0.11e+01	0.15e+01
	Mediterranean	0.36e+00	0.12e+01	0.21e+01
	Poland	0.80e+00	0.12e+01	0.22e+01
	North Sea	0.79e+00	0.11e+01	0.14e+01
Winter	Northern Italy	0.13e+01	0.10e+01	0.12e+01
	Mediterranean	0.13e+01	0.98e+00	0.14e+01

nm. If we compare the columns labelled MT-CGS and SALSA-CGS, then we see that the mass-transport model consistently gives lower values of α. This is related to the high values of r_{eff} in that model, which we noted earlier. On the other hand, if we compare the columns labelled MT-EXT and MT-CGS, then we see that the new optics model (CGS) predicts higher values of α than the old model (EXT) in the first six rows, and lower values in the last two rows. This indicates that the errors introduced by the simple external-mixture model in computing α are quite unpredictable, even the sign of the error. When used in a size retrieval algorithm the retrieval errors caused by the EXT model would be equally hard to predict. The difference between the MT and SALSA model is somewhat larger, but not much larger, than the differences between the old and new optics models. Note that the performance of the MT model could be improved in comparison to SALSA by modifying the assumed size distribution in the MT model. By contrast, the differences between the two optics models is rather fundamental; it is caused by the over-simplified treatment of aerosol morphology in the EXT model.

4 Conclusions

We have implemented a new aerosol optics model in a regional chemical transport model. The new model differs from an earlier optics model described in Kahnert (2008) in three essential points. (i) While the old model treats all chemical components as externally mixed, the new model accommodates both external and internal mixtures of aerosol species. (ii) The old model treats black carbon aerosols as homogeneous spheres; the new model assumes a fractal aggregate morphology with fractal parameters based on observations. Mass absorption cross sections and single scattering albedos computed with this model have previously been evaluated by comparison with measure-

26

ments (Kahnert, 2010b). (iii) The new model describes internally mixed black carbon aerosols by a recently developed "core-grey-shell" model (Kahnert et al., 2013). This model accounts for the inhomogeneous internal mixing state of black carbon aggregates encapsulated in a shell of liquid-phase material. The model has been evaluated by comparison with reference computations based on observation-derived realistic models for encapsulated fractal aggregates (Kahnert et al., 2013). Item (i) has been incorporated in other CTMs earlier (e.g. Saide et al. (2013)); however, to the best of our knowledge, items (ii) and (iii) go significantly beyond the current state-of-the-art of aerosol optics models employed in CTMs. The main question of the present study is whether or not such a substantial level of detail in the description of aerosol morphology and optical properties is needed in a CTM.

To this end we compare radiative fluxes, backscattering coefficients, and Ångström exponents modelled with the old and new optics models. To gauge the differences we observe, we further compare two model versions of the CTM with different levels of detail in the aerosol process descriptions, namely, one version that includes aerosol dynamic processes, and one simpler mass-transport model, in which aerosol dynamics is switched off. The importance of aerosol dynamics is well understood an can therefore serve as a reference. The comparison showed that both for radiative fluxes, and for backscattering coefficients, and for Ångström exponents the differences between the two different optics models are of similar magnitude as corresponding differences between an aerosol dynamics and a mass-transport model. This strongly suggests that over-simplified aerosol optics models are likely to introduce substantial errors in modelled radiative fluxes and remote sensing-relevant observables. In Earth-system models such errors would enter into the simulation of the direct aerosol radiative forcing effect and add to all other sources of error in the model. In model evaluations that make use of remote sensing observations these errors would complicate the comparison between model results and observations.

The modifications to the optics model studied here were limited to black carbon aerosols. There are many other aerosols with complex morphological properties, such as mineral dust, which our optics model still treats by an over-simplified homogeneous sphere model. The findings of our study should be an incentive for improving the description of dust and volcanic ash optical modelling in CTMs. A review of our current state of knowledge on aerosol morphology and aerosol optics for a variety of different aerosols has recently been reviewed in Kahnert et al. (2014).

The findings of this study are likely to have implications for chemical data assimilation. In data assimilation one employs an *observation operator* that maps the model results to observable quantities. In case of satellite-based observations of aerosol optical properties, the observation operator is just our aerosol optics model, possibly coupled to a radiative transfer model. Many data assimilation methodologies, such as the variational method, require a linear (or, at least, linearised) observation operator. In the old optics model, which assumes externally mixed aerosols, the observation operator is, indeed, linear (Kahnert, 2008). This largely explains why external-mixture optics models are

27

widely used in chemical data assimilation systems (e.g. Kahnert (2008); Benedetti et al. (2009); Liu

630 et al. (2011)). However, the new optics model we introduced here does not provide us with a linear map from the aerosol concentrations to the optical parameters. To what extend one could linearise this model and make use of its Jacobian in a data assimilation system mainly depends on the degree of nonlinearity, which would need to be investigated thoroughly.

References

Adachi, K. and Buseck, P. R.: Internally mixed soot, sulfates, and organic matter in aerosol particles from Mexico City, Atmos. Chem. Phys., 8, 6469–6481, 2008.

640 Adachi, K., Chung, S. H., Friedrich, H., and Buseck, P. R.: Fractal parameters of individual soot particles determined using electron tomography: Implications for optical properties, J. Geophys. Res., 112, D14 202, doi:10.1029/2006JD008 296, 2007.

Andersson, C., Langner, J., and Bergström, R.: Interannual variation and trends in air pollution over Europe due to climate variability during 1958-2001 simulated with a regional CTM coupled to the ERA40 reanalysis,

645 Tellus Ser. B, 59B, 77–98, 2007.

Andersson, C., Bergström, R., Bennet, C., Robertson, L., Thomas, M., Korhonen, H., Lehtinen, K. H. J., and Kokkola, H.: MATCH-SALSA — Multi-scale Atmospheric Transport and CHemistry model coupled to the SALSA aerosol microphysics model — Part 1: Model description and evaluation, Geosci. Model Dev., 8, 171–189, 2015.

650 Benedetti, A., Morcrette, M. J.-J., Boucher, O., Dethof, A., Engelen, R. J., Huneeus, M. F. H. F. N., Jones, L., andS. Kinne, J. W. K., Mangold, A., Razinger, M., Simmons, A. J., and Suttie, M.: Aerosol analysis and forecast in the European Centre for Medium-Range Weather Forecasts Integrated Forecast System: 2. Data assimilation, J. Geophys. Res., 114, D13 205, 2009.

Bond, T. C. and Bergstrom, R. W.: Light absorption by carbonaceous particles: An investigative review, Aerosol

655 Sci. Technol., 40, 27–67, 2006.

Bruggemann, D. A. G.: Berechnung verschiedener physikalischer Konstanten von heterogenen Substanzen. 1. Dielektrizitätskonstanten und Leitfähigkeiten der Mischkörper aus isotropen Substanzen, Ann. Phys., 24, 636–664, 1935.

Chang, H. and Charalampopoulos, T. T.: Determination of the wavelength dependence of refractive indices of

660 flame soot, Proc. R. Soc. Lond. A, 430, 577–591, 1990.

Dubovik, O., Sinyuk, A., Lapyonok, T., Holben, B. N., Mishchenko, M. I., Yang, P., Eck, T. F., Volten, H., Muñoz, O., Veihelmann, B., van der Zande, W. J., Leon, J.-F., Sorokin, M., and Slutsker, I.: Application of spheroid models to account for aerosol particle nonsphericity in remote sensing of desert dust, J. Geophys. Res., 111, D11 208, 2006.

665 Foltescu, V., Pryor, S. C., and Bennet, C.: Sea salt generation, dispersion and removal on the regional scale, Atmos. Environ., 39, 2123–2133, 2005.

Gerber, H. E.: Relative-humidity parameterization of the Navy Aerosol Model (NAM), Tech. Rep. 8956, Naval Research Laboratory, Washington, D.C., 1985.

Jones, A. R.: Light scattering in combustion, in: Light Scattering Reviews, edited by Kokhanovsky, A., Springer,

670 Berlin, pp. 393–444, 2006.

Kahnert, F. M.: Reproducing the optical properties of fine desert dust aerosols using ensembles of simple model particles, J. Quant. Spectrosc. Radiat. Transfer, 85, 231–249, 2004.

Kahnert, M.: Variational data analysis of aerosol species in a regional CTM: background error covariance constraint and aerosol optical observation operators, Tellus Ser. B, 60B, 753–770, 2008.

675 Kahnert, M.: Modelling the optical and radiative properties of freshly emitted light absorbing carbon within an atmospheric chemical transport model, Atmos. Chem. Phys., 10, 1403–1416, 2010a.

Kahnert, M.: On the discrepancy between modelled and measured mass absorption cross sections of light absorbing carbon aerosols, Aerosol Sci. Technol., 44, 453–460, 2010b.

Kahnert, M. and Devasthale, A.: Black carbon fractal morphology and short-wave radiative impact: a modelling

680   study, Atmos. Chem. Phys., 11, 11 745–11 759, 2011.

Kahnert, M., Nousainen, T., and Lindqvist, H.: Models for integrated and differential scattering optical properties of encapsulated light absorbing carbon aggregates, Optics Express, 21, 7974–7993, 2013.

Kahnert, M., Nousiainen, T., and Lindqvist, H.: Review: Model particles in atmospheric optics, J. Quant. Spectrosc. Radiat. Transfer, 146, 41–58, 2014.

685   Kokkola, H., Korhonen, H., Lehtinen, K. E. J., Makkonen, R., Asmi, A., Järvenoja, S., Anttila, T., Partanen, A.-I., Kulmala, M., Järvinen, H., Laaksonen, A., and Kerminen, V.-M.: SALSA — a Sectional Aerosol module for Large Scale Applications, Atmos. Chem. Phys., 8, 2469–2483, 2008.

Kupiainen, K. and Klimont, Z.: Primary emissions of submicron and carbonaceaous particles in Europe and the potential for their control, Tech. Rep. IR-04-079, IIASA, Laxenburg, Austria, 2004.

690   Kupiainen, K. and Klimont, Z.: Primary emissions of fine carbonaceous particles in Europe, Atmos. Environ., 41, 2156–2170, 2007.

Kylling, A., Bais, A. F., Blumthaler, M., Schreder, J., Zerefos, C. S., and Kosmidis, E.: The effect of aerosols on solar UV irradiances during the Photochemical Activity and Solar Ultraviolet Radiation campaign, J. Geophys. Res., 103, 26,051–26,060, 1998.

695   Liu, Z., Liu, Q., Lin, H.-C., Schwartz, C. S., Lee, Y.-H., and Wang, T.: Three-dimensional variational assimilation of MODIS aerosol optical depth: Implementation and application to a dust storm over East Asia, J. Geophys. Res., 116, D23 206, 2011.

Mackowski, D. W. and Mishchenko, M. I.: A multiple sphere T-matrix Fortran code for use on parallel computer clusters, J. Quant. Spectrosc. Radiat. Transfer, 112, 2182–2192, 2011.

700   Mårtensson, E. M., Nilsson, E. D., de Leeuw, G., Cohen, L. H., and Hansson, H.-C.: Laboratory simulations and parameterization of the primary marine aerosol production, J. Geophys. Res., 108, D9, 4297, 2003.

Maxwell Garnett, J. C.: Colours in metal glasses and in metallic films, Philos. Trans. R. Soc. A, 203, 385–420, 1904.

Mishchenko, M. I., , Travis, L. D., and Lacis, A. A.: Scattering, absorption, and emission of light by small

705   particles, Cambridge University Press, Cambridge, 2002.

Monahan, E. C., Spiel, D. E., and Davidson, K. L.: A model of marine aerosol generation via whitecaps and wave disruption, in: Oceanic Whitecaps and their role in air-sea exchange, edited by Monahan, E. C. and Niocaill, G. M., pp. 167–174, D Reidel, Norwell, MA, 1986.

Neusüß, C., Wex, H., Birmili, W., Wiedensohler, A., Koziar, C., Busch, B., Brüggemann, E., Gnauk, T.,

710   Ebert, M., and Covert, D. S.: Characterization and parameterization of atmospheric particle number-, mass-, and chemical-size distributions in central Europe during LACE 98 and MINT, J. Geophys. Res., 107, doi:10.1029/2001JD000 514, 2002.

Nousiainen, T.: Optical modeling of mineral dust particles: A review, J. Quant. Spectrosc. Radiat. Transfer, 110, 1261–1279, 2009.

715   Nousiainen, T., Kahnert, M., and Veihelmann, B.: Light scattering modeling of small feldspar aerosol particles using polyhedral prisms and spheroids, J. Quant. Spectrosc. Radiat. Transfer, 101, 471–487, 2006.

Robertson, L., Langner, J., and Engardt, M.: An Eulerian limited-area atmospheric transport model, J. Appl. Meteor., 38, 190–210, 1999.

720 Saide, P. E., Charmichael, G. R., Liu, Z., Schwartz, C. S., Lin, H. C., da Silva, A. M., and Hyer, E.: Aerosol optical depth assimilation for a size-resolved sectional model: impacts of observationally constrained, multi-wavelength and fine mode retrievals on regional scale analysis and forecasts, Atmos. Chem. Phys., 13, 10 425–10 444, 2013.

Yurkin, M. A. and Hoekstra, A. G.: The discrete dipole approximation: An overview and recent developments, J. Quant. Spectrosc. Radiat. Transfer, 106, 558–589, 2007.